DTU Mechanical Engineering
Department of Mechanical Engineering

Modelling of ductile failure over multiple scales

Ingrid Holte

PhD Thesis

Modelling of ductile failure over multiple scales

Ph.D. Thesis

Ingrid Holte

Department of Mechanical Engineering
Technical University of Denmark

Published in Denmark by
Technical University of Denmark

Technical University of Denmark
Department of Mechanical Engineering
Section of Solid Mechanics
Nils Koppels Allé, Building 404
2800 Kongens Lyngby
Denmark

Tel: (+45) 45 25 13 96
Fax: (+45) 45 25 19 61
www.mek.dtu.dk

Publication Reference Data
I. Holte
Modelling of ductile failure over multiple scales
Ph.D. Thesis
Section of Solid Mechanics, Department of Mechanical Engineering
Technical University of Denmark
January 2021
ISBN 978-87-7475-641-5
DCAMM Special Report No. S289

Let us not take ourselves too seriously. None of us has a monopoly on wisdom.

Queen Elizabeth II

Preface

This thesis is submitted to the Technical University of Denmark in partial fulfilment of the requirements for the degree of Doctor of Philosophy, Ph.D. The Danish Council for Independent Research funded the Ph.D project through the research project "Advanced Damage Models with InTrinsic Size Effects." The work has been carried out at the Section of Solid Mechanics at the Department of Mechanical Engineering at the Technical University of Denmark from February 2018 to January 2021. The project was supervised by Professor Christian F. Niordson, Associate Professor Kim L. Nielsen, and Professor Grethe Winther. Parts of the work were conducted during an external research stay at Texas A&M University in College Station, Texas from September 2019 to February 2020 under Assistant Professor Ankit Srivastava's supervision.

I would like to thank Christian and Kim for giving me the opportunity to do this PhD and for being great supervisors. I have appreciated you sharing your knowledge and all the corrections you have given (or suggestions, as you call them). A special thanks to Ankit, who welcomed me into his group at Texas A&M University. I valued all your support, always given with a smile and a lot of humour. A huge thank you to Emilio for all the help and enthusiastic e-mail responses. I appreciate it.

My gratitude goes to the Ph.Ds and postdocs at the Department who, along the way, turned into great friends - you know who you are. Thanks for making me feel at home.

Finally, a big thank you to my parents for unquestionably supporting me. You are always there when I look back.

Ingrid Holte

Sandvika, Norway, January 2021

Ingrid Holte

Abstract

This thesis investigates damage development through void growth in porous, ductile materials, both for conventional isotropic materials and materials exhibiting gradient strengthening. Two types of modelling approaches are used for the numerical analyses. The first is a local approach based on the classical micro-mechanical Gurson-Tvergaard model that accounts for porosity driven material damage through an averaged void volume fraction. Niordson and Tvergaard [1] have extended the model to account for gradient strengthening effects by introducing an intrinsic material length parameter in the constitutive equations. The aim is to investigate the possibility of simulating plastic strain gradient effects on damage evolution at the micron scale by employing an intrinsic length scale parameter in the continuum model's constitutive equations. The gradient enriched Gurson-Tvergaard model accurately predicts the elevated yield point and suppressed void growth associated with gradient strengthening in a parametric study. However, void shape and inter-void ligament sizes affect the load-carrying capacity more than the void volume fraction itself. A well-known extension to the Gurson-Tvergaard model accounting for the void shape evolution's effect on material damage, namely the Gologanu-Leblond-Devaux model, has also applied to conventional isotropic, porous, ductile materials. Current work is being done to extend this model to capture the effects of plastic strain gradients in gradient hardening materials, allowing for combined investigation of void size and shape on the macroscopic material response.

The second of the two modelling approaches consists of analysing discrete voids embedded in unit cells through finite element simulation. The finite element mesh consists of elements with a strain gradient plasticity theory incorporated in the element property definition. Accounting for the role of the plastic strain gradients in the constitutive equations naturally introduces a material length scale parameter for dimensional consistency. This non-local approach allows for an immediate investigation of the effects of inter-void ligament sizes and void distribution inhomogeneity on the void growth and the subsequent damage, as their presence is not determined by an averaging parameter, such as the void volume fraction. A study on the combination of void size and inter-void ligament size has been conducted. The results showed that a smaller inter-void ligament size would reduce the material's load-carrying capacity unless the microstructure is small enough to induce large plastic strain gradients in the inter-void ligaments, inhibiting localisation of plastic flow. The material response will be independent of inter-void ligament size for materials with a large length scale parameter. Ongoing work to further investigate the effect of the randomness of void distributions is being conducted. The combined effects of void clustering and microstructure size under different loading conditions are investigated by analysing the response of representative volume elements with a random distribution of voids. The method for such an investigation has been established, and some preliminary results presented.

Resumé

Denne afhandling undersøger skadesudvikling i porøse, duktile materialer, både for konventionelle, isotrope materialer og materialer der udviser gradientforstærkning. To numeriske modeller anvendes til de numeriske analyser. Den første er en lokal model, baseret på den klassiske mikromekaniske Gurson-Tvergaard-model, der tager højde for porøsitetsdrevet materialeskade igennem et sæt af konstitutive ligninger som inkluderer et mål for den gennemsnitlig volumenfraktion af porer. Niordson og Tvergaard [1] har udvidet denne model til yderligere at tage højde for gradientforstærkningseffekter ved at indføre en materialelængdeparameter i de konstitutive ligninger. Målet med dette er at muliggøre undersøgelse af de plastiske tøjningsgradienters indvirkning på porevækst på mikroskalaen. I en parametrisk undersøgelse viste den gradientberigede Gurson-Tvergaard-model sig at forudsige det forhøjede flydepunkt og undertrykt porevækst forbundet med gradientforstærkning. Imidlertid synes poreform og afstand imellem porer at påvirke materialets belastningskapacitet mere end selve volumenfraktionen. Gologanu-Leblond-Devaux modellen, som er en velkendt udvidelse af Gurson-Tvergaard modellen, der tager højde for ikke-sfærisk formudvikling af porer, er også anvendt på konventionelle isotrope, porøse, duktile materialer. Der arbejdes i øjeblikket med en udvidelse af denne model til at fange gradientforstærkende effekter i gradientberigede materialer. Modellen forventes at give mulighed for en kombineret undersøgelse af porerstørrelse og form på det makroskopiske materialerespons.

Den anden af de to modelleringsmetoder der er benyttet i arbejdet, består i at analysere porer i materialer på baggrund af finite element simuleringer af repræsentative volumenelementer. Finite element diskretiseringen består af elementer der følger en plastisk tøjningsgradientsberiget plasticitetsteori. Tøjningsgradient plasticitetsteorien har naturligt en materialelængdeskalaparameter inkluderet for dimensional konsistens i de konstitutive ligninger og muliggør undersøgelse af størrelseseffekter i forbindelse med skadesudviklingen. Modellen tillader direkte undersøgelse af kombineret indflydelse af poreafstand og in-homogenitet i porerfordelingen på porevæksten idet porernes tilstedeværelse ikke bestemmes af en gennemsnitsparameter, såsom volumenfraktionen. Der er udført en undersøgelse af kombinationen af porerstørrelse og afstanden mellem dem, og resultaterne viser at mindre afstand imellem porerne vil reducere materialets bæreevne, medmindre mikrostrukturen er lille nok til at inducere store plastiske tøjningsgradienter. I dette tilfellet hemmer gradientforstærkningen lokalisering af plasticitet. Materialeresponset vil være uafhængig af afstanden imellem porer for materialer med en stor længdeparameter (lille skala). Igangværende arbejde fokuserer yderligere på at undersøge effekten af tilfældighed af porerfordelinger. Målet er at undersøge de kombinerede effekter af klyngedannelse og mikrostrukturstørrelse under forskellige belastningsforhold på materialerespons gennem simuleringer af repræsentative volumenelementer. Metoden til en sådan undersøgelse er udviklet og foreløbige resultater præsenteret.

Publications

Journal papers

[P1] I. Holte, C.F. Niordson, K.L. Nielsen, V. Tvergaard, Investigation of a gradient enriched Gurson-Tvergaard model for porous strain hardening materials, *European Journal of Mechanics / A Solids*, **75**, 472–484, 2019

[P2] I. Holte, A. Srivastava. E. Martínez-Pañeda, C.F. Niordson, K.L. Nielsen, Interaction of void spacing and size on inter-void flow localisation, *Journal of Applied Mechanics*, **88**(2), 2020

Contents

1 Introduction **1**
1.1 Context and motivation . . . 1
1.2 Outline of the thesis . . . 4

2 Background **7**
2.1 Mechanical concepts . . . 7
2.1.1 Geometrically Necessary Dislocations . . . 7
2.1.2 Ductile fracture . . . 8
2.2 Micro-mechanics based continuum models for ductile failure . . . 10
2.3 Strain gradient plasticity theories . . . 11

3 Material models **13**
3.1 Plasticity . . . 13
3.2 J_2 flow theory . . . 14
3.3 Gurson-Tvergaard material model . . . 15
3.3.1 Gradient enriched Gurson-Tvergaard material model . . . 16
3.4 Gologanu-Leblond-Devaux material model . . . 18
3.5 Strain gradient plasticity . . . 19

4 Numerical implementation **25**
4.1 Single-point continuum models . . . 25
4.2 Axi-symmetric unit cells . . . 25
4.3 Three dimensional unit cells . . . 26

5 Summary of results and discussion **31**
5.1 Gradient enriched Gurson-Tvergaard model . . . 31
5.2 Combined effects of inter-void ligament size and void size . . . 38

6 Ongoing work **47**
6.1 Gradient enriched Gologanu-Leblond-Devaux model . . . 47
6.2 Combined effects of void clustering and void size . . . 56

7 Conclusions **63**

References **67**

Appendix A Yield surface parameters and derivatives **73**
A.1 Yield surface parameters . . . 73
A.2 Yield surface derivatives . . . 75

Appendix B Void evolution plots **77**

Publications
[P1] . . . 79
[P2] . . . 95

1. Introduction

1.1 Context and motivation

Ductile materials display a strong size effect when deformed non-uniformly into the plastic range. Several micron-scale experiments show that the material response to external loading changes with specimen size when the specimen is sufficiently small. Size effects have been observed in several micro and nanoindentation experiments, where the measured indentation hardness of the material increases as the width of the indenter decreases [2–7]. The trend observed from the micron-scale experiments is that *smaller is stronger*, which is associated with plastic strain gradients. Figure 1.1, taken from [4], shows the effect of indent diagonal on hardness in a tungsten single crystal, which increases as the diagonal decreases. Along the same lines, Stölken and Evans [8] performed micro-bending tests of nickel thin foils with different thicknesses and observed a significant effect on the material response when decreasing the thickness from 100 µm to 12.5 µm. This goes against conventional plasticity, which predicts that the normalised bending moment, $M/(bh^2)$, where b and h are the foils' width and thickness, respectively, should superpose for all values of h. However, the results showed that the thinner specimen are stronger and strain harden more than the thicker ones. Fleck et al. [9] applied torsion to thin copper wires and observed that the scaled shear strength increases by a factor of three as the wire diameter decreases from 170 µm to 12 µm. Figure 1.2, taken from [9], clearly shows the systematic increase in torsional hardening with decreasing wire diameter, but only a minor influence of specimen size on tensile behaviour.

The underlying mechanism that governs energy dissipation in ductile media under plastic deformation is the propagation of dislocations. Material strain hardening is controlled by the total density of dislocations, of which two types can be distinguished, namely statistically stored

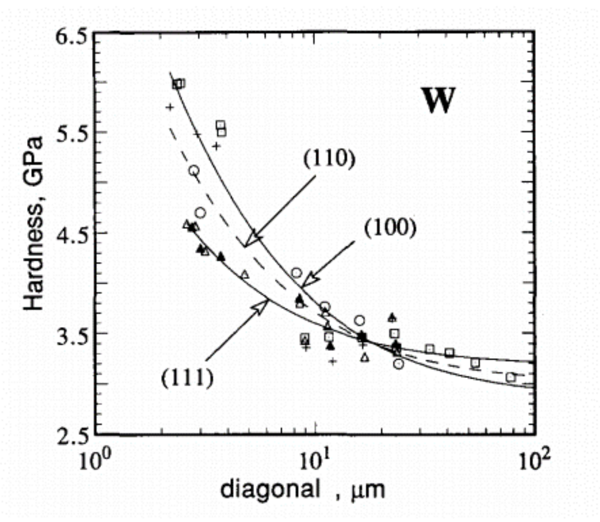

Figure 1.1. Increasing hardness measured in GPa with decreasing indent diagonal length given in µm. Experimental results are shown by markers, fitted with an equation, given by the full drawn lines, where hardness is proportional to the dislocation density. From [4].

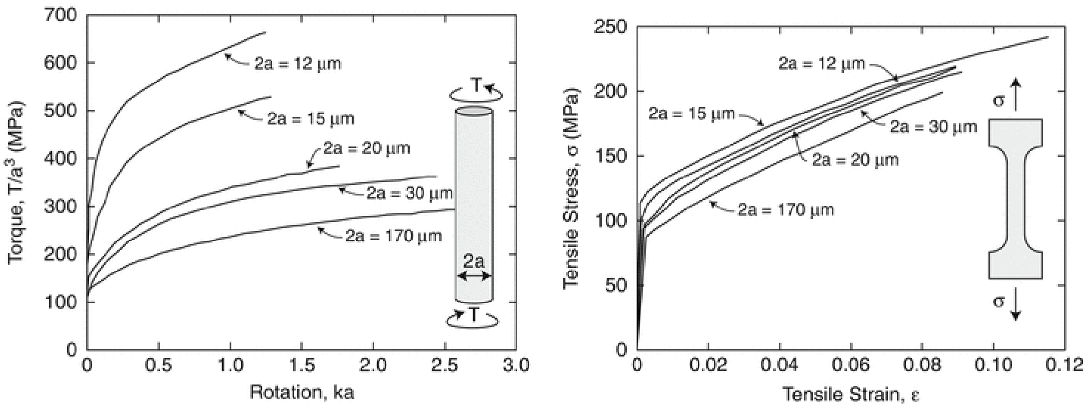

(a) (b)

Figure 1.2. (a) Response from copper wires with diameters in the range $2a = 12 - 170$ µm. The normalised torque, T/a^3, is shown as function of κa, where κ is the twist per unit length wire. If material response was independent of strain gradients, the response would fall on the same curve. (b) Uniaxial tension of wires of the same diameter show nearly no size effect confirming that the strengthening is due to the presence of strain gradients. From [10].

dislocations (SSDs) and geometrically necessary dislocations (GNDs). The SSDs are evenly distributed throughout the material, but the GNDs arise to accommodate the plastic strain gradients consistent with non-uniform deformation. The density of GNDs plays an essential part in micron-scale plasticity problems. SSDs are, in general, the main contributors to plastic flow, and their immobilisation due to, for example, pile-up is the main cause of work hardening. On the macroscopic scale, this is a phenomenon well captured by conventional plasticity theory. When plasticity occurs in a specimen or in geometries at the micron-scale, however, the density of GNDs becomes large compared to that of SSDs, sometimes even dominant, and the gradients of plastic strain associated with the density of GNDs will strengthen the material further than what conventional plasticity can predict. Despite both experimental evidence and insight into the mechanisms involved, putting forward a good extension to classical plasticity incorporating a dependence on plastic strain gradients has proven a challenge. An internal length scale must be included in the constitutive law. Strain gradient plasticity (SGP) is a formalism designed to extend plasticity theory to smaller scales. Conventional plasticity simply relates plastic work to strains only. Strain gradient plasticity incorporates plastic strain gradients, thereby naturally introducing an intrinsic length scale into the material model, allowing the theory to capture size effects.

For materials that deform by the movement of dislocations, the corresponding size effects have implications where deformation varies significantly in the micrometer range, where the ductile fracture process unfolds. The dissipation mechanism of nucleation and growth of microvoids and their ultimate coalescence into macrovoids or cracks defines the ductile fracture process. Void growth is driven by plastic deformation in regions adjacent to the void surface, a process ultimately driven by dislocation movement. Numerous molecular dynamics simulations have been performed, indicating that dislocation emission from growing voids is the primary mechanism for the material transfer required for the porosity evolution [11–16]. Size effects also come into play for this process. Traiviratana et al. [17] performed molecular dynamics simulations on porous mono- and bicrystalline copper under tensile uniaxial strains. The results, shown as squared markers in Figure 1.3, reveal that the critical stress for dislocation emission at the void surface increases as void size decreases when the void size is in the range of Burger's vector. This indicates that the trend mentioned above of *smaller is stronger* also applies to the evolution of microvoids.

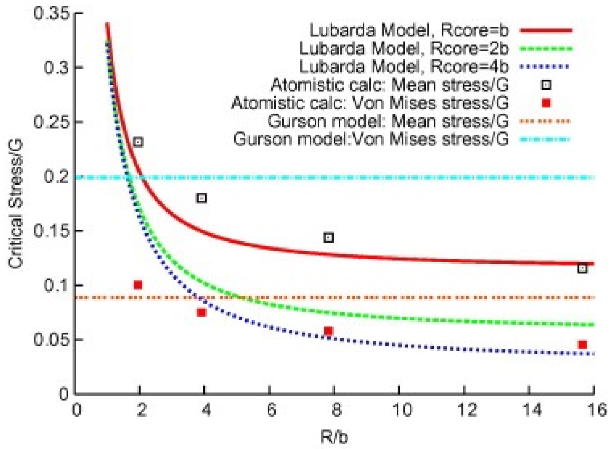

Figure 1.3. Normalised critical stress against normalised void size confirming size effects. On the vertical axis, the critical stress is normalised with the shear modulus, G, and the horizontal axis depicts the void radius, R, normalised with Burger's vector, b. The Lubarda model refers to the analytical model by Lubarda et al.[18]. From [17].

Ductile failure has historically been modelled by the use of homogenisation theory, thereby neglecting the size effects at the micron-scale, even though the underlying mechanism of void growth unfolds at the micrometre range. The notable Gurson-Tvergaard model [19–21] lays the foundation for modelling ductile fracture in terms of a macroscopic yield criterion and an evolution law for a single microstructural variable: the average void volume fraction. The intrinsic length scales, such as void size and spacing, are averaged out by adopting the void volume fraction to describe the entire damage evolution. This renders the model size-independent, as shown in Figure 1.3, where the horizontal lines clearly show that the predicted critical stresses from the Gurson model do not vary with void size. Given the distinct physical mechanism through which energy dissipation occurs at the micron-scale, it is not surprising that ductile fracture models based on conventional plasticity with averaged damage parameters fail to describe the combined phenomena of dislocation propagation and void evolution.

The work in this thesis focuses on methods for modelling ductile failure accounting for intrinsic material size-effects, thereby bridging the effects from the governing micro-mechanisms to the component level. To this end, several types of numerical simulations have been performed, presented in Fig. 1.4. Advanced homogenised plasticity theories have been used on single-point models to represent a homogeneously, voided continuum, Fig. 1.4i. For initially spherical voids, the Gurson-Tvergaard model is used with a recent proposal for extensions incorporating size-effects in the constitutive equations. This will ensure an accurate representation of stresses over multiple length scales and connect the micron and macro-scales. The results are compared to those from micro-mechanical analyses of an axi-symmetric unit cell model, shown in Fig. 1.4ii, with the intrinsic size effect accounted for by a matrix material governed by strain gradient plasticity. Good agreement between the single-point model and axi-symmetric unit cells is observed for small deformation levels until significant changes in the void shape occur. The work, therefore, goes on to explore a more advanced continuum model, which accounts for void shape. The Gologanu-Leblond-Devaux model [22–24] is a well-known extension to the Gurson-Tvergaard model and has been implemented for a single-point model. The results are compared to axi-symmetric cell models with voids of different initial shapes embedded in a gradient enriched material matrix. This is ongoing work with the aim to incorporate the combined effects of the shape and size of voids on the micron-scale in the constitutive equations for a continuum governed by the Gologanu-Leblond-Devaux model. Three-dimensional void configurations are

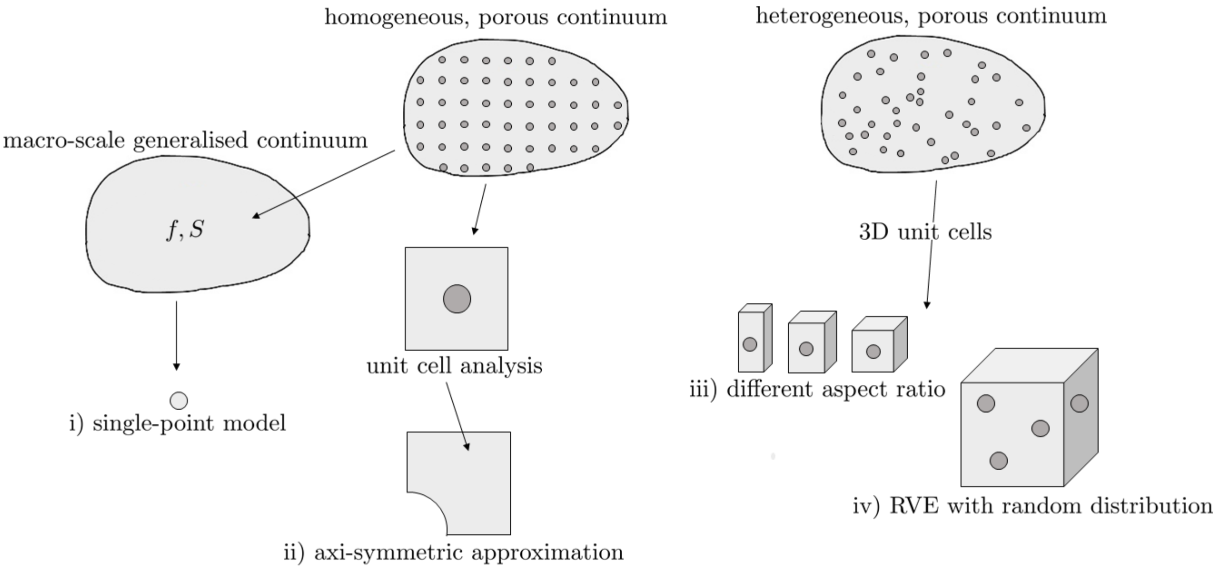

Figure 1.4. Overview of the models for the work in the thesis. From left, i) single-point models approximating a macro-scale generalised continuum, ii) axi-symmetric approximations of a unit cell with a single void embedded in a gradient matrix, iii) three dimensional unit cells with same initial void volume fraction, but different aspect ratios giving different inter-void ligament sizes, iv) three dimensional representative volume elements with a random distribution of voids.

analysed to characterise the size-effects under different three-dimensional loading states. To investigate the effect of void spacing in combination with size effects on macroscopic material response, three-dimensional cuboidal unit cells with a single population of voids are analysed. The different void spacings are accounted for by changing the unit cell aspect ratio, as shown in Fig. 1.4iii. The results showed that for a conventional, non-gradient strengthened material, a homogeneous distribution of voids is detrimental to the macroscopic yield strength. There is a range of inter-void ligament sizes over which material performance reaches its peak. The results also showed that introducing gradients will change the deformation mechanism of the unit cell. The conventional material will typically experience localisation of plastic flow in the inter-void ligament, while the presence of gradients will strengthen the inter-void ligaments sufficiently for plasticity to initiate as flow in the entire unit cell. The effect of inter-void spacing will disappear with sufficient gradient strengthening, regardless of loading state, and the material response will reach a threshold level for all configurations of void spacing and loading states. To investigate the effect of inhomogeneity further, unit cells with multiple voids randomly placed are analysed to quantify the effects of void clustering. The material is represented by a multi-voided cell, called a representative volume element, exemplified in Fig. 1.4iv. This is ongoing work with the scope to analyse the effects of void clustering in a gradient strengthening material under different three dimensional loading conditions.

1.2 Outline of the thesis

The thesis is structured as follows: Chapter 2 starts by describing the mechanisms at the micron-scale giving rise to the observed size effects associated with plastic strain gradients when plasticity is initiated at this scale. Further, the chapter explores the ductile fracture process and how this relates to the size effects. An attempt to bridge the two fields, strain gradient plasticity and ductile fracture, is made. Last, the chapter presents the state-of-the-art modelling techniques for both ductile failure and strain gradient plasticity. Chapter 3 gives a detailed description of the material models used for the work in the thesis. Starting with a fundamental plasticity model, the chapter goes on to thorough expositions of more sophisticated continuum scale plasticity models that account for void induced damage, such as the Gurson-Tvergaard model and an extension introducing void shape effects, the Gologanu-Leblond-Devaux model. Details of an extension of the Gurson-Tvergaard model to the micron-scale is given. The last material model treated in Chapter 3 is a strain gradient plasticity model. Details are given on the model's governing equations, the constitutive equations, and their thermodynamic consistency before arriving at the solution method. The numerical framework for each of the material models is presented in Chapter 4. The continuum scale plasticity models are implemented and solved incrementally in MATLAB. The strain gradient plasticity model has been incorporated in a finite element framework. Both an in-house FORTRAN code and the commercial finite element software ABAQUS have been used for the work in this thesis. Chapter 5 serves as a summary of the main results and discussions in the two appended papers.

The first paper, "Investigation of a gradient enriched Gurson-Tvergaard model for porous strain hardening materials" [P1], presents investigation of an extension to the classic Gurson-Tvergaard model to incorporate size effects at the micron-scale. The predicted results from this model are compared to those of an axi-symmetric unit cell model with a discrete void embedded in a strain gradient plasticity governed matrix. For the work in the second paper, "Interaction of void spacing and size on inter-void flow localisation" [P2], limit-load type analyses on three-dimensional voided unit cells with a plastic strain gradient matrix material are conducted. The work explores the combined effects of different spacing between voids and plastic strain gradients in the inter-void ligaments on the material response for a range of different loading conditions.

Chapter 6 presents two unpublished studies. The first one is inspired by [P1] and investigates the combined effect of void size and shape on the ductile damage process. The aim is to extend a continuum scale plasticity model accounting for both void volume fraction and void shape to the micron-scale, thereby accounting for size effects. The plasticity model results will be compared to corresponding predictions from an axi-symmetric voided unit cell model controlled by a plastic strain gradient theory. The second study draws inspiration from [P2] and investigates the effect of void clustering on material performance. Void clusters are generated randomly and characterised according to two different criteria. Material response for the clusters under different loading conditions is investigated, and preliminary results presented. The combined effects of clustering and material size effects are slightly touched upon, and some initial results are given.

Finally, Chapter 7 concludes the work published in [P1] and [P2] along with the unpublished work presented in this thesis.

2. Background

2.1 Mechanical concepts

This section is dedicated to further elaborate on some fundamental concepts, introduced in Section 1.1, related to strain gradient plasticity and ductile fracture. The overlap of the two fields is discussed, and explains why accounting for gradients in the plastic strain rate field is important when modelling ductile failure. Last, an overview of the state-of-the-art of strain gradient plasticity theories and ductile failure modelling is provided.

2.1.1 Geometrically Necessary Dislocations

The notion of plasticity involves structural re-arrangements of atoms at the micron-scale. These re-arrangements form the underlying mechanisms of plastic deformation in metals and usually involve the migration of dislocations. All materials have a certain density of dislocations in them. This density of dislocations controls material strain hardening and strengthening. As straining progresses during deformation, the dislocation density increases as the re-arrangement of material is accompanied by numerous sites emanating dislocations. Piling up of dislocation starts micro-deterioration processes, commonly called damage, coinciding with the onset of plastic deformation.

(a) (b)

Figure 2.1. (a) Geometrically necessary dislocations in a plastically bent metal beam. A periodic array of dislocations with Burger's vector b and spacing L will generate a lattice curvature equal to b/L^2. (b) A schematic view of GNDs in a plastically bent lattice. From [25].

There are different ways in which dislocations can accumulate and cause material hardening and strengthening. Statistically Stored Dislocations (SSDs) are evenly distributed throughout the material and arise during plastic flow. The SSDs have statistics of equal and negative signs and therefore have a zero net Burger vector density. Burger vector is denoted b throughout this thesis, and represents the magnitude and direction of lattice distortion resulting from a dislocation. The contribution to material hardening comes from the SSDs randomly trapping each other, especially when the density is high. During plastic deformation, dislocations may be required for compatible shape change of material [10]. These dislocations are referred to as Geometrically Necessary Dislocations (GNDs) and appear in strain gradient fields due to geometrical constraints. The physical notion of GNDs may be further explained by a plastically deformed bent beam, as seen in Fig. 2.1. The beam is shown in its entirety in Fig. 2.1a, where it can be observed that the beam is stretched across its top face and compressed at the bottom. Extra storage of dislocations is required at the top of the beam to accommodate the

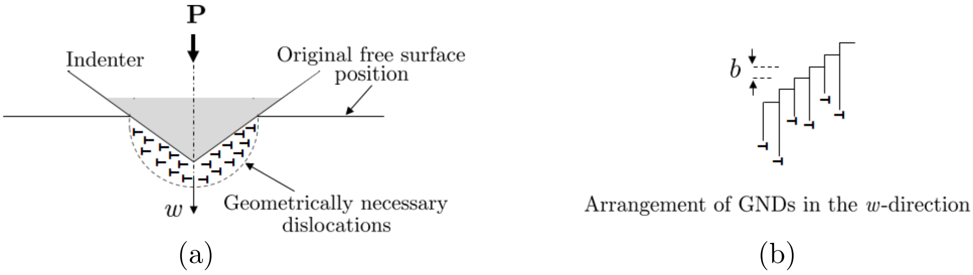

Figure 2.2. (a) Axi-symmetric conical indenter indenting a free surface. The geometrically necessary dislocations (GND) are created during the indentation process. (b) Schematic view of the atomic steps given by the Burger vector, b, created at the indented surface and the associated GNDs. Adapted from [26].

.

lattice curvature [25]. Further, Fig. 2.1b shows the top edge of the beam at a higher resolution where GNDs, here depicted as extra atomic half-planes, have migrated to the top of the beam to satisfy the non-uniform plastic deformation. The concept of GNDs may also be explained using indentation, as seen in Fig. 2.2. The material initially occupying the region of plastic indent has been pushed into the matrix as extra half-planes, as depicted in Fig. 2.2a. A schematic view of the steps at the atomic level associated with the inserted half-planes at the indented surface and the GNDs are shown in Fig. 2.2b.

Plastic work hardening of material is due to both statistically stored and geometrically necessary dislocations [27–29]. The density of SSDs, ρ_{SSD}, increases proportionally to the accumulated plastic strain according to $\varepsilon_p \approx \rho_{SSD} bd$, where d is the average distance travelled by a dislocation defined as the inverse of the average spacing of obstacles. The GNDs must be arranged to accommodate the incompatibility associated with gradients in the plastic strain field and the density scales as $\varepsilon_p^* \approx \rho_{GND} b$, where $\varepsilon_p^* = \sqrt{\varepsilon_{p,i}\varepsilon_{p,i}}$ are the gradients of plastic strain [10]. Based on the assumption that SSDs and GNDs do not strongly interact, their combined contribution to plastic work can be added and expressed as

$$U_p \approx \sigma_y \left(\rho_{SSD} bd + \rho_{GND} bd\right) \approx \sigma_y \left(\varepsilon_p + \varepsilon_p^* d\right), \tag{2.1}$$

where σ_y is the current material yield stress. The extra storage of the geometrically necessary dislocations will manifest its influence when the characteristic length of deformation is sufficiently small, in the range of d. At this scale, the density of GNDs might dominate the density of SSDs during plastic deformation, and not accounting for their presence will yield an inaccurate estimate for the plastic work from dislocations. Taking the torsion experiments of Fleck et al. [9] in Fig. 1.2 as an example. In torsion of a circular wire, the shear strain γ varies with radius r from the axis of twist so that $\gamma = \kappa r$, where κ is the twist per unit length of wire. The strain gradient $\mathrm{d}\gamma/\mathrm{d}r = \kappa$ introduces a density of GNDs in the order of κ/b. The wire is hardened by both statistically stored and geometrically necessary dislocations giving rise to the observed size effects in torsion in Fig. 1.2.

2.1.2 Ductile fracture

A ductile fracture can be described as a three-stage process with void nucleation, growth, and, ultimately, coalescence [30]. Voids are nucleated at material defects, mostly inclusions, but may also preexist in the material. After initiation, the voids will expand to a volume and shape determined by material properties and applied stress conditions. The voids grow in particular in situations where the stress triaxiality is large. When the voids are large enough, they coalesce to form microcracks and, eventually, a macroscopic crack that will lead to macroscopic failure.

For the work done in this thesis, both void nucleation and coalescence stages are omitted, and, as such, only the growth phase is considered. The question in mind then becomes: *how do these micron-scale voids lead to ductile fracture?*

In situations where diffusion of vacancies cannot account for growth, e.g., at high strain rates or low temperature, dislocations must be involved to account for the movement of material associated with void growth. Two different mechanisms were envisaged by Ashby [27], based on the emission of prismatic or shear dislocation loops, analogous to the concepts of SSDs and GNDs. The mechanism of plastic deformation by prismatic loop emission is shown in Fig. 2.3a. The prismatic dislocation loop carries a spherical calotte causing an increase in the volume of the void by $\pi R^2 b/2$, where R is the void radius, and b is Burger's vector. The shear loop mechanism, shown in Fig. 2.3b, involves the emission of dislocation loops along slip planes. Both prismatic loops and shear loops form preferentially at a plane intersecting the void along a 45° orientation to the equatorial plane. This maximises the shear dislocation's driving force as the shear stresses at 45° to the equatorial plane are maximum. A network of sequentially emitted dislocations may appear during void growth and continuous dislocation emission, as depicted in Fig. 2.4. The network of dislocations from emission of shear loops shown in Fig. 2.4b is analogous to the extra storage of GNDs shown in Figs. 2.1 and 2.2 in Section 2.1.1. The assumption of a far-field hydrostatic stress state means that the shear stresses decay to zero at large distances from the void. The far-field strains are purely elastic, while plastic deformation occurs in regions adjacent to the void surface. Plastic strains must therefore decrease with increasing distance from the void, indicating that gradients, and therefore also size effects, play a part in the void growth process.

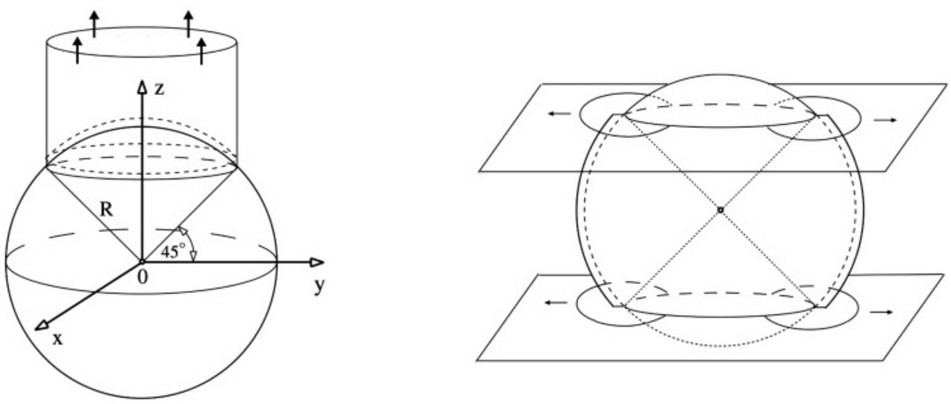

(a) (b)

Figure 2.3. (a) Prismatic dislocation loop of radius $R/\sqrt{2}$ punched out from a spherical void of radius R. (b) Emission of two pairs (four altogether) of dislocation shear loops from the void surface along the indicated slip planes. From [18].

Lubarda et al. [18] presented a criterion for emission of dislocations from the surface of a void analogous to the criterion for crack tip blunting by dislocation emission from Rice and Thomason [31]. The results, shown in Fig. 1.3 under the legend "Lubarda model", revealed that the threshold stress for dislocation emission decreases with increasing void size. A lower stress level is required to emit dislocations from larger than smaller voids. In their studies of void growth through a strain gradient approach, Fleck and Hutchinson [32] and Liu et al. [33] reached the same conclusion. This implies an accelerated void growth by continued emission of prismatic and shear dislocations loops for larger voids at a constant remote stress. The size effects in materials that deform by dislocations movement have important implications where deformation varies significantly in the micrometer range, where the void growth process unfolds. Size effect will therefore inevitably influence void growth and thereby the ductile fracture process.

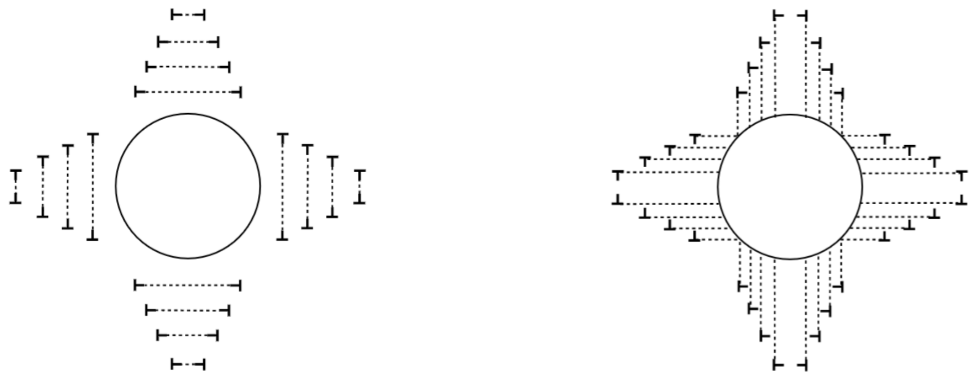

(a) (b)

Figure 2.4. Sequentially emitted dislocations will give networks of dislocations. Top view for dislocation networks due to (a) prismatic dislocation loops and (b) shear loops. From [18].

2.2 Micro-mechanics based continuum models for ductile failure

The first micromechanical models for the development of ductile damage by McClintock [34] and Rice and Tracey [35] described the growth of an isolated cylindrical or spherical void in a rigid, perfectly plastic matrix. Both studies outlined the combined role of stress triaxiality and plastic strain on the ductile void growth. The analysis of spherical voids by Rice and Tracey is more realistic. However, it does not take into account the interaction between voids and the effect of void growth, i.e., softening, on the material behaviour. Later models for porous, ductile solids were based on homogenisation theory. This was first addressed by Gurson [19], who represented damage through the void volume fraction (or porosity), f. The result was the definition of a macroscopic plastic yield criterion, an evolution law for a single microstructural variable, e.g., f, and a flow rule, based on limit analysis of a hollow sphere made of a von Mises material. The Gurson model was later adjusted by Tvergaard [20, 21] to represent the material response predicted by cell model studies better. The Gurson-Tvergaard model has been largely used to simulate the macroscopic response of ductile metals, particularly material failure prediction, for example, in [36–38]. The details of the Gurson-Tvergaard model are presented in Section 3.3. Further reformulations of the Gurson-Tvergaard model have been proposed. Gologanu et al. [22–24] proposed an extension to account for non-spherical void growth in a perfectly plastic material. The reformulated yield criterion is known as the Gologanu-Leblond-Devaux model. It brings exciting features with its ability to represent the evolution of both void shape and porosity into the micro-mechanical framework. The model was later further extended to strain hardening materials by Pardoen and Hutchinson [39]. The details of the Gologanu-Leblond-Devaux model with the extension by Pardoen and Hutchinson are laid out in Section 3.4.

Wavy markings are sometimes found on void walls, resulting from dislocation glide [30]. Despite this, few dislocation models for void growth have been developed. Dislocation dynamics and crystal plasticity are useful tools to gain insight into the fundamental mechanisms of plasticity. However, they are, from a computational point of view, expensive, and there exist significant limits to the size of the volume that can be handled through these approaches. Plastic deformation at the engineering component level is modelled using continuum level isotropic plasticity. However, state-of-the-art modelling techniques of ductile fracture neglect the micron-scale's size effects even though the underlying mechanisms unfold at the micrometer range. The general framework used for the micro-macro transition leaves unresolved the detailed steps over which one averages to arrive at specific constitutive equations incorporating, for example, f. The constitutive models cannot predict the size-dependence at the micron-scale because they do not possess an internal length scale and, hence, predict results independent of sample dimensions. This has been a problem attempted solved by several researchers in recent years. Dormieux and Kondo [40] extended the Gurson-Tvergaard model to incorporate interface surface stresses at the nanoscale and, as such, made the model size-dependent. Monchiet and Bonnet [41] have also proposed an extension to the Gurson-Tvergaard model. Where the traditional Gurson model gives the macroscopic yield criteria for voids in a rigid ideally plastic von Mises material, Monchiet and Bonnet incorporated the void size effect at the macroscopic scale by embedding the voids in a solid matrix not following the von Mises plasticity model but the strain gradient plasticity model by Fleck and Hutchinson [32]. The result was an analytical model for ductile, porous materials containing spherical micro and sub-micron voids. Niordson and Tvergaard [1] proposed a simple transformation of homogenised porous plasticity models to account for the size-dependence of micron-scale voids through two simple extensions to conventional models related to porosity and mean stress, respectively. This extension is discussed in Section 3.3.1.

While analytical models rely on simplifying assumptions and averaging processes, more accurate results may be obtained using numerical methods, such as the finite element (FE) method. A useful configuration for finite element analysis is provided by a 2D square or 3D box containing a single void or family of voids over which periodic boundary conditions (PBCs) are applied, called a unit cell or representative volume element (RVE). The periodic boundary conditions ensure that the square or box satisfies perfect tiling. During a simulation, results need to be calculated for the original square or box only as the PBCs approximate an extensive system consisting of an infinite number of unit cells. As such, the RVE will give a good representation of the whole material behaviour. These studies can help get a better understanding of damage processes, verify analytical solutions, or tune the phenomenological models derived from such solutions. For example, the pioneering work by Needleman [42], settled in work by Koplik and Needleman [43], provided micro-mechanical evidence of the mechanisms for void growth and coalescence and thereby laid the foundation for the development of analytical models. Calculations can be performed with prescribed stresses that allow control of the mean triaxiality ratio. Unit cell model studies for porous materials do not require homogenisation processes as the voids are discretely embedded in a matrix material. Accounting for size effects must therefore happen in the material definition through the plasticity theory applied. A class of such constitutive laws accounting for size effects is called strain gradient plasticity theories.

2.3 Strain gradient plasticity theories

To model plastic deformation on small scales, different alternatives based on the scale of interest exist. For studies interactions between individual dislocations, molecular dynamics models may be suitable. However, if a larger material volume is considered, these models would be prohibitively computationally expensive. Another alternative is to use dislocation dynamics to model a large number of individual dislocations in a crystal. The dislocation dynamics approach cannot handle length scales that approach the atomic dimensions. The limitation for larger scales is that the number of dislocations and the computational requirement, increase with scale. At the continuum scale, length scale effects may be captured with plasticity theory. Strain gradient plasticity (SGP) models have been proposed as extensions to conventional von Mises plasticity theory to small scales. The work of Aifantis [44–47] and Mühlhaus and Aifantis [48] lays the foundation for several different forms of strain gradient plasticity models. The underlying idea is that the yield stress depends on gradients of the plastic strain, which is motivated by the dislocation mechanisms discussed in Section 2.1.1. Here, a connection between plastic deformation and dislocation densities has been made. Statistically stored dislocations depend on plastic strains, while geometrically necessary dislocations depend on the plastic strain gradients, as shown in Eq. (2.1). In a continuum theory, these two contributions can be combined in various ways. The joint effect is that a length parameter is introduced into the material description by multiplication to the plastic strain rate gradient to keep the units consistent. The SGP models are cast in a way that reduces to classic plasticity when the length scale associated with the strain gradients is small compared to the material length parameter, i.e., small gradients for bigger specimen or microstructures.

Strain gradient plasticity formulations can be grouped into *phenomenological* and *mechanism*-based theories. Examples of the latter have been proposed by Gao et al. [49] and Huang et al. [50]. Fleck and Hutchinson [51] developed a *phenomenological* theory with the same structure as the one by Aifantis and Mühlhaus. This was built on previous theories by the same authors [32, 52] and Fleck et al. [9], but with an updated mathematical structure. The SGP theories may also be categorised as function of their order, i.e., with (*higher-order*) or without (*lower-order*) additional stress quantities and boundary conditions. An example of a lower order theory can be found in [53]. The theoretical treatment of higher-order terms may be used to classify the theories as either *work-conjugate* or *non-work-conjugate* [54]. One of the most widely used SGP models is that of Fleck and Hutchinson [51]. This is a *phenomenological, higher-order* theory with higher-order terms introduced as *work-conjugates* to plastic strain gradients in the material formulation. This formulation treats the plastic strains and the displacement components as primary variables in the variational statements of boundary value problems. Unlike its predecessor [32], only the primary variables and their first gradients enter the variational statement, making numerical implementation smooth. This formulation further has length parameters present in the plastic range only. However, the theory was found to violate the thermodynamic requirement that plastic dissipation must always be positive under some non-proportional straining histories. To recover this deficiency, Gudmundson [55] and Gurtin and Anand [56] extended the theory to incorporate both energetic (or recoverable) and dissipative (or unrecoverable) higher-order stresses. Positive plastic work was ensured by introducing a gradient enhanced equivalent plastic strain rate to relate the dissipative higher-order stresses to plastic strain increments [55–57]. However, the presently available strain gradient plasticity models have not been firmly established. Uncertainties regarding the constitutive formulations and how to best capture the effect of the increased density of GNDs associated with non-homogeneous plastic deformation remain. Gudmundson's theory lays the basis for work done for this thesis and is accounted for in Section 3. The theory has been reformulated mathematically in terms of minimum principles by Fleck and Willis [58], given in detail in Section 3, while the numerical implementation is accounted for in Section 4.

3. Material models

This chapter introduces the modelling approaches used for the numerical simulations of porous, ductile media presented in this thesis. The starting point is a presentation of the constitutive equations governing isotropic plastic behaviour of a damage-free material in Sections 3.1 and 3.2. This forms the basis for the subsequent models. Section 3.3 presents the Gurson-Tvergaard (GT) model [19–21], used to simulate isotropic, strain hardening, porous materials with spherical void growth. Then follows a description of the gradient enriched GT model, derived by Niordson and Tvergaard [1], incorporating a material length scale parameter in the constitutive equations. Section 3.4 describes the Gologanu-Leblond-Devaux (GLD) model [24], an extension to the GT model accounting for non-spherical void growth.

Section 3.5 presents the theoretical framework used for the numerical analyses of discrete voids embedded in a strain gradient plasticity governed matrix material, starting with Gudmundson's [55] governing equations. Then follows a description of the constitutive equations and their thermodynamically consistent basis before the solution method, as presented by Fleck and Willis [58], is described.

In the following, general multiaxial stress states are described in terms of a stress tensor, σ_{ij}. A strain tensor, ε_{ij}, describes the state of deformation. The usual index notation is applied, where differentiation in the coordinate system is denoted $()_{,i}$ and $\dot{()}$ implies time differentiation. Latin indices range from 1 to 3, and repeated indices imply summation.

3.1 Plasticity

In the linear theory of elasticity, the stress components are given as simple linear relations of the strain components. It is well known that this gives a good approximation for materials below the yield limit. Most metals, however, show a non-linear behaviour in critical application areas. The boundary between linear and non-linear behaviour is called the yield limit, which forms a yield surface in stress space. Plastic flow theory is used to describe non-linear material behaviour, which cannot be described as reversible. To formulate the flow theory, three ingredients are needed: i) to identify the onset of plastic deformation, *a yield criterion* is necessary. It is useful to determine what can happen to material under multiaxial loading, and the yield criterion must therefore project the multiaxial case to a uniaxial stress-strain curve, which will give the size and shape of the yield surface; ii) to identify whether continued loading occurs, *a flow rule* is needed. At every stage of deformation, the plastic flow rule gives an expression for the changes of the strain components as a function of stress components as part of the constitutive law; iii) finally, the increase in yield stress with continued plastic strain must be specified, given by *a hardening rule*. The hardening rule in which the yield surface expands during plastic deformation preserving its shape, is known as the isotropic hardening model. The models used for this thesis are rate-independent, isotropic materials unless otherwise is specified, characterised by power law-hardening following

$$\sigma_y = \sigma_0 \left(1 + \frac{E^p}{\sigma_0/E}\right)^N, \tag{3.1}$$

where σ_y is the current matrix yield stress, σ_0 is the initial matrix yield stress, E^p is the current plastic strain, E is Young's modulus, and N is the strain hardening exponent.

3.2 J_2 flow theory

The J_2 flow theory describes the plastic response of a non-porous material subject to a multiaxial stress state. It is, in general, assumed that volumetric deformation is elastic and that volume strains are negligible ($\varepsilon^p_{kk} = 0$). This is called plastic incompressibility and allows for removing the volumetric parts from the total stress and strain tensors. This is accomplished by defining deviatoric stress and deviatoric strain tensors as follows:

$$s_{ij} = \sigma_{ij} - \frac{1}{3}\sigma_{kk}\delta_{ij} \quad \text{and} \quad e_{ij} = \varepsilon_{ij} - \frac{1}{3}\varepsilon_{kk}\delta_{ij}, \tag{3.2}$$

where σ_{ij} is the Cauchy stress tensor, ε_{ij} the corresponding strain tensor, and δ_{ij} is the Kronecker delta. Plastic deformation should be characterised only by the components of the deviatoric stress and strain tensors. The J_2 flow theory is governed by the von Mises yield surface, given in a six-dimensional stress space as

$$\Phi = J_2 - (\sigma_e)^2_{\max}, \tag{3.3}$$

where J_2 is defined as $3/2 s_{ij} s_{ij}$ and $(\sigma_e)_{\max}$ is given by $\sqrt{3/2(J_2)_{max}}$, which is the maximum value that the von Mises stress, σ_e, has reached during the deformation history (with initial value σ_0). Stress states within the von Mises yield surface ($\Phi < 0$) dictates an elastic material response, while stress states at the von Mises yield surface ($\Phi = 0$) dictate plastic behaviour.

The total strain increment, ε_{ij}, is assumed to be given as the sum of an elastic part and a plastic part: $\varepsilon_{ij} = \varepsilon^e_{ij} + \varepsilon^p_{ij}$. The stress increment depends linearly on the elastic part of the strain increment, $\dot{\varepsilon}^e_{ij}$, in the elastic region as $\dot{\sigma}_{ij} = \mathcal{L}_{ijkl}\dot{\varepsilon}^e_{ij}$, where the fourth-order tensor $\mathcal{L}_{ijkl}$ is the elastic stiffness tensor given by

$$\mathcal{L}_{ijkl} = \frac{E}{1+\nu}\left[\frac{1}{2}\left(\delta_{ik}\delta_{jl} + \delta_{il}\delta_{jk}\right) - \frac{\nu}{1-2\nu}\delta_{ij}\delta_{kl}\right], \tag{3.4}$$

where ν is the Poisson's ratio. The plastic part of the strain increment, $\dot{\varepsilon}^p_{ij}$, can be written

$$\dot{\varepsilon}^p_{ij} = \beta\frac{9}{4\sigma_e^2}\left(\frac{1}{E_t} - \frac{1}{E}\right) s_{ij} s_{kl} \dot{\sigma}_{kl}, \tag{3.5}$$

where E_t is the tangent modulus for the uniaxial tensile test at the stress level σ_e and β is a measure for whether or not plasticity is initiated in the material given by

$$\beta = \begin{cases} 1, & \text{for} \quad \sigma_e = (\sigma_e)_{\max} \quad \text{and} \quad \dot{\sigma}_e \geq 0 \\ 0, & \text{for} \quad \sigma_e < (\sigma_e)_{\max} \quad \text{or} \quad \dot{\sigma}_e < 0. \end{cases} \tag{3.6}$$

Continuous plasticity occurs if the current matrix stress state is on the yield surface and the effective stress increment is positive; otherwise the material becomes elastic. The relationship between the incremental Cauchy stresses and total incremental strains is given as

$$\dot{\sigma}_{ij} = L_{ijkl}\dot{\varepsilon}_{kl}, \tag{3.7}$$

where the incremental stiffness tensor, L_{ijkl}, is

$$L_{ijkl} = \frac{E}{1+\nu}\left[\frac{1}{2}\left(\delta_{ik}\delta_{jl} + \delta_{il}\delta_{jk}\right) + \frac{\nu}{1-2\nu}\delta_{ij}\delta_{kl} - \beta\frac{3}{2}\frac{E/E_t - 1}{E/E_t - (1-2\nu)/3}\frac{s_{ij}s_{kl}}{\sigma_e^2}\right]. \tag{3.8}$$

3.3 Gurson-Tvergaard material model

The Gurson-Tvergaard (GT) model is an extension of the J_2-flow theory that introduces strong coupling between deformation and damage. It is based on the work of Gurson [19], who formulated a continuum approach to describe a porous material macroscopically using only the void volume fraction, f, to approximately account for damage development. Tvergaard [20, 21] introduced two parameters, q_1 and q_2, to scale the void volume fraction, f, and the stress trace, σ_{kk}, of the original yield surface. These parameters have been estimated to $q_1 = 1.5$ and $q_2 = 1$. Omitting porosity reduces the constitutive relations to J_2 flow theory. The GT yield surface reads

$$\Phi = \frac{\sigma_e^2}{\sigma_M^2} + 2q_1 f\cosh\left(\frac{q_2}{2}\frac{\sigma_{kk}}{\sigma_M}\right) - \left[1 + (q_1 f)^2\right] = 0, \tag{3.9}$$

where $\sigma_e = (3/2 s_{ij}s_{ij})^2$ is the macroscopic equivalent stress, $s_{ij} = \sigma_{ij} - 1/3\delta_{ij}\sigma_{kk}$ is the macroscopic Cauchy stress deviator, and δ_{ij} is the Kronecker delta. The expressions for the macroscopic equivalent stress and Cauchy stress deviator are recognised in Eqs. (3.3) and (3.2). The Gurson modelling approach introduces a macroscopic and a microscopic material level. On the macro-level, the Cauchy stress and strain components are assumed to describe the average fields over the material, including the voids. In contrast, on the micron-level, the matrix material surrounding voids is assumed to follow an isotropic von Mises (J_2) material. A microscopic equivalent reference stress, σ_M, and a microscopic equivalent plastic strain, ε_M^p, are defined. The incremental relationship between them is given by $h_M = \mathrm{d}\sigma_M/\mathrm{d}\varepsilon_M^P$. The macroscopic and microscopic level of the material are coupled by the assumption of an equal plastic work rate on both levels

$$\sigma_{ij}\dot{\varepsilon}_{ij}^p = (1-f)\sigma_M\dot{\varepsilon}_M^p. \tag{3.10}$$

The GT model's constitutive equations can be derived on an incremental form by postulating normality of plastic flow. Following Bishop and Hill [59] and Gurson [19], normality locally within the matrix implies macroscopic normality. The macroscopic plastic strain rate tensor must therefore be normal to the yield surface according to

$$\dot{\varepsilon}_{ij}^p = \Lambda\frac{\partial\Phi}{\partial\sigma_{ij}}, \tag{3.11}$$

where the plastic multiplier, Λ, can be found from the consistency condition during plastic straining, $\dot{\Phi} = 0$. The matrix material satisfies the plastic incompressibility condition, $\varepsilon_{kk}^p = 0$. However, voids presence and growth are associated with volume changes, and the trace of the plastic deformation rate becomes non-zero. As neither void nucleation nor coalescence is considered in the models used for this thesis, the porosity growth rate is taken to be dependent only on the plastic deformation rate through

$$\dot{f} = (1 - f)\dot{\varepsilon}^p_{kk}. \tag{3.12}$$

The total strain increment is given by $\dot{\varepsilon}_{ij} = \dot{\varepsilon}^e_{ij} + \dot{\varepsilon}^p_{ij}$, with the elastic rate of deformation taken to be

$$\dot{\varepsilon}^e_{ij} = \frac{1+\nu}{E}\sigma_{ij} - \frac{\nu}{E}\delta_{ij}\sigma_{kk}, \tag{3.13}$$

while the plastic rate of deformation is given by

$$\dot{\varepsilon}^p_{ij} = \frac{1}{H}n_{ij}n_{kl}\dot{\sigma}_{kl}, \quad \text{with} \quad n_{ij} = \frac{3}{2}\frac{s_{ij}}{\sigma_M} + \alpha\delta_{ij}, \tag{3.14}$$

where H is given by

$$H = \frac{h_M}{1-f}\left(\frac{\sigma_e^2}{\sigma_M^2} + \alpha\frac{\sigma_{kk}}{\sigma_M}\right)^2 - 3\sigma_M(1-f)\alpha\gamma, \tag{3.15}$$

and α and γ are defined as follows

$$\alpha = \frac{1}{2}q_1 q_2 f \sinh\left(\frac{q_2}{2}\frac{\sigma_{kk}}{\sigma_M}\right), \tag{3.16}$$

$$\gamma = q_1 \cosh\left(\frac{q_2}{2}\frac{\sigma_{kk}}{\sigma_M}\right) - q_1^2 f \tag{3.17}$$

Adding the elastic and plastic rate of deformation, and inverting, gives the following relation between the stress and strain increment

$$\dot{\sigma}_{ij} = \mathbb{L}_{ijkl}\dot{\varepsilon}_{ij}, \tag{3.18}$$

with $\mathbb{L}_{ijkl}$

$$\mathbb{L}_{ijkl} = \mathcal{L}_{ijkl} - \mu M_{ij}M_{kl}, \tag{3.19}$$

where $\mathcal{L}_{ijkl}$ is the elastic stiffness tensor, while M_{ij} and μ are given by

$$M_{ij} = \mathcal{L}_{ijkl}n_{kl}, \quad \mu = \frac{1}{H + \mathcal{L}_{ijkl}n_{ij}n_{kl}}. \tag{3.20}$$

3.3.1 Gradient enriched Gurson-Tvergaard material model

Niordson and Tvergaard [1] investigated size-dependent yield surfaces for porous materials and found that for size-dependent material behaviour the yield surfaces intersect the von Mises stress axis at increasing values as the size of the voids decreases, and that size-dependent yield surfaces are stretched significantly along the mean stress axis. This led to the suggestion that the yield surface of a size-dependent material could model as the yield surface of a conventional material with a smaller void volume fraction and less mean stress sensitivity. They estimated with good approximations from the conventional yield surface using two size-dependent parameters, Q_1 and Q_2, that scale the void volume fraction and mean stress, respectively, depending on void size. The parameters, Q_1 and Q_2 are always less than or equal to 1, dependent on the size of the voids, and given by

$$Q_1 \approx \frac{0.364}{1 + 1.8\left(\frac{L_D}{r_v}\right) + 10\left(\frac{L_D}{r_v}\right)^2} + 0.636 \tag{3.21}$$

$$Q_2 \approx \frac{1}{1 + 1.8 \left(\frac{L_D}{r_v}\right)^{3/2}}, \tag{3.22}$$

where L_D is a dissipative material length scale parameter, and r_v is the current mean void size. A phenomenological interpretation of L_D is given in Section 3.5. The fraction L_D/r_v is given by the initial void radius, r_0, the initial void volume fraction, f_0 and the current void volume fraction, f, through

$$\frac{L_D}{r_v} = \frac{L_D}{r_0}\left(\frac{f_0}{f}\right)^{1/3}. \tag{3.23}$$

Following this, the GT yield surface previously defined by $\Phi = \Phi(\sigma_e, \sigma_{ij}, f, \sigma_m)$, can be transformed into a size-dependent counterpart following the transformation $\Phi = \Phi(\sigma_e, \sigma_{ij}, Q_1 f, Q_2\sigma_m)$ written as

$$\Phi = \frac{\sigma_e^2}{\sigma_M^2} + 2Q_1 q_1 f \cosh\left(\frac{Q_2 q_2}{2}\frac{\sigma_{kk}}{\sigma_M}\right) - [1 + (Q_1 q_1 f)^2] = 0 \tag{3.24}$$

The gradient enriched GT model will have two extra terms in the consistency condition, which gives

$$\dot{\Phi} = \frac{\partial \Phi}{\partial \sigma_{ij}}\dot{\sigma}_{ij} + \frac{\partial \Phi}{\partial \sigma_m}\dot{\sigma}_m + \frac{\partial \Phi}{\partial f}\dot{f} + \frac{\partial \Phi}{\partial Q_1}\dot{Q}_1 + \frac{\partial \Phi}{\partial Q_2}\dot{Q}_2 = 0 \tag{3.25}$$

where $\frac{\partial \Phi}{\partial Q_1}\dot{Q}_1$ and $\frac{\partial \Phi}{\partial Q_2}\dot{Q}_2$ can be expressed through $\dot{f}$ as $\frac{\partial \Phi}{\partial Q_1}\frac{\partial Q_1}{\partial f}\dot{f}$ and $\frac{\partial \Phi}{\partial Q_2}\frac{\partial Q_2}{\partial f}\dot{f}$, so that H, following the same derivation as in Section 3.3, can be expressed as

$$H = \frac{h_M}{1-f}\left(\frac{\sigma_e^2}{\sigma_M^2} + \alpha\frac{\sigma_{kk}}{\sigma_M}\right)^2 - 3\sigma_m(1-f)\alpha\left[\gamma\left(1 + \frac{f}{q_1}\frac{\partial Q_1}{\partial f}\right) + \frac{\sigma_{kk}}{\sigma_M}\alpha\frac{1}{q_2}\frac{\partial Q_2}{\partial f}\right] \tag{3.26}$$

with α, γ, $\frac{\partial Q_1}{\partial f}$ and $\frac{\partial Q_2}{\partial f}$ given by

$$\alpha = \frac{1}{2}Q_1 q_1 Q_2 q_2 f \sinh\left(\frac{Q_2 q_2}{2}\frac{\sigma_{kk}}{\sigma_M}\right) \tag{3.27}$$

$$\gamma = Q_1 q_1 \cosh\left(\frac{Q_2 q_2}{2}\frac{\sigma_{kk}}{\sigma_M}\right) - (Q_1 q_1)^2 f \tag{3.28}$$

$$\frac{\partial Q_1}{\partial f} = \frac{0.364\left[1.8\frac{L_D}{r_v} + 20\left(\frac{L_D}{r_v}\right)^2\right]}{3f\left[1 + 1.8\frac{L_D}{r_v} + 10\left(\frac{L_D}{r_v}\right)^2\right]^2} \tag{3.29}$$

$$\frac{\partial Q_2}{\partial f} = \frac{0.9\left(\frac{L_D}{r_v}\right)^{3/2}}{f\left[1 + 1.8\left(\frac{L_D}{r_v}\right)^{3/2}\right]^2} \tag{3.30}$$

3.4 Gologanu-Leblond-Devaux material model

To deal with the limitation of spherical void growth in the Gurson model, Gologanu et al. [22–24] reformulated the model to account for the growth of spheroidal voids[1] in perfectly plastic material. This new model has become known as the Gologanu-Leblond-Devaux (GLD) model. The GLD model includes four elements: a macroscopic yield criterion, $\Phi = 0$, depending upon porosity, f, and void shape, S, a macroscopic flow rule obeying the normality property, Eq. (3.11), and evolution equations for the porosity, $\dot{f}$, and the void shape parameter, $\dot{S}$. The void shape parameter is given by $S = \ln(W) \equiv \ln(a/b)$, where a and b are illustrated in Fig. 3.1. The GLD model allows for micromechanical analysis of spheroidal voids along the lines of the Gurson analysis leading to the following yield surface for the GLD model:

$$\Phi = C\frac{B_0^2}{\sigma_M^2} + 2q(g+1)(g+f)\cosh\left(\kappa\frac{\sigma_{gh}}{\sigma_M}\right) - (g+1)^2 - q^2(g+f)^2. \tag{3.31}$$

where B_0 is given by $B_0 = 3/2\hat{s}_{ij}\hat{s}_{ij}$ with $\hat{s}_{ij} = \eta\sigma_{gh}X_{ij}$ where σ_{gh} is generalised hydrostatic stress defined by $\sigma_{gh} = \sigma_{ij}J_{ij}$. The Cauchy stress is given by σ_{ij} and s_{ij} its deviatoric part. The tensors X_{ij} and J_{ij} are associated with the void axis and defined as

$$X_{ij} = 2/3e_x \otimes e_x - 1/3e_y \otimes e_y - 1/3e_z \otimes e_z \tag{3.32}$$
$$J_{ij} = (1-2\alpha_2)e_x \otimes e_x + \alpha_2 e_y \otimes e_y + \alpha_2 e_z \otimes e_z \tag{3.33}$$

where e_x is the base vector parallel to the cavity axis. Gologanu et al. [24] derived analytical relationships for the parameters C, η, g, κ, h_1, h_2, α_2 in terms of the state variables f and W. The relations can be found in Appendix A.1. The parameter g can be viewed as a "second porosity". Finally, q is the analogue of the heuristic parameter q_1 in the GT model calibrated as a function of f_0 and W_0 and the strain hardening capacity of the material (exponent N) introduced by Pardoen and Hutchinson [39]. The expressions used for q in this work are given in Appendix A.1.

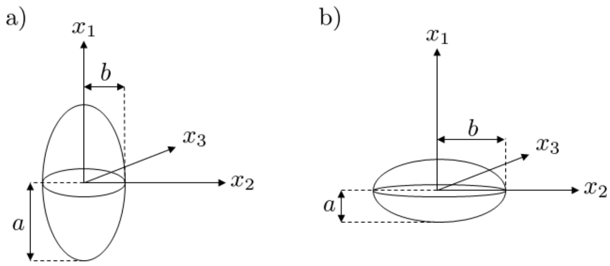

Figure 3.1. Void geometry for (a) Prolate void, $S = \ln\left(\frac{a}{b}\right) > 0$, (b) Oblate void, $S = \ln\left(\frac{a}{b}\right) < 0$.

The evolution of void growth follows that of the GT model with $\dot{f} = (1-f)\dot{\varepsilon}^p_{kk}$, while the evolution law for the void shape is given by

$$\dot{S} = \frac{3}{2}(1+h_1 h_T)\left(\dot{\varepsilon}^p_{ij} - \frac{\dot{\varepsilon}^p_{kk}}{3}\delta_{ij}\right)P_{ij} + h_2\dot{\varepsilon}^p_{ij}, \tag{3.34}$$

where P_{ij} is a projector tensor defined by $e_x \otimes e_x$, δ_{ij} is the Kronecker delta. The parameters h_1 and h_2 depend on the void shape and are given in Appendix A.1. The parameter h_T depends on triaxiality and is also given in Appendix A.1.

[1]Ellipsoid with symmetry of revolution around one axis.

The GLD model follows the coupled plastic work rate of the macroscopic and microscopic material levels given by Eq. (3.10) and the requirement for normality according to Eq. (3.11). Following Pardoen [60] and defining

$$\mu_{ij} = \frac{\partial \Phi}{\partial \sigma_{ij}} \tag{3.35}$$

$$m_{ij} = \mathcal{L}_{ijkl}\mu_{kl}, \tag{3.36}$$

the consistency condition, $\dot{\Phi} = 0$, will give

$$A = -\left[\frac{h_M}{1-f}\frac{\sigma_{ij}}{\sigma_y}\frac{\partial\Phi}{\partial\sigma_{ij}}\frac{\partial\Phi}{\partial\sigma_y} + \left(\frac{3}{2}(1+h_1 h_T)\left(\frac{\partial\Phi}{\partial\sigma_{ij}} - \frac{1}{3}\frac{\partial\Phi}{\partial\sigma_{kk}}\delta_{ij}\right)P_{ij} \right.\right.$$
$$\left.\left. + \, h_2\frac{\partial\Phi}{\partial\sigma_{kk}}\right)\frac{\partial\Phi}{\partial S} + (1-f)\frac{\partial\Phi}{\partial\sigma_{kk}}\frac{\partial\Phi}{\partial f}\right], \tag{3.37}$$

where the yield surface derivatives are given in Appendix A.2. The relation between the stress and the strain increment given by Eq. (3.18) where $\mathbb{L}_{ijkl}$ is given by

$$\mathbb{L}_{ijkl} = \mathcal{L}_{ijkl} - \frac{m_{ij}m_{kl}}{A + \mu_{mn}m_{mn}}. \tag{3.38}$$

3.5 Strain gradient plasticity

The models presented thus far rely on a local evaluation of material behaviour. When constructing a material model, a resolution level is selected, e.g., micron-scale, mesoscale, or macroscale. It is only phenomena larger than the scale of resolution that is explicitly represented in a model. The microscopic length scale, for example, is represented by a length scale parameter in a macro scale model. If changes in the deformation field under loading are greater than the resolution level, a conventional continuum mechanics approach is adequate. However, if such changes are below the resolution level, some enhancement to the model must be made to adequately capture real phenomena. Nonlocality provides such an enhancement, such as the isotropic, visco-plastic strain gradient plasticity model proposed by Gudmundson [55]. This has been implemented in the mathematical formulation context in terms of minimum principles as proposed by Fleck and Willis [58].

In a small strain formulation, the total strain rate is determined from the gradients of displacement rates: $\dot{\varepsilon}_{ij} = (\dot{u}_{i,j} + \dot{u}_{j,i})/2$, and decomposes into an elastic part and a plastic part so that: $\dot{\varepsilon}_{ij} = \dot{\varepsilon}^e_{ij} + \dot{\varepsilon}^p_{ij}$. The starting point for the strain gradient plasticity model, involving higher-order stresses, is the principle of virtual work, which can be written as

$$\int_V \left(\sigma_{ij}\delta\epsilon_{ij} + (q_{ij} - s_{ij})\delta\epsilon^p_{ij} + \tau_{ijk}\delta\epsilon^p_{ij,k}\right)\mathrm{d}V = \int_S \left(T_i\delta u_i + t_{ij}\delta\epsilon^p_{ij}\right)\mathrm{d}S, \tag{3.39}$$

where σ_{ij} is the Cauchy stress, $s_{ij} = \sigma_{ij} - 1/3\delta_{ij}\sigma_{kk}$ its deviatoric part, q_{ij} is the so-called micro-stress tensor (work conjugate to the plastic strain, ε^p_{ij}) and τ_{ijk} is the higher-order stress tensor (work conjugate to the plastic strain gradients, $\varepsilon^p_{ij,k}$). The right-hand side of Eq. (3.39) includes both conventional tractions, $T_i = \sigma_{ij}n_j$, and higher-order terms, $t_{ij} = \tau_{ijk}n_k$, with n_k denoting the outward normal to the surface S, which bounds the volume V. It should be noted that by omitting gradient effects, the first term on both the left- and right-hand side of Eq. (3.39), revert to those of the conventional principle of virtual work.

Applying the product rule and Gauss' divergence theorem to the left-hand side of Eq. (3.39), the internal virtual work, gives

$$\delta W_{\text{internal}} = \int_S \left(\sigma_{ij} n_j \delta u_i + \tau_{ijk} n_k \delta \varepsilon^p_{ij}\right) \mathrm{d}S - \int_V \left(\sigma_{ij,j} \delta u_i + (\tau_{ijk,k} + s_{ij} - q_{ij}) \delta \varepsilon^p_{ij}\right) \mathrm{d}V. \quad (3.40)$$

The first integral on the right-hand side of Eq. (3.40) may be identified as part of the external virtual work, as the conventional equilibrium equation in the absence of body forces. The second term of the integral on the right-hand side of Eq. (3.40) should vanish for arbitrary variations, meaning that two sets of equilibrium equations can be obtained

$$\sigma_{ij,j} = 0 \quad \text{and} \quad \tau_{ijk,k} + s_{ij} - q_{ij} = 0. \quad (3.41)$$

The second equation is the higher-order equilibrium equation that shows that in the presence of higher-order stresses, τ_{ijk}, the micro-stress q_{ij} and the stress-deviator s_{ij} are in general different. Thus, by accounting for the right-hand side of Eq. (3.39), the corresponding conventional $T_{ij} = \sigma_{ij} n_j$ and higher-order $t_{ij} = \tau_{ijk} n_k$ boundary conditions can be obtained.

Given Eq. (3.39) and the Clausius-Duhem inequality, also known as the principle of dissipation, the local free-energy inequality can be expressed as

$$\sigma_{ij} \dot{\varepsilon}^e_{ij} + q_{ij} \dot{\varepsilon}^p_{ij} + \tau_{ijk} \dot{\varepsilon}^p_{ij,k} - \dot{\Psi} \geq 0, \quad (3.42)$$

where the time derivative of the Helmholtz free energy is given by

$$\dot{\Psi} = \frac{\partial \Psi}{\partial \varepsilon^e_{ij}} \dot{\varepsilon}^e_{ij} + \frac{\partial \Psi}{\partial \varepsilon^p_{ij}} \dot{\varepsilon}^p_{ij} + \frac{\partial \Psi}{\partial \varepsilon^p_{ij,k}} \dot{\varepsilon}^p_{ij,k}, \quad (3.43)$$

which accordingly will give the following imbalance, which must be fulfilled by the appropriate constitutive relations

$$\left(\sigma_{ij} - \frac{\partial \Psi}{\partial \varepsilon^e_{ij}}\right) \dot{\varepsilon}^e_{ij} + \left(q_{ij} - \frac{\partial \Psi}{\partial \varepsilon^p_{ij}}\right) \dot{\varepsilon}^p_{ij} + \left(\tau_{ij} - \frac{\partial \Psi}{\partial \varepsilon^p_{ij,k}}\right) \dot{\varepsilon}^p_{ij,k} \geq 0. \quad (3.44)$$

Plastic deformation is generally considered a dissipative process, and no free energy associated with the plastic strain itself is introduced to the free energy expression. Following [55], it is assumed that free energy is stored due to elastic strain, $\varepsilon^e_{ij} = \varepsilon_{ij} - \varepsilon^p_{ij}$, and gradients of plastic strain, but not due to plastic strain itself, i.e. the free energy is given by $\Psi = \Psi(\varepsilon^e_{ij}, \varepsilon^p_{ij,k}) = \Psi(\varepsilon_{ij} - \varepsilon^p_{ij}, \varepsilon^p_{ij,k})$. This renders the micro-stresses with a dissipative part only, $q_{ij} = q^D_{ij}$, while the higher-order stresses, τ_{ijk}, decompose into a dissipative part, τ^D_{ijk}, and an energetic part, τ^E_{ijk}, so that $\tau_{ijk} = \tau^D_{ijk} + \tau^E_{ijk}$. The free energy accounting for conventional stresses and energetic higher-order stresses is given according to the isotropic expression

$$\Psi = \frac{1}{2} \left(\varepsilon_{ij} - \varepsilon^p_{ij}\right) \mathcal{L}_{ijkl} \left(\varepsilon_{kl} - \varepsilon^p_{kl}\right) + \frac{1}{2} G (L_E)^2 \varepsilon^p_{ij,k} \varepsilon^p_{ij,k}, \quad (3.45)$$

where $\mathcal{L}_{ijkl}$ is the elastic stiffness tensor, G is the elastic shear modulus, and L_E is an energetic length scale parameter. The conventional stresses are readily obtained through the elastic relationship

$$\sigma_{ij} = \frac{\partial \Psi}{\partial \varepsilon^e_{ij}} = \mathcal{L}_{ijkl} (\varepsilon_{kl} - \varepsilon^p_{kl}), \quad (3.46)$$

and the energetic higher-order stresses are derived as

$$\tau^E_{ijk} = \frac{\partial \Psi}{\partial \varepsilon^p_{ij,k}} = G(L_E)^2 \varepsilon^p_{ij,k}. \tag{3.47}$$

For the dissipative contribution, the micro stresses, q^D_{ij}, and the dissipative part of the higher-order stress, τ^D_{ijk}, Eq. (3.44) can be rewritten as

$$q^D_{ij}\dot{\varepsilon}^p_{ij} + \tau^D_{ijk}\dot{\varepsilon}^p_{ij,k} \geq 0, \tag{3.48}$$

called the dissipation inequality, where, for the last two terms, the following replacements have been done: $q^D_{ij} = (q_{ij} - \partial\Psi/\partial\varepsilon^p_{ij})$ and $\tau^D_{ijk} = (\tau_{ijk} - \partial\Psi/\partial\varepsilon^p_{ij,k})$, respectively. The first term of the dissipation inequality will never violate the second law of thermodynamics as the plastic strain rate, $\dot{\varepsilon}^p_{ij}$, enters twice, and the term will be inherently positive. However, the second term may be negative for strongly non-proportional loading histories when the stored energy associated with plastic strain gradients is released, which, from a thermodynamics point of view, is not allowed. This is the case for the theory by Fleck and Hutchinson [51] mentioned in Section 2.3, where the higher-order stresses are purely dissipative: $\tau_{ijk} = \tau^D_{ijk}$. Several methods have been proposed to ensure positive plastic work. One suggestion is to adopt a purely energetic formula, i.e. setting $\tau^E_{ijk} = \tau_{ijk}$ and $\tau^D_{ijk} = 0$. This, however, requires the material to have a constant tangent modulus, which is generally not a realistic restriction for a plasticity model. From a physical point of view, it also seems likely that some of the work associated with τ_{ijk} should be dissipative. The source of dissipative effects may be ascribed to the movement of dislocations, through which resistance to dislocation motion may be translated into increased yield strength. Energetic effects, however, may be associated with dislocation networks that lead to an increase in strain hardening. The mechanisms associated with GNDs, discussed in Section 2.1.1, have been incorporated into the higher-order theory by incorporating both dissipative and energetic higher-order stresses in the constitutive equations. At large length scales, where the density of SSDs is large compared to GNDs, all energy associated with plastic deformation is dissipated. At smaller length scales, however, when gradients are strong, GNDs are stored, giving rise to free energy associated with the local stress fields of the dislocations, and increased dissipation with the motion of the GNDs [61, 62]. For all work in this thesis, the energetic terms are omitted and only the dissipative contribution is considered. The orientation of the energetic contributions is given for consistency.

A class of constitutive equations incorporating the dissipative higher-order stresses in a thermodynamically consistent manner, was constructed by Gudmundson [55] and Gurtin and Anand [56]. As mentioned in the introduction of Section 3.5, the work in this thesis is based on the work of Gudmundson [55]. The theory introduces an effective stress, σ_c, work conjugate to the gradient enhanced effective plastic strain rate, $\dot{E}^p$, ensuring that the plastic work rate

$$\sigma_c \dot{E}^p = q_{ij}\dot{\varepsilon}^p_{ij} + \tau^D_{ijk}\dot{\varepsilon}^p_{ij,k} \tag{3.49}$$

is always positive by relating the dissipative stress quantities, q^D_{ij} and τ^D_{ijk}, to increments of strain. The expressions for σ_c and $\dot{E}^p$ read

$$\sigma_c = \sqrt{\frac{3}{2}q^D_{ij}q^D_{ij} + L_D^{-2}\tau^D_{ijk}\tau^D_{ijk}} \quad \text{and} \quad \dot{E}^p = \sqrt{\frac{2}{3}\dot{\varepsilon}^p_{ij}\dot{\varepsilon}^p_{ij} + L_D^2\dot{\varepsilon}^p_{ij,k}\dot{\varepsilon}^p_{ij,k}}, \tag{3.50}$$

where L_D is a dissipative length scale parameter. The corresponding dissipative stress quantities, the dissipative micro-stresses and higher-order stresses, in terms of increments of strain are readily obtained:

$$q_{ij}^D = \frac{2}{3}\frac{\sigma_c}{\dot{E}^p}\dot{\varepsilon}_{ij}^p \quad \text{and} \quad \tau_{ijk}^D = \frac{\sigma_c}{\dot{E}^p} L_D^2 \dot{\varepsilon}_{ij,k}^p. \tag{3.51}$$

In rate-dependent J_2 flow theory, the material behaviour can be described by a simple power-law expression on the form

$$\sigma_c\left[\dot{E}^p, E^p\right] = \sigma_y(E^p)\left(\frac{\dot{E}^p}{\dot{\varepsilon}_0}\right)^m, \tag{3.52}$$

where σ_y is the current matrix yield stress, given by, for example, Eq. (3.1), $\dot{\varepsilon}_0$ is a reference strain rate, m is the viscoplastic strain rate sensitivity exponent, and σ_c is the effective stress. For the work in this thesis, the materials are approximated rate-independent by employing a sufficiently small strain rate sensitivity exponent to approach the rate-independent limit. To account for dissipative terms, a visco-plastic potential is defined as

$$\Phi\left[\dot{E}^p, E^p\right] = \int_0^{\dot{E}^p} \sigma_c\left[\dot{E}^p, E^p\right] \mathrm{d}\dot{E}^p, \tag{3.53}$$

where $\sigma_c[\dot{E}^p, E^p]$ is given by Eq. (3.52). To complete the higher-order theory, Fleck and Willis [58] put forward two minimum principles that deliver the incremental solutions to the displacement field and plastic strain rate field, respectively. Assuming that the current stress/strain state is known in terms of the displacement, u_i, and plastic strain, ε_{ij}^p, fields, the plastic strain rate field in the subsequent load increment can be determined from Minimum Principle I (MPI):

$$H = \inf_{\dot{\varepsilon}_{ij}^p} \int_V (\Phi[\dot{\varepsilon}_{ij}^p] + \tau_{ijk}^E \dot{\varepsilon}_{ij,k}^p - s_{ij}\dot{\varepsilon}_{ij}^p)\mathrm{d}V - \int_S t_{ij}\dot{\varepsilon}_{ij}^p \mathrm{d}S, \tag{3.54}$$

which includes the viscoplastic potential function, meaning that the plastic strain rate directly depends on MPI through the hardening rule given by Eq. (3.52). The minimum principle in Eq. (3.54) therefore delivers the actual plastic strain rate field, $\dot{\varepsilon}_{ij}^p$. Stationarity of MPI ($\delta H[\dot{\varepsilon}_{ij}^p] = 0$) results in

$$\int_V \left(q_{ij}^D \delta\dot{\varepsilon}_{ij}^p + \tau_{ijk}^D \delta\dot{\varepsilon}_{ij,k}^p\right) \mathrm{d}V = \int_V \left(s_{ij}\delta\dot{\varepsilon}_{ij}^p - \tau_{ijk}^E \delta\dot{\varepsilon}_{ij,k}^p\right) \mathrm{d}V + \int_S t_{ij}\delta\dot{\varepsilon}_{ij}^p \mathrm{d}S, \tag{3.55}$$

as the variation of the viscoplastic potential gives

$$\delta\Phi = \sigma_c[\dot{E}^p, E^p]\delta\dot{E}^p = \frac{2}{3}\frac{\sigma_c[\dot{E}^p, E^p]}{\dot{E}^p}\dot{\varepsilon}_{ij}^p\delta\dot{\varepsilon}_{ij}^p + \frac{\sigma_c[\dot{E}^p, E^p]}{\dot{E}^p} L_D^2 \dot{\varepsilon}_{ij,k}^p \dot{\varepsilon}_{ij,k}^p = q_{ij}^D \delta\dot{\varepsilon}_{ij}^p + \tau_{ijk}^D \delta\dot{\varepsilon}_{ij,k}^p \tag{3.56}$$

Fulfilling this variational statement will lead to solutions satisfying the higher-order equilibrium equation. By introducing the constitutive equations and requiring that the variational statement hold for any admissible plastic strain rate field, $\delta\dot{\varepsilon}_{ij}^p$, a discretized non-linear system of equations can be obtained, given in Eq. (4.4).

Having determined the plastic strain rate field, the incremental solution for the displacement field is readily obtained from Minimum Principle II (MPII) from Fleck and Willis [58]. The standard functional can be written as

$$J[\dot{u}_i] = \frac{1}{2}\int_V \mathcal{L}_{ijkl}(\dot{\varepsilon}_{ij} - \dot{\varepsilon}_{ij}^p)(\dot{\varepsilon}_{kl} - \dot{\varepsilon}_{kl}^p)\mathrm{d}V - \int_S \dot{T}_i \dot{u}_i \mathrm{d}S \tag{3.57}$$

where $\mathcal{L}_{ijkl}$ is the elastic stiffness tensor. Stationarity of MPII ($\delta J[\dot{u}_i] = 0$) gives the following requirement

$$\int_V \mathcal{L}_{ijkl}(\dot{\epsilon}_{ij} - \dot{\epsilon}_{ij}^P)(\delta\dot{\epsilon}_{kl} - \delta\dot{\epsilon}_{kl}^p)\mathrm{d}V = \int_S \dot{T}\delta\dot{u}_i\mathrm{d}S \tag{3.58}$$

which must hold for any kinematically admissible incremental displacement field, $\delta\dot{u}_i$. The discretised equations will deliver the actual velocity field, $\dot{u}_i$, consistent with the plastic strain rate field found from MPI.

4. Numerical implementation

The work in this thesis is numerical and uses several different implementations to predict the ductile response of voided metals. This chapter goes through the different numerical implementations of the material models presented in Section 3, which span from direct implementation of a single-point model, to a finite element implementation in an in-house FORTRAN code to commercial finite element software. Several types of models are used in conjunction with the implementations, and an overview of these will be given as well.

4.1 Single-point continuum models

The gradient enriched Gurson-Tvergaard model has been implemented for a single point representing a voided continuum with damage represented through the void volume fraction f. The constitutive equations have been implemented in MATLAB and solved directly by forward Euler integration of an imposed stress/strain history. A Rayleigh-Ritz method is employed to ensure a constant ratio of transverse to axial stresses for each increment with a prescribed displacement. The stress state is considered axi-symmetric, and the ratio of transverse to axial stresses is given by the parameter ρ defined as

$$\rho = \frac{\sigma_{22}}{\sigma_{11}}, \tag{4.1}$$

where ρ is prescribed, and σ_{11} is the stress along the main loading axis. Axi-symmetric conditions give $\sigma_{11} > \sigma_{22}$. The stress triaxiality is related to the stress ratio through

$$T = \frac{1}{3}\left[\frac{1+2\rho}{1-\rho}\right]. \tag{4.2}$$

The mechanical response from the Gurson-Tvergaard model should be frame-indifferent and the stress-rate objective. To achieve this, the Jaumann stress rate, $\overset{\triangledown}{\sigma}_{ij}$, is typically used to calculate the deformation rate and enters Eq. (3.13). However, for the single-point model there is no distinction between the deformed and reference configurations. Rigid body deformations can be omitted from the implementation as the spin tensor is zero. Therefore, the incremental Cauchy stress may be used directly in Eq. (3.13), instead of the Jaumann stress rate. To represent a continuum with damage expressed through both void volume fraction, f, and void shape, S, the Gologanu-Leblond-Devaux model has been implemented for a one-point model analogous to the implementation of the enriched Gurson-Tvergaard model.

4.2 Axi-symmetric unit cells

The results from the single-point continuum models have been compared to corresponding simulations of discrete voids in a gradient enriched material matrix of the Fleck and Willis [63] type. An axi-symmetric approximation of a unit cell with a single void has been used. This is explained further in Section 5.1. A schematic view of axi-symmetric representations of cells with voids of different initial void radius is given in Fig. 4.1. A Rayleigh-Ritz procedure has been employed to ensure that a constant ratio, ρ, of transverse to axial stress, given in Eq. (4.1), is

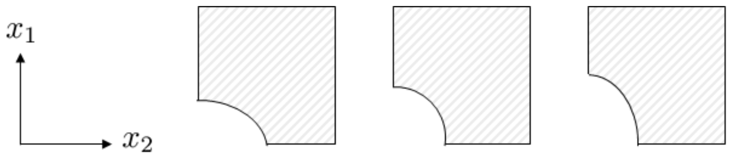

Figure 4.1. Axi-symmetric approximations with different initial void shapes.

maintained throughout the simulation. The Rayleigh Ritz method uses three degrees of freedom, Δ_1 and Δ_2, which control the cell's outer dimensions, and a visco-plastic multiplier as the third. The boundary value problems of discretely voided unit cells have been solved using the Finite Element (FE) method based on the two minimum principles proposed by Fleck and Willis [58], introduced in Section 3.5. A forward Euler integration scheme has been built into an in-house FORTRAN code using a finite strain set up. To determine the displacement field, eight-node, isoparametric, axi-symmetric elements are used, whereas corresponding four-node elements are used for the plastic strain rate field. The standard finite element interpolation approximates the field variables through

$$\dot{u}_i = \sum_{n=1}^{N_I} N_i^{(n)} \dot{U}^{(n)} \quad \text{and} \quad \dot{\epsilon}^p_{ij} = \sum_{n=1}^{N_{II}} M_{ij}^{(n)} \dot{\epsilon}^{p(n)}, \tag{4.3}$$

where $N_i^{(n)}$ are quadratic shape functions for the displacement field and $M_{ij}^{(n)}$ are linear shape functions for the plastic strain rate field. Here, $i, j = 1, 2, 3$ refers to the components of the vector-fields, N_I and N_{II} are the numbers of degrees of freedom and $\dot{U}^{(n)}$, $\dot{\epsilon}^{p(n)}$ holds the nodal values of the unknown rate field variables. The discretised version of Eq. (3.55) gives

$$\int_V \frac{\sigma_c}{\dot{E}^p} \left(\frac{2}{3} M_{ij}^{(n)} M_{ij}^{(m)} + L_D^2 M_{ij,k}^{(n)} M_{ij,k}^{(m)} \right) \mathrm{d}V \cdot \dot{\varepsilon}^{p(m)} = \int_V \left(s_{ij} M_{ij}^{(n)} - \tau^E_{ijk} M_{ij,k}^{(n)} \right) \mathrm{d}V + \int_S t_{ij} M_{ij}^{(n)} \mathrm{d}S, \tag{4.4}$$

which is solved iteratively to obtain the plastic strain rate field. The converged solution is then used to determine the incremental displacement solution found through the discretised form of Eq. (3.58) stated as

$$\int_V L_{ijkl} B_{ij}^{(n)} B_{kl}^{(m)} \mathrm{d}V \cdot \dot{u} = \int_V L_{ijkl} B_{ij}^{(n)} \dot{\epsilon}^p_{kl} \mathrm{d}V - \int_S \dot{T}_i N_i^{(n)} \mathrm{d}S \tag{4.5}$$

where $B_{ij}^{(n)} = (N_{i,j}^{(n)} + N_{j,i}^{(n)})/2$ are the strain displacement functions.

4.3 Three dimensional unit cells

To directly investigate the effect of plastic strain gradients on the ductile fracture process at the micron-scale, three-dimensional unit cells with discrete voids have been analysed. The combined effect of void size and spacing has been investigated by simulation of arrays of initially spherical voids of equal size under different imposed loading conditions. Due to symmetry, the arrays are approximated by 1/8 cuboids, as shown in Fig. 4.2, where the aspect ratio of the cuboid can change to ensure different void spacings in different directions. Symmetry boundary conditions are applied to the three of the faces of the cell containing the void to mimic the behaviour of a full cell. The voids are embedded in a strain gradient enhanced material matrix allowing for the investigation of size effects. The boundary value problems have been solved using the commercial

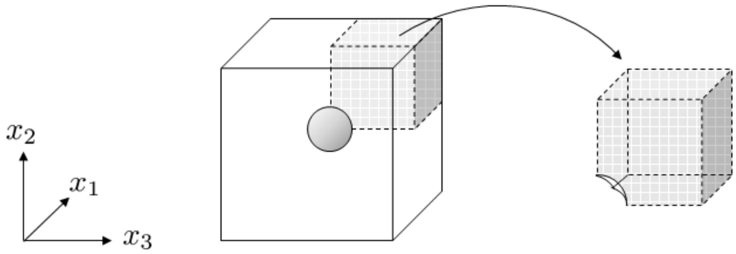

Figure 4.2. Three-dimensional, voided unit cell. Symmetry opens for 1/8 cube being modelled. Changing the aspect ratio of the unit cell will give different void spacings.

finite element solver ABAQUS. The strain gradient plasticity theory given by Fleck and Willis [58] is implemented as a user element subroutine (UEL) in a backward Euler framework. A small strain formulation is employed. The reader is referred to [64] for further details on the implementation.

The unit cells employ user elements corresponding to the general-purpose twenty-node quadratic brick element with reduced integration (C3D20R) in the ABAQUS library. The reduced integration gives 2x2x2 integration points. The UEL subroutine will be called for each element in the mesh every time element calculations are required. The loading conditions have been fixed by enforcing constant ratios between normal stress components throughout deformation history. For 3D configurations, stress ratios relating stress in all three principal directions must be defined. For conditions with σ_{11} as the stress along the main loading axis, the stress ratios in the two other principal directions are given by

$$\rho_2 = \frac{\sigma_{22}}{\sigma_{11}} \quad \text{and} \quad \rho_3 = \frac{\sigma_{33}}{\sigma_{11}}, \tag{4.6}$$

where ρ_2 and ρ_3 are constants. Three-dimensional loading states are characterised by two parameters, the triaxiality and the Lode parameter. The stress triaxiality relates to the given stress ratios as

$$T = \frac{1+\rho_2+\rho_3}{\sqrt{(1-\rho_2)^2+(\rho_2-\rho_3)^2+(\rho_3-1)^2}}, \tag{4.7}$$

and the Lode parameter is given by

$$L = \frac{2\rho_2 - 1 - \rho_3}{1-\rho_3}. \tag{4.8}$$

The Lode parameter values $L = -1$ ($\sigma_{11} > \sigma_{22} = \sigma_{33}$) and $L = 1$ ($\sigma_{11} = \sigma_{22} > \sigma_{33}$) correspond to overall axi-symmetric stress states, while $L = 0$ ($\sigma_{11} > \sigma_{22} > \sigma_{33}$) corresponds to an overall state of shear and hydrostatic stress. The stress components vary throughout deformation, but the stress ratios, ρ_2 and ρ_3, are maintained in each increment according to Eq. (4.6). This is achieved for the 3D model by creating multiple point constraints (MPCs), allowing for the connection of different nodes and degrees of freedom in the model. In ABAQUS, this is done through the user subroutine MPC. To allow for a prescribed stress state while imposing boundary conditions on all sides of the unit cell, extra degrees of freedom are needed. The extra degrees of freedom are introduced through three dummy nodes placed outside the mesh. The dummy nodes are referred to as N_i ($i = 1, 2, 3$). They are connected to a master node, M, integrated with the mesh through spring elements (SPRING2 in the ABAQUS element library). This is shown in Fig. 4.3. A prescribed displacement in the main loading direction (x_1) is applied to a dummy node, N_1. The MPC subroutine is called for each user-subroutine-defined multi-point constraint in the ABAQUS input file. The displacements of the dummy nodes N_2

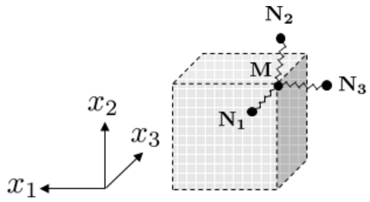

Figure 4.3. The spring elements for the multiple point constraints connected to one connector node M.

and N_3 corresponding to the desired stress triaxiality and Lode parameter values are calculated in the MPC subroutine. The displacement of the dummy nodes is related to the forces, F_i at the face of the unit cell through

$$F_i = k_i(u_i^{N_i} - u_i^M), \quad i = 1, 2, 3, \tag{4.9}$$

where k_i is the spring element constant, given as a function of the unit cell face areas, A_i. The forces across the unit cell faces, F_i, relate to the macroscopic stresses through

$$\sigma_{11} = \frac{F_1}{A_1}, \quad \sigma_{22} = \frac{F_2}{A_2}, \quad \sigma_{33} = \frac{F_3}{A_3}, \tag{4.10}$$

where A_i is the area over which the forces act, i.e., the faces of the unit cell. Combining Eqs. (4.6), (4.9) and (4.10) and solving for $u_i^{N_i}$ gives the displacement of dummy node N_i in the direction of x_i, which, with constant ρ_2 and ρ_3 values for the x_2- and x_3-direction, respectively, read

$$\begin{aligned} u_2^{N_2} &= u_2^M + \rho_2 \frac{A_2}{A_1}\frac{k_1}{k_2}\left(u_1^{N_1} - u_1^M\right) \\ u_3^{N_3} &= u_3^M + \rho_3 \frac{A_3}{A_1}\frac{k_1}{k_3}\left(u_1^{N_1} - u_1^M\right), \end{aligned} \tag{4.11}$$

where ρ_2 and ρ_3 are input values. It is seen that both the areas and the spring element cancel out for a perfect cubic geometry as $k_i = k_i(A_i)$. When u_2 and u_3 have been applied to the dummy nodes N_2 and N_3, linear constraint equations are used to apply the displacement of the dummy nodes, N_1, N_2 and N_3, to the entire unit cell. A linear constraint requires that a linear combination of nodal variables is equal to zero and can be used to constrain degrees of freedom. The displacement of the master node in the mesh, which is given based on the displacements of the dummy nodes, is coupled to the displacement of all nodes at the unit cell's outward faces, i.e., the ones without symmetry conditions, in the direction of their respective face normals. In this manner, displacements consistent with the prescribed stress ratios will be applied to the entire unit cell.

For further investigation of combined effects of randomness in void distribution and size effects under different three-dimensional loading conditions, representative volume elements (RVEs) with random distributions of voids have been generated, shown in Fig. 4.4a. The voids are embedded in a matrix with user-defined elements with strain gradient plasticity theory incorporated in their definition through a UEL subroutine (see [64]). The mesh consists of element corresponding to the general-purpose ten-node tetrahedral element with four integration points (C3D10) in the ABAQUS element library. The RVEs have four voids, and symmetry cannot be exploited to model just a part of the volume.

A prescribed three-dimensional stress state is applied for each increment of simulation. Multiple point constraints (MPCs) are used, written in the subroutine MPC in ABAQUS, in a way

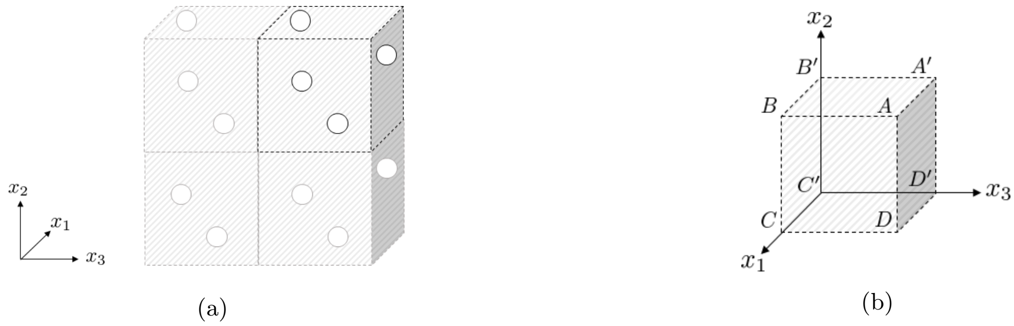

Figure 4.4. (a) Representative volume element (RVE) of a material with randomly distributed voids. (b) Faces, sides and vertices of the representative volume element.

analogous to those of the symmetric 1/8 unit cell. Displacement is applied to a dummy node, N_1, outside the mesh. For these simulations, three master nodes in the mesh are used. The displacements for the dummy nodes N_2 and N_3 corresponding to a given triaxiality and Lode parameter value, given through the stress ratios ρ_2 and ρ_3, are calculated in the MPC subroutine through Eq. 4.11, where the master nodes now are numbered as M_1, M_2 and M_3. Linear constraint equations are used to constrain degrees of freedom to ensure that the displacement of the dummy nodes is linked to the entire unit cell. This is done through periodic boundary conditions (PBCs). The PBCs require that the unit cell have a shape that will tile perfectly into a three-dimensional pattern, such as a cube. An RVE is assumed to be the smallest volume that can be simulated to give results representative of the whole. The RVE is simulated as periodic, which ensures that the unit cell approximates a continuum with a random distribution of voids. The linear constraint equations are given in Eq. 4.12, where u_i is the displacement in the ith direction ($i = 1, 2, 3$) of the nodes at the faces, edges and vertices of the unit cell as implied in Fig. 4.4b. The nodes at the corners B', C and D' are the master nodes. The combination of multiple point constraints and linear constraint equations ensures that the unit cell is periodic while maintaining a given loading state for each increment of the simulation. A limitation to the current set-up is that the voids cannot cross the unit cell boundary, and there will exist horizontal and vertical bands without voids in the material. This can be solved with an updated method of applying PBCs, which has not been done for the current work.

$$
\begin{aligned}
&\text{Faces:} && \text{Edges:} \\
&\quad u_i^{ABCD} = u_i^{A'B'C'D'} + u_i^{C} && \quad u_i^{AB} = u_i^{D'C'} + u_i^{C} + u_i^{B'} \\
&\quad u_i^{A'ABB'} = u_i^{D'DC'C} + u_i^{B'} && \quad u_i^{AD} = u_i^{B'C'} + u_i^{C} + u_i^{D'} \\
&\quad u_i^{A'BDD'} = u_i^{BB'CC'} + u_i^{D'} && \quad u_i^{AA'} = u_i^{CC'} + u_i^{B'} + u_i^{D'} \\
&\text{Vertices:} && \\
&\quad u_i^{A'} = u_i^{D'} + u_i^{B'} && \\
&\quad u_i^{D} = u_i^{C} + u_i^{D'} && \\
&\quad u_i^{B} = u_i^{C} + u_i^{B'} && \\
&\quad u_i^{A} = u_i^{C} + u_i^{B'} + u_i^{D'} && \quad i = 1, 2, 3
\end{aligned}
\tag{4.12}
$$

5. Summary of results and discussion

This chapter summarises the work carried out over the three years of the Ph.D. Section 5.1 presents work done to investigate how a continuum scale damage model's resolution level can be enhanced to incorporate length scale effects. A parametric study of the enriched Gurson-Tvergaard model has been performed for different loading conditions. The results are presented in terms of response curves and damage development. As a benchmark, corresponding results from numerical analyses of an axi-symmetric unit cell with a discrete void embedded in a material matrix obeying a strain gradient plasticity theory have been performed. The shape evolution for the discrete void is presented and used as a supplement for the discussion.

Section 5.2 summarises the main results from the numerical study of the combined effects of inter-void ligament size and size effects in three dimensional voided unit cells subject to a range of three-dimensional loading conditions. The results are presented in terms of a critical equivalent localisation stress and gradient enhanced equivalent plastic strain contours.

5.1 Gradient enriched Gurson-Tvergaard model

For porous, ductile media, the voids and their evolution, in terms of size and shape, affect material behaviour. In gradient hardening materials, a small void will generate large gradients, and the void evolution will not be captured by classic plasticity theories, as discussed in Section 2.2. Niordson and Tvergaard [1] investigated how size-effects would affect the yield surface of porous metals based on cell model analyses of axi-symmetric loading states. For a conventional material, the yield surface may be expressed by the following general form of a yield function

$$\Phi = \Phi\left(\sigma_e, \sigma_y, f, \sigma_m\right), \tag{5.1}$$

where σ_e is the equivalent Mises stress, f is the void volume fraction, σ_m is the mean stress given by $\sigma_m = (\sigma_1 + 2\sigma_2)/3$ for an axi-symmetric loading state with σ_1 as the principal stress along the main loading axis, and σ_y is the current material yield strength. Niordson and Tvergaard [1] proposed that conventional yield surfaces for porous metals can be extended to account for size-effects by modelling a conventional yield surface with a smaller void volume fraction and a decreased mean stress sensitivity. Two parameters, Q_1 and Q_2, both related to a length scale parameter, were realised. The results showed that the yield surface for a size-dependent material might be modelled by that of a conventional material following the simple transformation

$$\Phi = \Phi\left(\sigma_e, \sigma_y, Q_1 f, Q_2 \sigma_m\right), \tag{5.2}$$

where the numerically determined values of Q_1 and Q_2 fit curves with expressions given in Eq. (3.21) and Eq. (3.22). The transformation method could be applied to a previously known yield surface for a conventional material, such as the Gurson-Tvergaard model (GT), presented in Section 3.3, which is a yield surface following Eq. (5.1). The transformation according to Eq. (5.2), will introduce size effects in the constitutive equations to remedy the issue of resolution level of the GT model. Introducing size effects to the model, as such, will allow for accounting for micron-scale effects in a macro-scale simulation. The constitutive equations of the enriched GT model are given in Section 3.3.1 and have been implemented for a one-point model according to Section 4.1. The new parameters, Q_1 and Q_2, are introduced as prefactors to the void volume fraction and mean stress, respectively, in the yield function.

The solutions based on the gradient enriched GT model are compared to corresponding predictions from a unit cell model with discrete voids embedded in a gradient enriched matrix material of the Fleck and Willis type [58]. Details of the strain gradient plasticity model can be found in Section 3.5 and its implementation in Section 4.2. The model assumes initially spherical voids periodically arranged in cylinders, shown in Fig. 5.1a, where the voids are placed in equally spaced planes according to Fig. 5.1b. Due to symmetry, only half a cell is modelled, with the cylinder approximated by an axi-symmetric unit cell, as shown in Fig. 5.1c. The initial void plane distance is $2H_c$, the initial in-plane void distance is $2R_c$, and the initial void radius is denoted r_0. The initial void volume fraction is thereby given as

$$f_0 = \frac{2r_0^2}{3R_c^2 H_C}. \tag{5.3}$$

The voids are modelled as initially spherical but change shape upon loading. The shape is characterised as the aspect ratio of the current vertical void radius and horizontal void radius, given by W. If $W = 1$, the void is spherical. For $W > 1$, the void is prolate, and $W < 1$ corresponds to an oblate void. The aspect ratio of the void for each increment is given by

$$W = \frac{r_0 + \Delta_A}{r_0 + \Delta_B}, \tag{5.4}$$

where Δ_A is the displacement of the node at the boundary between the discrete void and the matrix aligned with the x_1-axis in the axial direction. Correspondingly, Δ_B is the displacement in the transverse direction of the node at the boundary between the discrete void and the matrix aligned with x_2-axis.

The following parameters are used for all analyses: $\sigma_0/E = 0.005$, $\nu = 0.3$, $f_0 = 0.0104$ and $m = 0.01$, where σ_0 is the yield stress, E is Young's modulus, ν is the Poisson ratio and f_0 is the initial void volume fraction. The strain-rate sensitivity parameter is given as m and enters the constitutive equations for the cell model only. Care has been taken that the visco-plastic effects are minimal and that the results from the gradient enriched Gurson-Tvergaard model and the unit cell can be compared directly. See [65] for details on the value of m and the rate-independent limit. The dissipative length scale parameter, L_D, that enters the gradient enriched Gurson-Tvergaard model through the prefactors Q_1 and Q_2 for the one-point model,

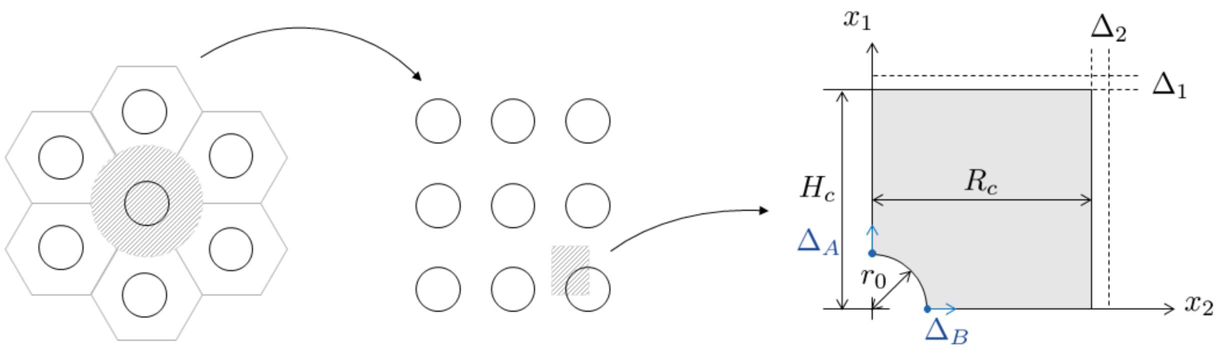

(a) (b) (c)

Figure 5.1. (a) Hexagonal distribution of voids approximated by cylinders. (b) Layers of voids where each column corresponds to a cylinder. (c) Symmetry giving an axi-symmetric unit cell approximation.

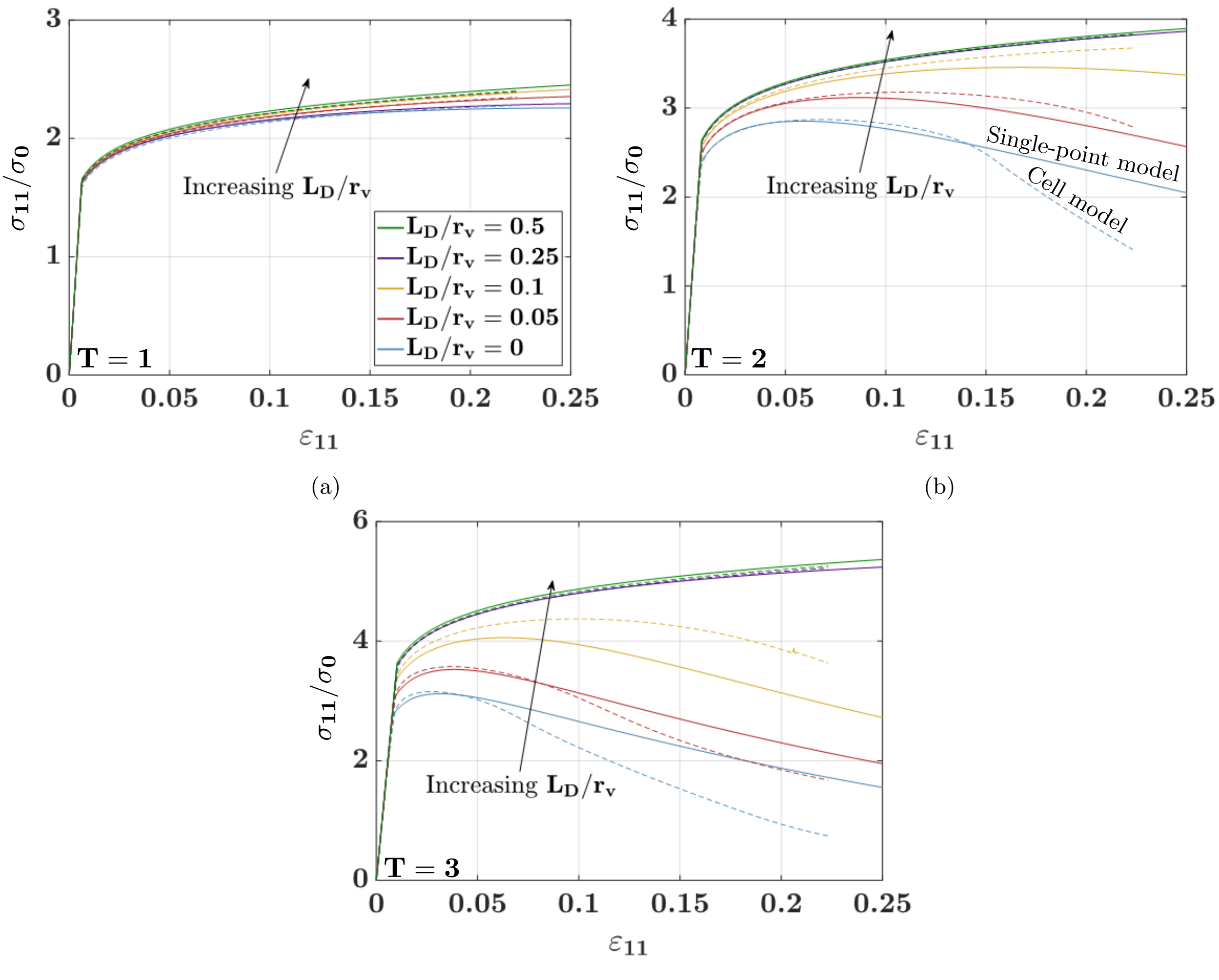

(a) (b) (c)

Figure 5.2. Response curves predictions for a conventional material and four gradient strengthening materials with $L_D/r_v = 0.05, 0.1, 0.25$ and 0.5 from the enriched GT model (solid lines) and the cell model (dashed lines) for $f_0 = 0.0104$ and $N = 0.1$. The loading conditions give (a) $T = 1$, (b) $T = 2$ and (c) $T = 3$. The logarithmic strain is given as $\varepsilon_{11} = \ln(1 + e_{11})$, where e_{11} is the engineering strain.

is normalised with the current void radius, r_v, following Eq. (3.23), and is updated with every increment. For the unit cell model, the dissipative length scale parameter enters the numerical simulations according to Section 3.5, and has been normalised with the initial void radius, r_0 in Fig. 5.1c, for all increments.

Several values of triaxiality have been applied in the numerical analysis of four different gradient strengthening materials. A conventional material with $L_D/r_v = 0$ has also been modelled and is considered the benchmark for the discussion. Three values of triaxiality are considered: $T = 1, 2$ and 3, enforced by prescribing a stress ratio, ρ in Eq. (4.1), giving the desired triaxiality through Eq. (4.2). The gradient strengthening materials have dissipative length scale parameters of $L_D/r_v = 0.05, 0.1, 0.25$ and 0.5. The strain hardening exponent has been set to $N = 0.1$. Results for different triaxiality in conjunction with size effects are presented in Fig. 5.2, where response curves in terms of axial stress and strain are shown. Taking the conventional material with $L_D/r_v = 0$ as motivation, the general observation is that higher triaxiality yields lower response curves. This is because the relative stress ratio in the transverse direction, ρ, increases with increasing triaxiality. Plastic flow will localise more easily towards coalescence with higher relative stresses in the transverse direction, associated with a higher triaxiality, lowering the load-carrying capacity of the material. Localisation is considered the basis for rapid void growth leading to material softening. This is confirmed by the conventional material results in Fig. 5.2, where the response curves are seen to exhibit increased softening due to damage growth for higher values of triaxiality. Void evolution plots can be found in Appendix B, confirming the accelerated void growth. Corresponding void shape evolution plots from the discrete void in the unit cell model are presented in Fig. 5.3, where W is shown as function of axial strain. Taking the conventional material as an example again, the void shape curve shows that the initially spherical void grows towards an increasingly oblate shape with increasing triaxiality values. The oblate shape will motivate rapid void evolution, giving considerable material softening and, ultimately, coalescence, corresponding to a rapid loss of load-carrying capacity of the material. This is seen in the response curves from the unit cell model in Fig. 5.2 for $T = 2$ and 3. The Gurson-Tvergaard model for the conventional material, $L_D/r_v = 0$, does not capture the rapid loss of load-carrying capacity associated with oblate void growth as it does not incorporate the void shape in the constitutive equation. All damage is taken to be a result of the evolution of a spherical void. The response curves from the Gurson-Tvergaard model will therefore follow the ones from the unit cell model only until severe void shape changes affect the material response.

The effect of gradient strengthening is seen to be more prominent with increasing triaxiality in Fig. 5.2. For the lowest triaxiality, $T = 1$, the effect of the length scale is limited. At the stress state giving $T = 1$, the relative stresses in the transverse direction are insufficient for localisation to develop in the inter-void ligaments for the state of deformation considered. This is reflected in the rising response curves for all values of L_D/r_v at $T = 1$. The corresponding void shape evolution predicted by the cell model in Fig. 5.3a shows that for $T = 1$, the voids are merely stretched along the main straining axis, and the shape of the voids turns prolate. The gradient enriched GT model is seen to capture the effect of elevated yield point for all values of L_D/r_v in Fig. 5.2a. The curves from the two models follow each other as no localisation or dramatic void shape changes occur at this low value of triaxiality.

For the intermediate value of triaxiality, $T = 2$, a greater effect of gradient strengthening is observed in Fig. 5.2b. The enriched GT model accurately predicts the yield point for all unit cell simulations with different L_D/r_v-values. For the conventional material, softening is observed. The cell model results predict a rapid drop in load-carrying capacity around a logarithmic axial strain of $\varepsilon_{11} = 0.13$. The corresponding void shape evolution curve in Fig. 5.3b shows that the void will grow oblate under the given loading conditions in the absence of plastic strain gradients. A rapid escalation of void shape evolution toward coalescence is predicted at a strain corresponding to the drop in load-carrying capacity. The enriched GT model will not capture this effect as it does not incorporate the shape of the void in its constitutive equations. The response curves for the conventional material predicted from the enriched GT model is seen to deviate from that of the cell model following the rapid void change. For the materials with gradient hardening, this effect will vanish as gradients will strengthen the void ligaments and hinder plastic flow localisation. For material with small microstructures and large strain gradients, $L_D/r_v = 0.25$ and 0.5, the material does not soften for the state of deformation considered for loading conditions giving $T = 2$. The corresponding void shape curves in Fig. 5.3b show that the voids grow towards a prolate shape. The gradient strengthening in the void ligaments is strong enough to drastically delay plastic flow localisation for $L_D/r_v = 0.25$ and 0.5. The enriched GT model captures the response curves for these materials well, as the prolate void shape affects the material response to a lesser extent than oblate voids. For the intermediate length scale parameters, $L_D/r_v = 0.05$ and 0.1 a similar effect is observed. The materials soften at the state of deformation considered but at larger axial strain values compared to the conventional material. The void shape curves show that the voids grow slightly towards a prolate shape. The

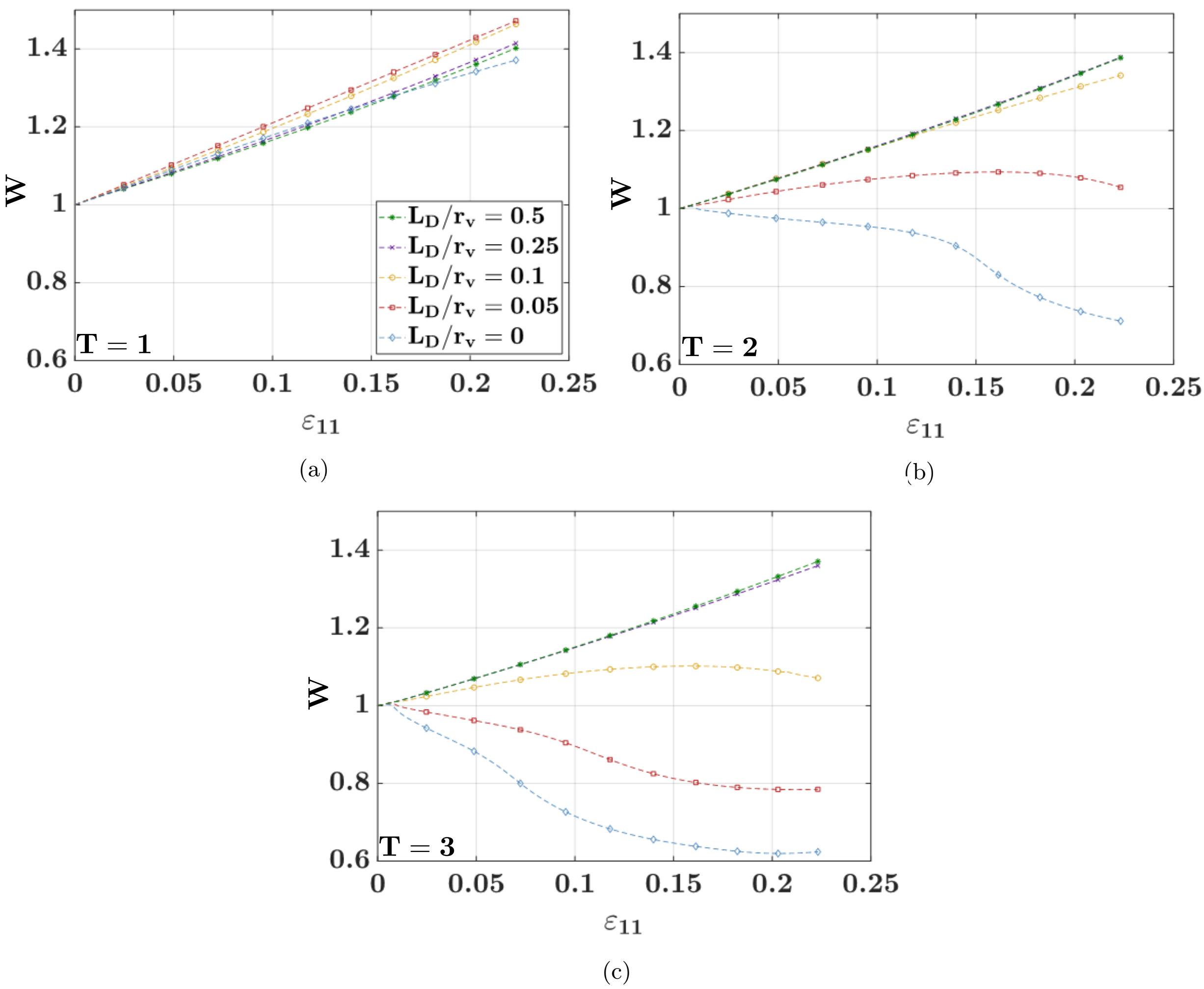

Figure 5.3. Aspect ratio evolution of the discrete void in the cell model given by Eq. 5.4 for $f_0 = 0.0104$, $n = 0.1$ and loading conditions giving (a) $T = 1$, (b) $T = 2$ and (c) $T = 3$.

material with the least gradient strengthening, $L_D/r_v = 0.05$, will grow back towards a spherical shape for higher values of axial logarithmic strain, indicating that plastic flow has started to localise in the ligaments.

The response curves and void shape evolution for the highest triaxiality, $T = 3$ are shown in Fig. 5.2c and Fig. 5.3c, respectively. The results are continuations of the trend observed for $T = 2$. At this value of triaxiality, the relative stress ratios in the transverse direction are sufficient to invoke localisation for the conventional material and the materials with little gradient strengthening, $L_D/r_v = 0.05$ and 0.1. The material loses its load-carrying capacity as plastic flow localises in the ligaments and the void shape grows towards oblate. This is again not captured by the enriched GT model. The deviation between the two models becomes obvious when comparing response curves predicted from the enriched GT model and the unit cell model for the conventional material and materials with dissipative length scale parameters of $L_D/r_v = 0.05$ and 0.1. For the same materials, the void shape evolution shows that void growth toward an oblate shape is prominent. Accounting for void shape changes toward coalescence is paramount for accurate predictions of material response at the micron-scale. For materials with a length scale parameter sufficient to inhibit plastic flow localisation, and thereby also oblate void growth towards coalescence, the enriched GT model captures the material response well.

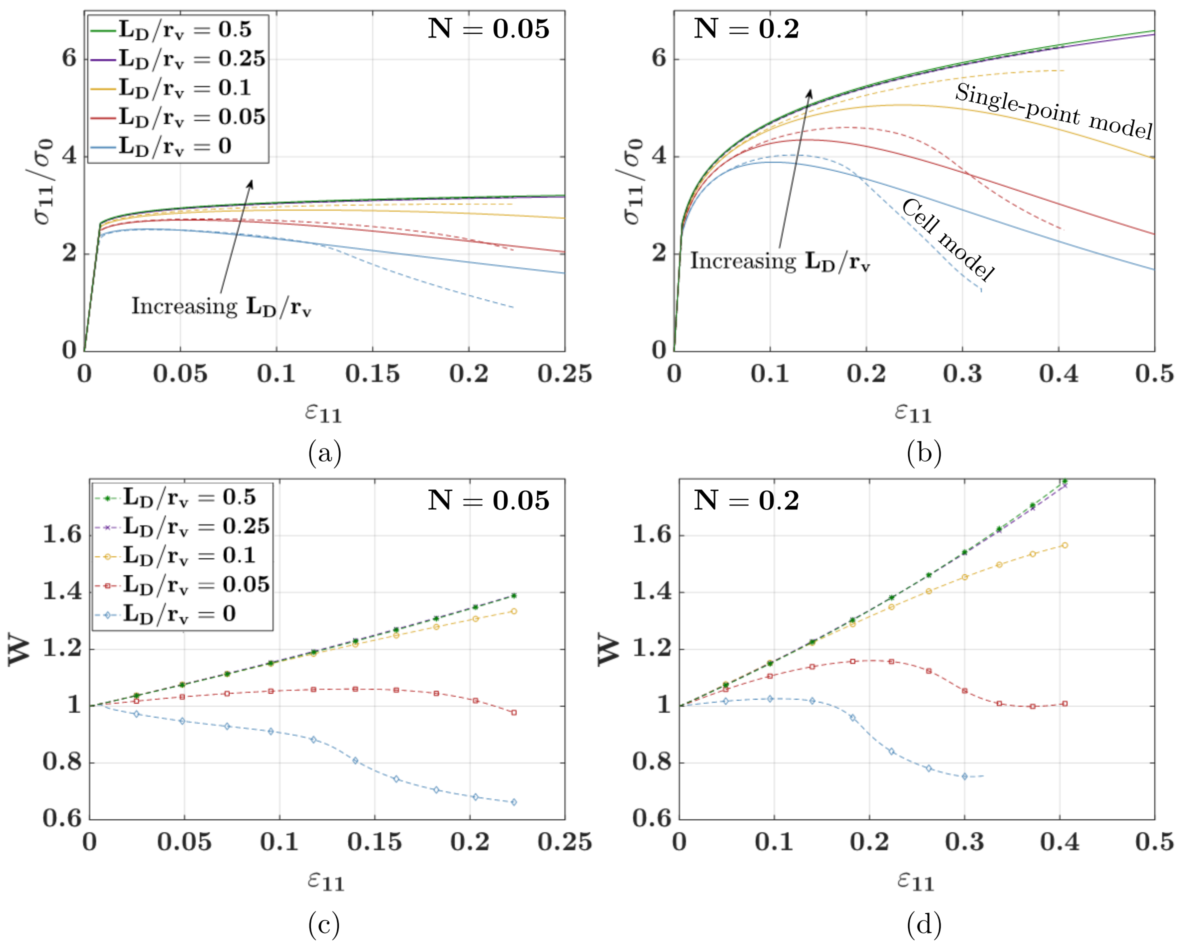

Figure 5.4. Response and void shape evolution curves for $N = 0.05$, (a) and (c), and $N = 0.2$, (b) and (d). The applied loading conditions give a triaxiality of $T = 2$ and the initial void volume fraction is $f_0 = 0.0104$.

The effect of the hardening exponent, N in Eq. (3.1), in conjunction with gradient hardening has been investigated. Three values of N have been used in numerical simulation: $N = 0.05$, 0.1 and 0.2 for the following four values of $L_D/r_v = 0.05$, 0.1, 0.25 and 0.5. Results for a conventional material is used as a reference. The triaxiality was kept constant at $T = 2$. As the strain hardening exponent influences the peak of the response curves, direct comparison between results for the different values of N is not possible. Therefore, the simulations for $N = 0.2$ are taken to twice as large axial strain compared to the other simulations. Figure 5.4 shows predicted response curves from the enriched GT model presented alongside corresponding predictions from the axi-symmetric unit cell for $n = 0.05$ and $n = 0.2$ for all values of L_D/r_v. Void shape evolution curves from the cell model are also presented in Fig. 5.4. Corresponding porosity evolution plots can be found in Appendix B. For $N = 0.1$, results are presented for $T = 2$ in Figs. 5.2b and 5.3b. Figures 5.4a and b show that the spread of the response curves with increasing length scale parameter increases with increasing hardening exponent value. This indicates the synergy effect between strain hardening and gradient strengthening as they are related through Eq. 3.50. Considering the conventional material and the smaller value of strain hardening, $N = 0.05$, the response curve is seen to soften soon after yielding. The corresponding void shape evolution curves show that the void immediately grows towards an oblate shape. The strain hardening is not sufficient to impede plastic flow localisation, and the voids grow towards coalescence. The GT model is seen to capture the softening due to void growth in the material, but not the effects of rapid void shape changes towards an oblate shape consistent with localisation. For the gradient strengthening materials with the same strain hardening exponent, $N = 0.05$, gradients build up around the voids, strengthening the material and delaying the onset of localisation. The enriched GT model is seen to capture the rising yield point of the response curves and the softening due to void growth for $L_D/r_v = 0.05$ and 0.1. For the materials with the greatest gradient strengthening, $L_D/r_v = 0.25$ and 0.5, the gradient contribution is sufficient to impede localisation. The response curves do not show softening as the voids grow prolate. The enriched Gurson-Tvergaard model captures the response of these materials well localisation has not occurred.

For the materials with a larger strain gradient exponent, $N = 0.2$, the response curve for the conventional material predicted by the cell model is seen to exhibit a different course of curve than for lower values of N. Strong strain hardening gives a rapidly rising response curve after yielding before a peak is reached, after which a rapid loss of load-carrying capacity occurs. The initial rise of the response curves indicates that the conventional material hardens sufficiently to delay excessive void growth in the transverse direction. This is confirmed in the void shape evolution plot, Fig. 5.4d, where the voids are observed to grow prolate for small values of axial strain for the conventional material. In a material with a large hardening exponent, high stresses are required to maintain plastic flow after yielding. Localisation will therefore be dramatic when it occurs, followed by abrupt softening of the material. The high stresses in the material will drive the void growth rapidly, and localisation will ensure that the voids grow oblate. This is confirmed in Fig. 5.4d, where a dramatic change of void shape is seen to occur around an axial strain value of $\varepsilon_{11} = 0.15$ for the conventional material.

The material with the lowest dissipative length scale parameter, $L_D/r_v = 0.05$, and $N = 0.2$, exhibits the same behaviour as the conventional material, slightly delayed due to strengthening from the plastic strain gradients. Increased length scale parameter corresponds to a more considerable plastic strain gradient contribution and gradient strengthening. For the materials with a large dissipative length scale parameter, $L_D/r_v = 0.25$ and 0.5, the plastic strain gradients are sufficiently large to inhibit localisation for the state of deformation considered. The response curves do not show softening, and the void shape curves show that the voids grow towards a prolate shape. The enriched GT model captures the effects of an increasingly rising response curve with increased strain hardening, but the material softening is dependent only on the void volume fraction, f. The dramatic effect of void shape evolution and coalescence is not captured, and response curves predicted by the enriched GT model deviate from those of the cell model for the material with insufficient gradient strengthening to impede localisation. It is clear that representing the effect of the evolution of micronscale voids through a single parameter, namely the void volume fraction, f, is not sufficient to capture these combined effects, and the enriched GT model will therefore not accurately represent the response of the material.

In summary, the enriched GT model captures the dissipative strengthening arising from gradients in the plastic strain rate field with diminishing microstructure for all configurations of loading state and strain hardening investigated. In [P1], the effect of the initial void volume fraction, f_0, is also investigated. The results are omitted, but can be found in the appended publication, [P1]. It seems reasonable to assume that void shape evolution plays a prominent role in material response and influences the load-carrying capacity of the material to such an extent that the void volume fraction itself is not a sufficient measure for damage evolution. However, the enriched GT model, being a damage model, accounts for the damage from void evolution solely through f and will not capture the effects of void shape, which are obvious given that the significant drops in the load-carrying capacity for the different materials are found to occur at the same level of axial logarithmic strain as significant void shape changes towards an oblate shape. Higher triaxiality will, given the high relative stress component, ρ, allow the voids to grow in the transverse direction and turn oblate, and localisation in the inter-void ligaments will more readily occur than plasticity in the entire material volume. This is indicative of inter-void ligament size as well as void shape being of importance for material performance. Two natural continuations of this work therefore follow. One is the implementation of a gradient enriched Gologanu-Leblond-Devaux model that accounts for void shape and porosity in the yield criterion. The ongoing work treating this is presented in Section 6.1. The other is to perform a parametric study of inter-void ligament size for a single void population, as done in [P2]. The results of this work is summarised in Section 5.2.

5.2 Combined effects of inter-void ligament size and void size

To understand the interaction of the inter-void ligament size and material size effect on localisation for a range of imposed stress states, three-dimensional unit cell analyses were carried out. The unit cells form a periodic array of initially spherical voids with initial radius r_0, as seen in Fig. 5.5. The unit cell has edge lengths $2a_i^0$ along the three coordinate axes, $x_i (i = 1, 2, 3)$, and inter-void spacings equal $2l_i^0 = 2a_i^0 - 2r_0$. Only 1/8 of the unit cell needs to be modelled due to symmetry about the three planes perpendicular to the coordinate axes. The initial void volume fraction is given by $f_0 = (4/3\pi r_0^3)/(8a_1^0 a_2^0 a_3^0)$ is kept constant for all unit cells considered. To achieve various initial inter-void ligament spacings, while the initial void volume fraction is kept constant through a constant initial void radius, r_0, the unit cell dimensions are varied. The geometric parameters for the different unit cells are given in Table 5.1, where it can be seen that the l_3-ligament is the smallest ligament for all configurations except one, which is a perfect cube.

The discrete voids were embedded in a material matrix obeying the strain gradient plasticity theory of Gudmundson [55], cast in the mathematical context of Fleck and Willis [58]. The theory was implemented in a user-defined element subroutine (UEL) in ABAQUS following Section 4.3. Finite element meshes for four unit cell configurations are shown in Fig. 5.6. The imposed stress states are characterised by fixed values of stress triaxiality and Lode parameter given by Eqs. (4.7) and (4.8), respectively, imposed through a multiple point constraint subroutine (MPC) in ABAQUS, described in Section 4.3. A small strain formulation is used, and the modelling setup does therefore not account for softening due to void evolution. The critical stress at which a given configuration of loading conditions and geometry loses load-carrying capacity is determined through a limit load-type analysis. A limit load analysis is designed to determine the overall yield criterion for a given configuration, and the materials analysed are therefore idealised as

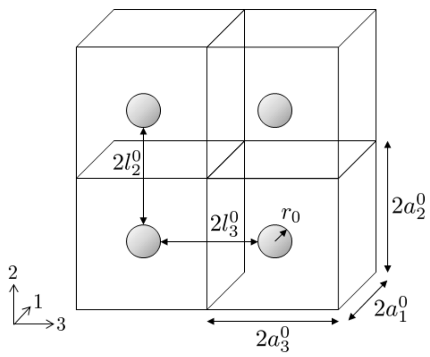

Figure 5.5. Schematic showing the periodic arrangement of voids in the x_2- and x_3-plane. The distribution along the x_1-direction is not shown for simplicity.

Table 5.1. Geometric parameters for the various unit cells considered for $f_0 = 0.01$.

$a_1^0/r_0 = a_2^0/r_0$	a_3^0/r_0	$l_1^0/r_0 = l_2^0/r_0$	l_3^0/r_0
6.06	1.43	5.05	0.43
5.55	1.70	4.55	0.70
5.21	1.94	4.21	0.95
4.97	2.12	3.97	1.12
4.58	2.50	3.58	1.50
4.18	3.00	3.18	2.00
3.75	3.75	2.75	2.75

perfectly plastic. The strain hardening exponent, N, is set to zero as is the energetic length scale parameter, L_E. Energetic gradient contributions strain harden the material and are therefore omitted. Consequently, the corresponding energetic quantities given in Section 3.5 vanish.

The following parameters are used for all analyses: $\sigma_0/E = 0.001$, $\nu = 0.3$ and $m = 0.01$, where σ_0 is the yield stress, E is Young's modulus, and ν is the Poisson ratio and m the strain rate sensitivity exponent. The value of m has been chosen to approximate a rate-independent material response, see [65] for details. The initial void volume fraction is $f_0 = 0.01$. The influence of imposed stress state, illustrated by the stress triaxiality, T, and the Lode parameter, L, is studied along with the influence of the normalised dissipative length scale parameter, L_D/r_0.

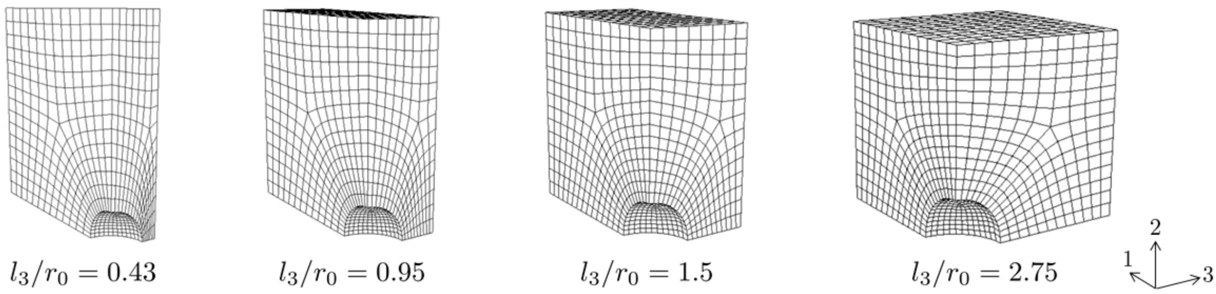

Figure 5.6. Finite element meshes showing 1/8 of the unit cell with an initially spherical void of radius r_0 in the centre giving an initial void volume fraction of $f_0 = 0.01$.

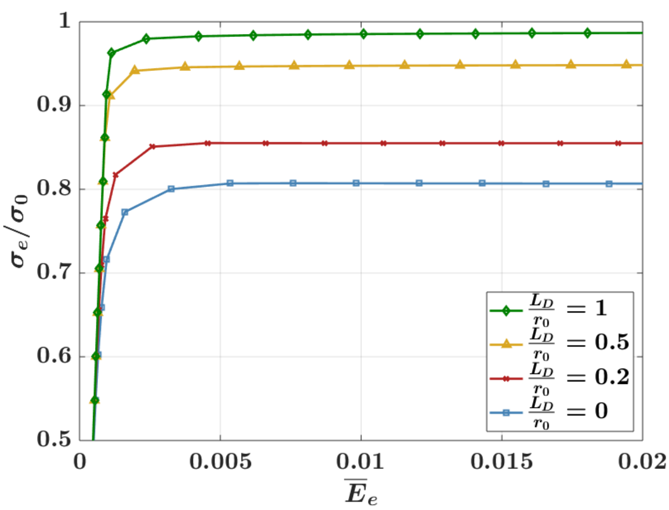

Figure 5.7. Equivalent stress-strain curves for an inter-void ligament size of $l_3/r_0 = 1.5$ under loading conditions giving Lode parameter $L = -1$ and triaxiality $T = 3$.

The dissipative length scale parameter is normalised with the initial void radius, r_0, and kept constant throughout the deformation history. For all imposed stress states, the relative stress component in the l_3-ligament, the ligament along the x_3-axis in Fig. 5.5, will be smallest as ρ_3 in Eq. (4.6) is always the smallest stress ratio.

The critical equivalent stress determines the load-carrying capacity of the material. Figure 5.7 shows examples of equivalent stress-strain curves. Here, for a geometry giving $l_3/r_0 = 1.5$ under loading conditions giving a triaxiality of $T = 3$ and a Lode parameter of $L = -1$. Results for three values of normalised dissipative length scale parameter are presented, $L_D/r_0 = 0.2, 0.5$ and 1 along with results for a conventional material with $L_D/r_0 = 0$. The overall equivalent stress, σ_e, is given by

$$\sigma_e = \frac{1}{\sqrt{2}}\sqrt{(\Sigma_{11}-\Sigma_{22})^2 + (\Sigma_{22}-\Sigma_{33})^2(\Sigma_{33}-\Sigma_{11})^2}, \tag{5.5}$$

where the overall stress components σ_{ij} are given by $\Sigma_{ij} = \int_V \sigma_{ij}\mathrm{d}V/V$, where V is the volume of the unit cell, including the volume of the void. The overall equivalent strain, $\overline{E}_e$, is given by

$$\overline{E}_e = \frac{\sqrt{2}}{3}\sqrt{(E_{11}-E_{22})^2 + (E_{22}-E_{33})^2 + (E_{33}-E_{11})^2}, \tag{5.6}$$

where the strain components E_{ij} are found in a way analogous to the stress components. The material response in Fig. 5.7 shows a clear size effect. The larger the length scale parameter and, i.e., the smaller the microstructure, the higher the equivalent stress level. Increased strain gradient strengthening with down-scaling of the microstructure will delay material yielding. The critical equivalent stress, σ_e^c/σ_0, which is considered the onset localisation, is taken at the plateau of the equivalent stress-strain curve.

Several values of both triaxiality, T, and Lode parameter, L, have been applied to the different unit cell geometries. Their effect in combination with the inter-void ligament size on material response is discussed for the conventional material. This is considered to lay the foundation for the discussion of material size effects. Three values of Lode parameter are considered: $L = -1, 0$ and 1. Recall that the outer bound values of the Lode parameter, $L = -1$ and $L = 1$, correspond to axi-symmetric stress states with $\sigma_{11} > \sigma_{22} = \sigma_{33}$ and $\sigma_{11} = \sigma_{22} > \sigma_{33}$, respectively. However, for $L = 0$, an overall state of shear and hydrostatic stress is considered, where $\sigma_{11} > \sigma_{22} > \sigma_{33}$. Results for different Lode parameters are presented in Fig. 5.8a, where the critical equivalent stress as function of inter-void ligament size is shown. The triaxiality is kept constant at $T = 3$. The critical equivalent stress is seen to increase with increasing inter-void ligament size for all Lode parameter values. The l_3-ligament can sustain higher stresses with increasing size and give higher critical equivalent stress levels as it increases. This trend cannot be extrapolated to the results for the cubic unit cell, $l_3/r_0 = 2.75$, where the critical equivalent stress level is seen to drop compared to the results for $l_3/r_0 = 1.5$. This is especially prominent for $L = 0$. This is a geometrical and loading condition-specific effect stemming from a localisation pattern shift as there is no bias towards the l_3-ligament for a cubic configuration. For the combined state of hydrostatic tension and shear for $L = 0$, the plastic flow will localise in a band stretching at $\approx 45°$ across the unit cell, rather than in the l_3-ligament. This will lead to an early loss in load-carrying capacity. Localisation will be favoured in the l_3-ligament for the elongated unit cells with $l_3/r_0 < 2.75$. A homogeneous distribution of voids, where all inter-void ligament sizes are equal, will be detrimental to material performance. The results in Fig. 5.8a indicate that there exists a range of inhomogeneity, represented by a range of l_3/r_0 in this work, over which material performance will be optimal. The results presented in Fig. 5.8a show that the critical equivalent stress decreases with increasing Lode parameter for all inter-void ligament

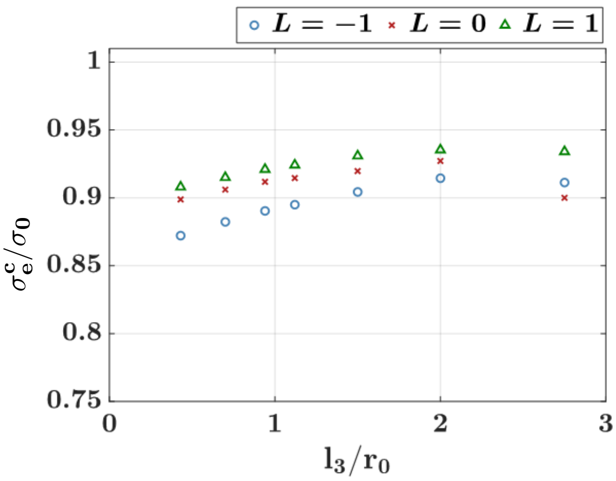

(a)

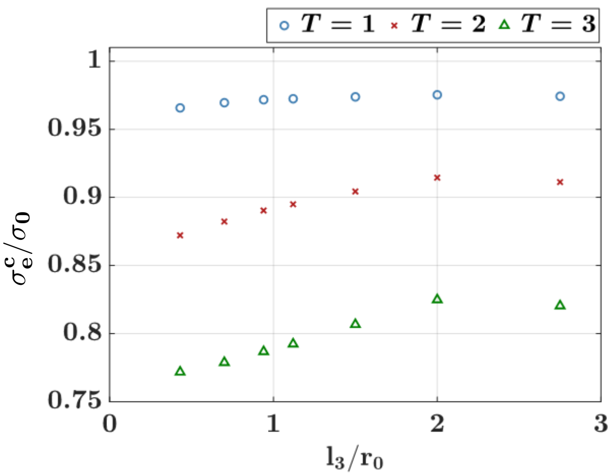

(b)

Figure 5.8. Critical equivalent stress vs. normalised ligament size for a conventional material with $L_D/r_0 = 0$ for (a) three values of the Lode parameter with $T = 2$ and(b) three values of the stress triaxiality with $L = -1$.

sizes except the cubic unit cell, $l_3/r_0 = 2.75$. The relative stress component in the x_3-direction, ρ_3, is largest for the smallest Lode parameter, $L = -1$. Therefore, localisation in the l_3-ligament is expected to initiate at lower overall deformation levels, and the critical equivalent stress will be lower. Conversely, ρ_3 is the smallest for the largest Lode parameter value, $L = 1$, resulting in delayed localisation, and this loading state will give higher critical equivalent stresses.

The effect of triaxiality has been investigated. The effect of $T = 1, 2$ and 3 is shown in Fig. 5.8b, where critical equivalent stress as function of inter-void ligament size is presented. An overall axi-symmetric stress state corresponding to $L = -1$ is prescribed. For all ligament sizes considered, a high value of stress triaxiality is seen to give lower critical equivalent stress. This is expected as the relative stress ratios, ρ_2 and ρ_3, increase with increasing stress triaxiality. The effect of inter-void ligament size is observed to be more prominent for higher triaxialities. For the lowest triaxiality, $T = 1$, the critical stress is almost independent of inter-void ligament size. The relative stress transverse to the main loading axis for this triaxiality value is insufficient to invoke localisation in the l_3-ligament for the state of deformation considered. Plasticity will instead initiate in the entire cell, called macroscopic localisation, and the results will not exhibit profound dependence on inter-void ligament size. For increasing triaxialities, the transverse stresses are sufficient to invoke localisation in the l_3-ligament, and the critical equivalent stress will therefore depend on the inter-void ligament size. For the cubic unit cell, $l_3/r_0 = 2.75$, a drop is observed in the critical equivalent stress. This is especially prominent for the highest value of triaxiality, $T = 3$. This is a consequence of the symmetric geometry and loading conditions at $L = -1$ ($\sigma_{22} = \sigma_{33}$). Bands of plastic deformation will initiate across the unit cell's faces at sufficiently large strains instead of in the l_3-ligament as this is the same size as the two other ligaments. This will ultimately lower the critical equivalent stress, which confirms that a homogeneous void distribution may be detrimental to material performance.

Gradient strengthening is introduced through the normalised length scale parameter L_D/r_0, where L_D is introduced in Section 3.5. Keep in mind that increasing L_D/r_0 corresponds to down-scaling the microstructure giving rise to higher gradients and increased gradient strengthening. Three values of the length scale parameter are used to investigate the effect of gradient strengthening on critical equivalent stress, $L_D/r_0 = 0.2, 0.5$ and 1. Results for a conventional material, $L_D/r_0 = 0$, are presented as a reference. The effect of the the normalised length scale

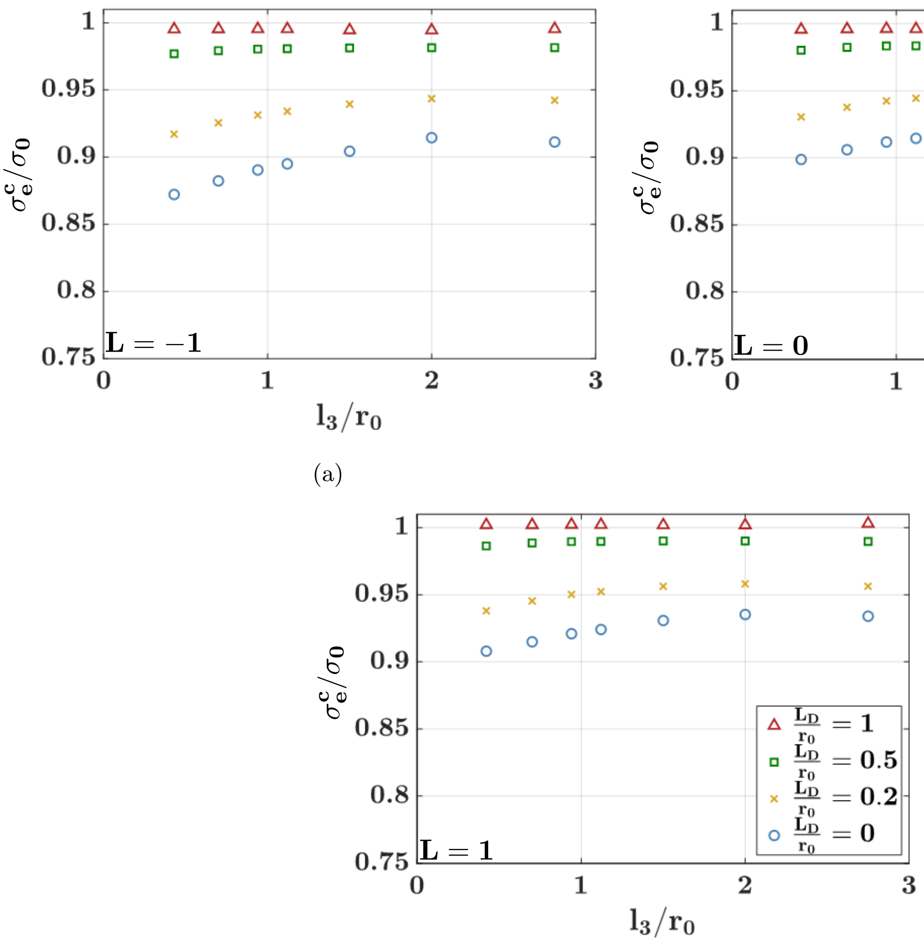

(a) (b)

(c)

Figure 5.9. Critical equivalent stress vs. normalised ligament size for a conventional material with $L_D/r_0 = 0$ and three gradient strengthening materials with $L_D/r_0 = 0.2, 0.5$ and 1 under loading conditions giving $T = 2$ for (a) $L = -1$, (b) $L = 0$ and (c) $L = 1$.

parameter, L_D/r_0, in conjunction with Lode parameter is presented in Fig 5.9 where the critical equivalent stress as function of inter-void ligament size is shown for a fixed value of triaxiality, $T = 2$. The observation is that increasing the length scale parameter strengthens the material resulting in high critical equivalent stress values. With sufficient gradient strengthening, the critical stress reaches an upper bound where the gradients dominate the material response. At these large values of length scale parameter, $L_D/r_0 = 0.5$ and 1, the strengthening is so severe that the unit cells will undergo macroscopic localisation instead of plasticity localising in the inter-void ligaments. The results become independent of the Lode parameter, inter-void ligament size for all geometries.

Similar results, the effect of the normalised length scale parameter, L_D/r_0, together with triaxiality, are presented in Fig. 5.10. The critical stress as function of inter-void ligament size is presented for a fixed value of Lode parameter, $L = 0$. The effect of the length scale parameter is seen to increase with increasing triaxiality. For $T = 1$, presented in Fig. 5.10a, limited effect of L_D/r_0 is seen. The small increase in critical equivalent stress is due to plastic strain gradients that build up around the void as its size decreases. The relative stress components in the transverse direction, ρ_2 and ρ_3, giving loading conditions corresponding to $T = 1$ are inadequate for localisation to initiate in the inter-void ligaments for the state of deformation considered.

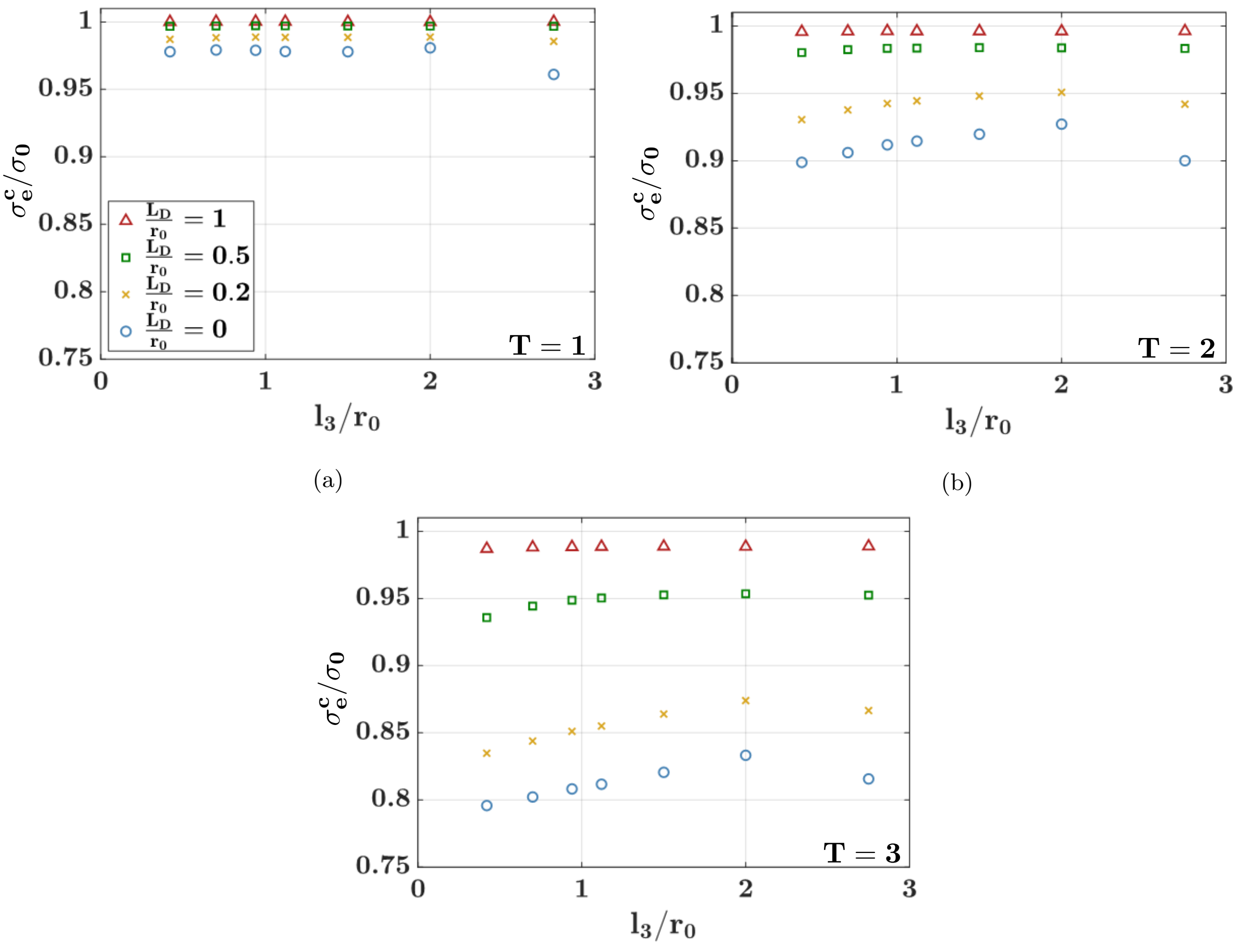

(a) (b) (c)

Figure 5.10. Critical equivalent stress vs. normalised ligament size for a conventional material with $L_D/r_0 = 0$ and three gradient strengthening materials with $L_D/r_0 = 0.2, 0.5$ and 1 under loading conditions giving $L = 0$ for (a) $T = 1$, (b) $T = 2$ and (c) $T = 3$.

The effect of the inter-void ligament will therefore be limited. Macroscopic localisation is the deformation mechanism prevailing at this low value of stress triaxiality [66]. The gradients surrounding the void will have a limited effect as deformation takes place across the unit cell. Therefore, the critical equivalent stress for $T = 1$ does not depend greatly on neither inter-void ligament size nor length scale parameter. The drop observed in critical equivalent stress observed for $l_3/r_0 = 2.75$ is due to symmetry of the unit cell and the hydrostatic and shear loading conditions, as discussed for Fig. 5.8a. The results for $T = 2$ and $T = 3$, shown in Figs. 5.10b and 5.10c, show that the effect of the length scale parameter is more prominent at these loading states, especially for the smaller inter-void ligament sizes. The relative stress ratios in the transverse direction increase as triaxiality increases and induce plastic flow localisation in the inter-void ligaments for a lower state of deformation, ultimately lowering the critical equivalent stress. The smaller ligaments can withstand less stress, and the material will lose its load-carrying capacity. The combined effect of geometry and loading condition appears with the lowered critical equivalent stress for increased triaxiality and smaller inter-void ligament size. However, plastic flow localisation gives rise to large plastic strain gradients and thereby gradient strengthening in the ligament. This will hinder further plastic flow localisation and the load-carrying capacity will increase. For a sufficiently large length scale parameter, $L_D/r_0 = 1$, the gradient strengthening will reach a threshold above which further increase in L_D/r_0 will have a negligible effect. Although not shown here, it was found that increasing the value of L_D/r_0 from 1 to 2, has a negligible effect. The effects of triaxiality and inter-void ligament size are reduced but still visible for the intermediate length scale parameter, $L_D/r_0 = 0.5$. The material with the smallest length scale parameter, $L_D/r_0 = 0.2$, follows the conventional material, just at a higher level for all inter-void ligament sizes. The gradients are sufficient to strengthen the material but not to overpower the effect of triaxiality and inter-void ligament size.

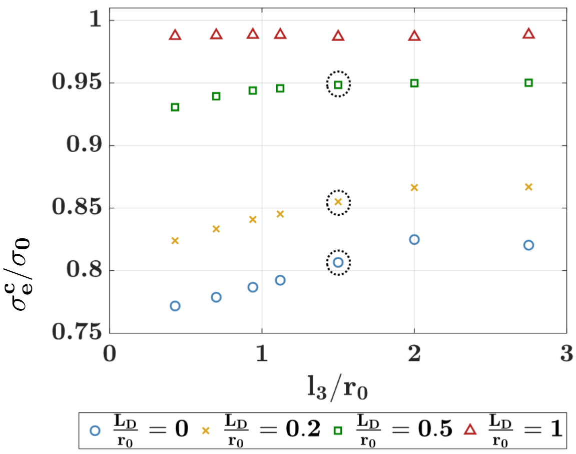

Figure 5.11. Critical equivalent stress vs. normalised ligament size for a conventional material with $L_D/r_0 = 0$ and three gradient strengthening materials with $L_D/r_0 = 0.2, 0.5$ and 1 under loading conditions giving $L = -1$ and $T = 3$.

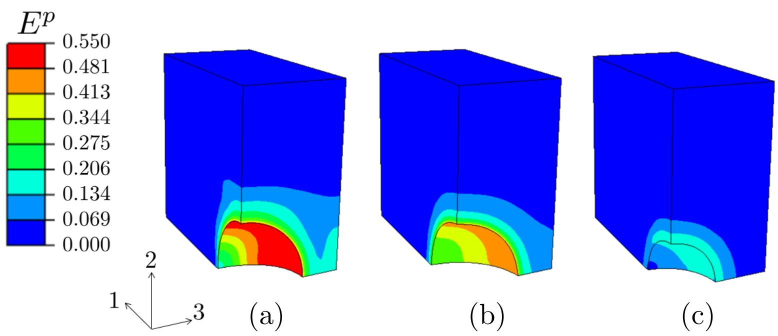

Figure 5.12. Gradient enhanced effective plastic strain, E^p, for $L = -1$, $T = 3$, $l_3/r_0 = 1.5$ for (a) the conventional material, $L_D/r_0 = 0$, (b) $L_D/r_0 = 0.2$ and (c) $L_D/r_0 = 0.5$ at an overall macroscopic effective plastic strain of $\overline{E}_e = 0.02$.

The configuration with the most pronounced effect of the length scale parameter is for loading conditions giving $L = -1$ and $T = 3$. The critical equivalent stress as function of inter-void ligament for all geometries and length scale parameters considered under those loading conditions are given in Fig. 5.11. The effect of gradient strengthening for this geometry is illustrated in Fig. 5.12, where contour plots of the gradient enhanced equivalent plastic strain, E^p in Eq. (3.50), at an overall equivalent strain of $\overline{E}_e = 0.02$ are presented for the conventional material and materials with two different length scale parameters, $L_D/r_0 = 0.2$ and $L_D/r_0 = 0.5$ for a geometry giving $l_3/r_0 = 1.5$. The corresponding critical equivalent stress values are circled in Fig. 5.11. For the conventional material, the second term in Eq. (3.50) vanishes as $L_D/r_0 = 0$. The term gradient enhanced effective plastic strain refers to the time integration of the first term of Eq. (3.50) only, which corresponds to the conventional effective plastic strain. Figure 5.12 shows a significantly lower effective plastic strain in the l_3-ligament with increasing length scale parameter. For the conventional material, plasticity is seen to have localised in the l_3-ligament. For $L_D/r_0 = 0.2$, far less plasticity is seen to develop, plasticity has barely been initiated for the material with the largest length scale parameter, L_D/r_0. The large gradients corresponding to a large L_D/r_0-value strengthen the material and inhibits plastic flow. This gives rise to the elevated critical equivalent stress with increasing length scale parameter.

Increasing the length scale parameter will inhibit plastic flow in the inter-void ligament and strengthen the material. However, a change in deformation mechanism associated with increased gradient strengthening has been observed. Taking the loading conditions giving $L = 1$ and $T = 3$ as an example, the critical equivalent stress as function of inter-void ligament given for all length scales considered in Fig. 5.13. The geometry giving $l_3/r_0 = 0.43$, the smallest inter-void ligament size, has the overall most significant increase in critical equivalent stress with gradient strengthening. The change in deformation mechanism is illustrated for this configuration of geometry and loading conditions by the contour plots in Fig. 5.13. Contours of the normalised equivalent plastic strain rate, $\dot{E}^p/\dot{\overline{E}}_e$, are shown for both the conventional material and the material with the most significant gradient strengthening, $L_D/r_0 = 1$. For the conventional material, Fig. 5.13a shows that plastic deformation has localised in the l_3-ligament and that plasticity in the matrix surrounding the void is reduced in favour of this localisation. However, for the gradient strengthening material in Fig. 5.13b, the deformation mechanism is significantly different. Plasticity is less developed, in line with gradient strengthening, and initiated in the entire unit cell. Localisation in the l_3-ligament occurs to only a minimal extent. This indicates that gradient strengthening not only delays the onset of plasticity but changes the deformation mechanism from localisation to simultaneous macroscopic flow. The material will withstand higher stresses as the plastic deformation is spread out rather than concentrated in the inter-void ligaments. A combined effect of gradient strengthening in the inter-void ligaments and change in deformation mechanism gives rise to the elevated critical equivalent stress with increased length scale parameter. At the threshold value of critical equivalent stress, the deformation mechanism has shifted entirely to macroscopic flow, and the results are independent of inter-void ligament size.

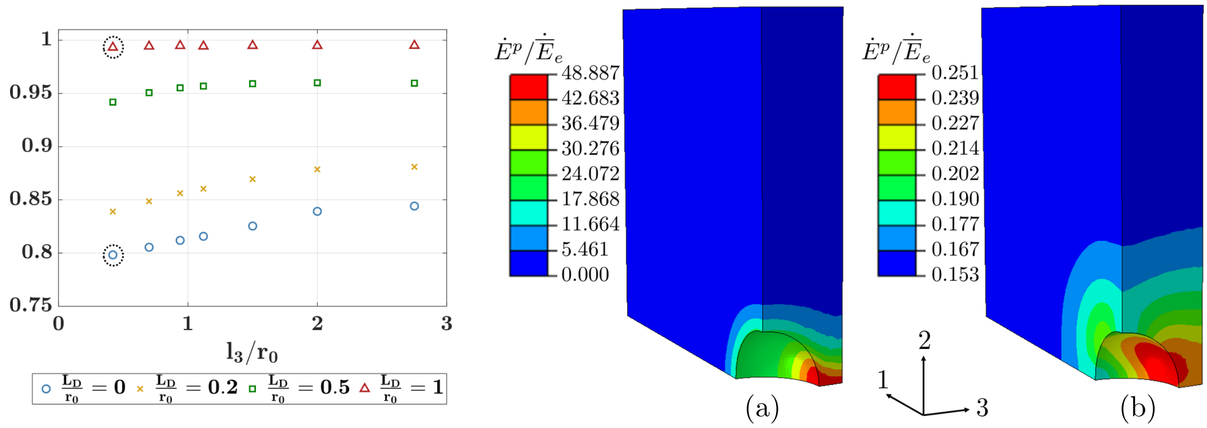

Figure 5.13. Critical equivalent stress vs. normalised ligament size and change in deformation mechanism with increased length scale parameter for $l_3/r_0 = 0.43$ with loading conditions $L = 1$ and $T = 3$ for (a) the conventional material with $L_D/r_0 = 0$ and (b) a gradient enriched material with $L_D/r_0 = 1$.

6. Ongoing work

This chapter presents two ongoing studies. The study presented in Section 6.1 is a direct continuation of the work presented in Section 5.1 and is carried out in collaboration with C.F. Niordson and K.L. Nielsen. The work has not been completed yet, but preliminary results have been obtained to allow for discussion. The second study, presented in Section 6.2, is a continuation of the work presented in Section 5.2 and is done in collaboration with E. Martìnez-Pañeda, C.F. Niordson and K.L. Nielsen. A method for studying clustering effects on material response is presented and discussed based with some preliminary results. Suggestions for further work are made.

6.1 Gradient enriched Gologanu-Leblond-Devaux model

Void shape evolution has been found to play a dominant part in the response of ductile, porous materials. To incorporate void shape effects in numerical simulations of ductile damage at the continuum scale, the Gologanu-Leblond-Devaux model has been implemented for a single-point model. The basis and constitutive equations of the model are given in Section 3.4, while the details of implementation can be found in Section 4.1. The predictions from the Gologanu-Leblond-Devaux model have been compared to corresponding predictions from a unit cell model with discrete voids of varied initial void shape embedded in a strain gradient strengthening material matrix following the theory by Gudmundson [55] on the mathematical formulation by Fleck ad Willis [63], given in Section 3.5. The implementation was done per Section 4.2. A Rayleigh-Ritz method is employed to ensure a constant value of triaxiality throughout the simulation by enforcing a prescribed stress ratio value, ρ, to be fulfilled in each increment. The voids are assumed arranged in equal distance planes in a regular hexagon pattern approximated as cylindrical, as shown in Fig. 5.1a and b. The geometry is modelled using an axi-symmetric approximation, and symmetry allows for only half a cell to be modelled. The voids are not necessarily initially spherical in this case. The shape of the discrete void is determined by the aspect ratio, W, given by the current radius in the axial direction over the current radius in the transverse direction. Different void shapes are illustrated in Fig. 6.1. Defining r_1 as the void radius in the axial direction and r_2 as the void radius in the transverse direction, the initial void volume fraction is given as

$$f_0 = \frac{2r_{20}^2 r_{10}}{3R_c^2 H_c}, \tag{6.1}$$

where r_{10} and r_{20} are the initial values of r_1 and r_2 given in Fig. 6.1. The initial void plane distance is $2H_c$, and the initial in-plane void distance is $2R_c$, shown in Fig. 5.1c. The aspect ratio for each increment given as

$$W = \frac{r_1 + \Delta_A}{r_2 + \Delta_B}, \tag{6.2}$$

where Δ_A and Δ_B are displacements of the nodes shown in Fig. 5.1c. For a spherical void, $W = 1$ as $r_1 = r_2$. For $W < 1$, the void takes an oblate shape, as showed in Fig. 6.1a, while $W > 1$ corresponds to a prolate void, given in Fig. 6.1c. Another common definition of void shape is $S = \ln(W)$, which is the parameter that enters the Gologanu-Leblond-Devaux yield

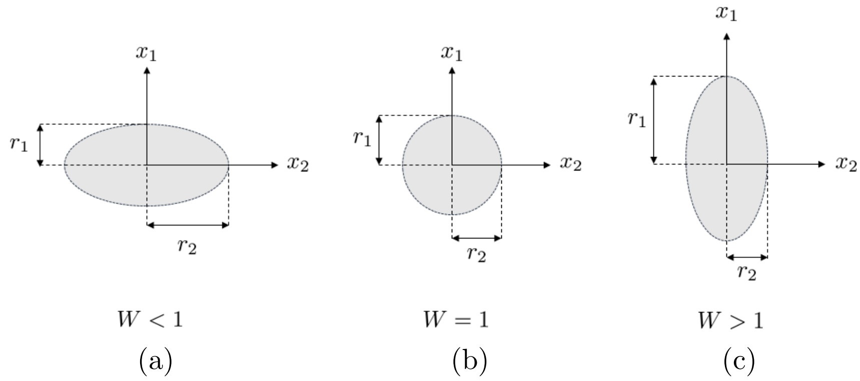

Figure 6.1. Void shapes determined by $W = r_1/r_2$ giving (a) an oblate void, (b) a spherical void and (c) a prolate void. The parameter S in the Gologanu-Leblond-Devaux model is given by $S = \ln(W)$.

surface expression given in Eq. (3.31) through the dummy parameters given in Appendix A.1. For a spherical void $S = 0$, an oblate void takes $S < 0$ and a prolate void $S > 0$.

The following parameters have been used for analysis: $\sigma_0/E = 0.002$, $\nu = 0.3$, where σ_0 is the yield stress, E is Young's modulus, and ν is the Poisson ratio. The materials are idealised as perfectly plastic in the absence of strain gradients, and the strain hardening exponent, N, is set to zero. For the cell model calculations, the strain-rate sensitivity parameters is $m = 0.01$, which is considered sufficient for the results to reasonably approximate rate-independent behaviour. The initial void volume fraction is $f = 0.04$. The investigation of size effects in porous materials with voids of different initial shapes begins with response curves showing true axial stress as function of axial strain. Response curves predicted by the unit cell model are shown in Fig. 6.2 for a conventional material without gradient strengthening under loading conditions with three different stress ratios, $\rho = 0$, 0.25 and 0.5, for three different values of initial void shape, $W_0 = 1/3$, 1 and 3. It is observed that the general effect of increasing W_0 is a heightened yield point. This is not surprising as voids are prolate when $W > 1$, and the material is able to withstand higher stresses as the inter-void ligaments are larger for prolate than for oblate voids. This is in line with the void shape effects presented in Section 5.1. Another observation is that increasing the ρ-ratio heightens the stress-strain curves for all values of W_0. The spread in the response curves for the different values of W_0 increases with ρ. This is explained by an increasing ρ giving higher relative transverse stresses, which will facilitate localisation and void growth in the transverse direction. The oblate voids, $W_0 < 1$, will be sensitive to transverses stresses to a greater extent than spherical or prolate voids, as they are already biased towards transverse growth. As such, a more significant value of transverse stresses will affect the initially oblate voids more than an initially prolate void. A prolate void, $W_0 > 1$, will have to undergo more growth in the transverse direction than an oblate void before reaching coalescence. Thus, a greater value of ρ will spread the results for the different values of W_0. The large relative stresses in the transverse direction associated with increasing ρ is also why the increased material softening observed as ρ increases, as seen in Fig. 6.2.

Axial stress-strain curves from the unit cell model for two initial void shapes, $W_0 = 1$ and 3, for a conventional material, $L_D/r_0 = 0$, and a gradient strengthening material with $L_D/r_0 = 0.6$ under loading conditions giving $\rho = 0.5$ are shown in Fig. 6.3. The yield point is delayed as the dissipative length scale increases relative to the void size, i.e., as the void size becomes smaller relative to the material length scale. The rising yield point with gradient strengthening is more prominent for the spherical than the prolate void. The spherical void is more prone to localisation of plastic flow but the gradient strengthening will shift the deformation mechanism towards macroscopic plastic flow. The void shape will play a lesser part in the deformation process as gradient strengthening increases. To quantify the delay in yield point with increasing

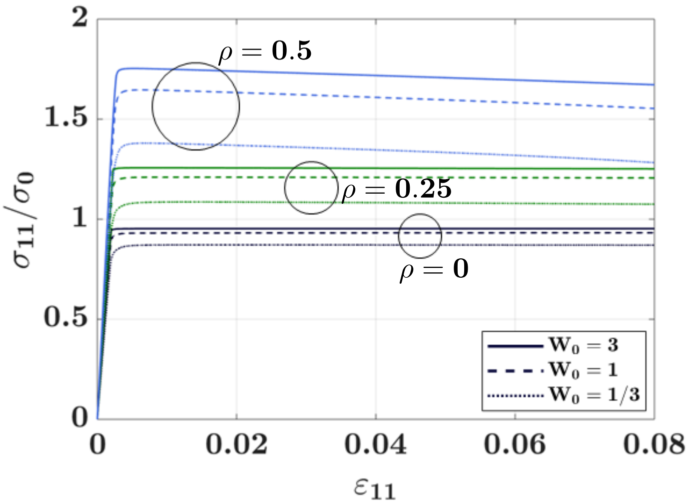

Figure 6.2. Response curves predicted by the cell model for three initial void shapes, $W_0 = 1/3$, 1 and 3 and three different stress rations, $\rho = 0$, 0.25 and 0.5.

gradient strengthening, an objective yield criterion for the cell model results must be determined. Figure 6.3 shows how the yield point has been determined for results from the unit cell model, which is taken to be at 0.02% strain. The yield point for the Gologanu-Leblond-Devaux model is taken as the first increment where β in Eq. (3.6) is 1, i.e the first increment where the yield criterion, $\Phi = 0$, is met, where Φ is given in Eq. (3.31). Yield surfaces are established in the mean stress, von Mises stress space (σ_m, σ_e). Analyses for ρ-values ranging from -0.5 to 1 gives results for the entire range of positive stress triaxialities from compression to a purely hydrostatic stress state. Yield surfaces for a conventional material with three different initial void shapes, $W_0 = 1/3$, 1 and 3, are shown in Fig. 6.4. The yield surfaces are obtained from both the cell model and the Gologanu-Leblond-Devaux (GLD) model, and a direct comparison can be made. The observation is that the oblate void, $W_0 = 1/3$, has a yield surface shifted down along the von Mises stress axis and the mean stress axis compared to the spherical void, $W_0 = 1$. The prolate void, $W_0 = 3$, has a yield surface shifted up along the von Mises stress

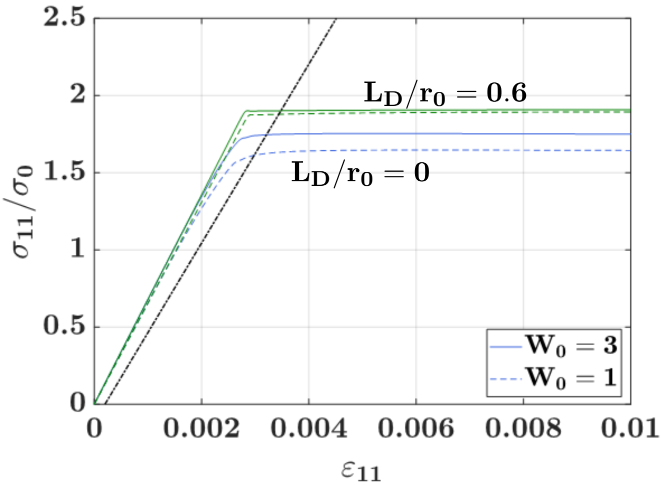

Figure 6.3. Yield point determined at 0.02% plastic strain shown for $\rho = 0.5$, $f_0 = 0.04$ for two values of initial void shape, $W_0 = 1$ and 3, for a conventional material with $L_D/r_0 = 0$ and a gradient strengthening material with $L_D/r_0 = 0.6$.

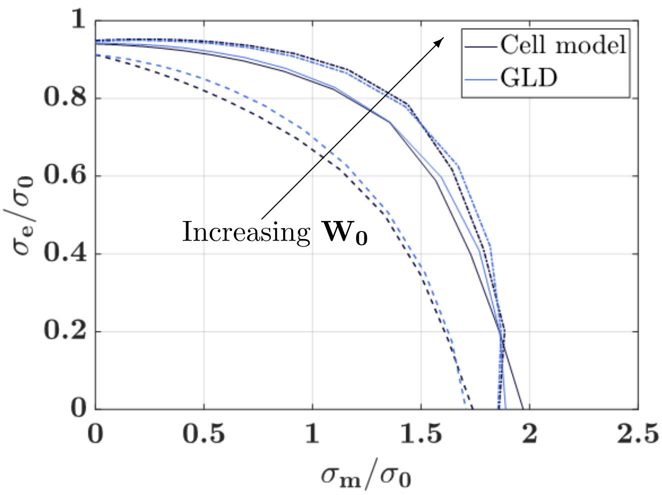

Figure 6.4. Yield surfaces predicted by the unit cell model and the Gologanu-Leblond-Devaux (GLD) model for three different initial void shapes: $W_0 = 1/3$ given by the dashed curves, $W_0 = 1$ given by the fully drawn curves, and $W_0 = 3$ given by the dotted curves.

axis but down along the mean stress axis compared to the spherical void. The yield surfaces for the spherical void, $W_0 = 1$, and the prolate void, $W_0 = 3$, cross each other for a specific value of ρ. This means that the material with prolate voids will yield at lower stresses as the loading conditions approach a hydrostatic state than the material with spherical voids. The GLD model is seen to predict the yield surfaces from the cell model accurately.

Niordson and Tvergaard [1] put forth two factors, Q_1 and Q_2, to approximate a gradient enriched yield surface utilising a yield surface for a conventional material with f and σ_m scaled by Q_1 and Q_2, respectively. The expressions for Q_1 and Q_2, given in Eqs. 3.21 and (3.22), were derived for a porous metal with damage accounted for solely through the void volume fraction. In other words, the void shape is not considered. How these factors might be used to predict size-dependent yield surfaces for a material with non-spherical voids has been explored. Yield surfaces analogous to those of Niordson and Tvergaard are used to investigate if the Q_1 and Q_2 parameters will allow the Gologanu-Leblond-Devaux framework to capture the combined effects of void size and shape. The aim is to see if a transformation corresponding to Eq. (5.2) is sufficient to predict the yield surface of a gradient strengthening material with non-spherical void growth. The Q_1-parameter for a given value of L_D/r_v has been calculated and multiplied with f in the GLD yield surface and its derivatives. The gradient enhancing Q_2-parameter is originally supposed to scale the mean stress. However, the Gologanu-Leblond-Devaux yield surface is not directly dependent on the mean stress, σ_m, but rather on generalised hydrostatic stress, σ_{gh}, given by $\sigma_{gh} = \sigma_{ij}J_{ij}$, where σ_{ij} is the Cauchy stress, and J_{ij} is given in Eq. (3.33). The tensor J_{ij} is dependent on void volume fraction and void shape through the parameter α_2, given in Eq. (A.6) for prolate voids and (A.11) for oblate voids, which is calculated from the eccentricities e_2 and e_1 given by Eqs. (A.1) and (A.2). Equation (A.1) shows that e_1 is determined from the void shape, S, while e_2 has a direct dependence on the void volume fraction, f, which makes the generalised hydrostatic stress directly depend on both f and S. The Q_2-parameter has been directly applied to the σ_{gh}-components in the GLD yield surface and its derivatives. This might be a shortcut as the Q_2-parameter was derived to scale the mean stress, σ_m, and not the generalised hydrostatic stress of the GLD model.

The Q_1 and Q_2 parameters depend on the normalised dissipative length scale parameter, L_D/r_v, given in Eq. (3.23). However, for a non-spherical void, several options for normalisation

Table 6.1. Configurations for radius dependency of Q_1 and Q_2 for the gradient enriched GLD model.

Configuration	Radius
$Q_1 = Q_1[r_{eq}]$, $Q_2 = Q_2[r_{eq}]$	$r_1 = r_{\text{axial}}$
$Q_1 = Q_1[r_1]$, $Q_2 = Q_2[r_{eq}]$	$r_2 = r_{\text{transverse}}$
$Q_1 = Q_1[r_1]$, $Q_2 = Q_2[r_2]$	$r_{eq} = \left(r_1 r_2^2\right)^{1/3}$

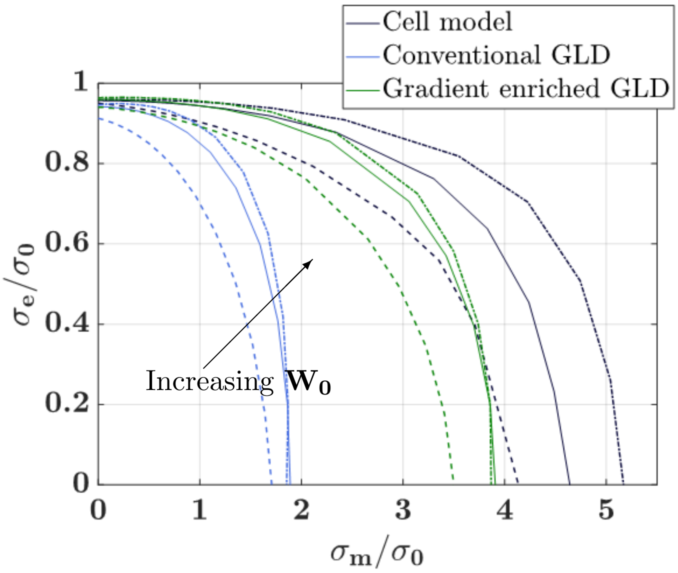

Figure 6.5. Yield surfaces for a gradient strengthening material with $L_D/r_{eq} = 0.6$ predicted by the unit cell model. The gradient enriched GLD model has Q_1 and Q_2 parameters relating to a dissipative length scale normalised with the void radius length through $Q_1 = Q_1[r_{eq}]$ and $Q_2 = Q_2[r_{eq}]$. Three different initial void radii are considered: $W_0 = 1/3$ given by the dashed curves, $W_0 = 1$ given by the fully drawn curves, and $W_0 = 3$ given by the dotted curves. The conventional GLD yield surfaces are shown as a reference.

radii, r_v, exists. An equivalent radius given as $r_{eq} = (r_1 r_2^2)^{1/3}$, where r_1 is the axial radius and r_2 the transverse radius in Fig. 6.1, might be used. The equivalent radius will take the same value for all void shapes for a given initial void volume fraction. The axial and transverse radii of the void might also be used by themselves. Three configurations of Q_1, Q_2, and void radii are explored for this work: $Q_1 = Q_1[r_{eq}]$ and $Q_2 = Q_2[r_{eq}]$, $Q_1 = Q_1[r_1]$ and $Q_2 = Q_2[r_{eq}]$, and $Q_1 = Q_1[r_1]$ and $Q_2 = Q_2[r_2]$, summed up in Table 6.1. All possible configurations of Q_1 and Q_2 have been investigated and these were chosen as they were found to yield the best results. Figure 6.5 shows the yield surface for a material with $L_D/r_0 = 0.6$ for three initial void shapes $W_0 = 1/3$, 1 and 3 as predicted by the cell model. The general observation is that for smaller void sizes, i.e., larger L_D/r_0 values, the yield surfaces shift up along both the von Mises stress axis and the mean stress axis. The gradient enriched GLD model takes Q_1 and Q_2 as functions of r_{eq} and is seen to capture the shift along the von Mises axis well. However, for the mean stress, the trend of a shift along the axis with increasing length scale parameter is captured by the gradient enriched GLD model, but the predictions are far from accurate. The spread in the yield surfaces with gradient strengthening for the different W_0-values predicted by the cell model is not captured. The gradient enriched GLD yield surfaces have the same shape as the conventional ones, and the crossing of yield surfaces for $W_0 = 1$ and $W_0 = 3$ is predicted at the same value of ρ as for the conventional material. Relating both the Q_1 and Q_2 parameters to the equivalent radius is not sufficient to model the effects of gradient strengthening for different void shapes.

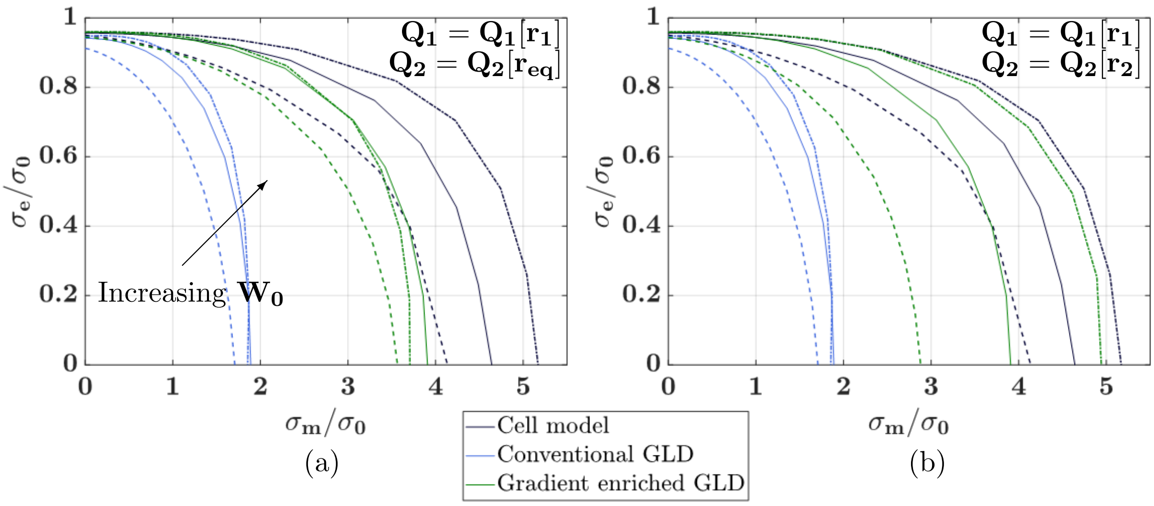

Figure 6.6. Yield surfaces for a gradient strengthening material with $L_D/r_{eq} = 0.6$ predicted by the unit cell model. Corresponding predictions from the gradient enriched GLD model with Q_1 and Q_2 updated as (a) $Q_1 = Q_1[r_1]$ and $Q_2 = Q_2[r_{eq}]$, and (b) $Q_1 = Q_1[r_1]$ and $Q_2 = Q_2[r_2]$.Three different initial void radii are considered: $W_0 = 1/3$ given by the dashed curves, $W_0 = 1$ given by the fully drawn curves, and $W_0 = 3$ given by the dotted curves. The conventional GLD yield surfaces are shown as a reference.

Next, keeping Q_2 as a function of r_{eq} and updating Q_1 to depend on r_1 is discussed. The results are presented in Fig. 6.6a, with benchmark results from the unit cell model and the conventional GLD yield surfaces. The shift along the von Mises stress axis is captured by the gradient enriched GLD model also in this case. The same trend for the mean stress axis is observed as in Fig. 6.5. The gradient enriched GLD yield surface does not capture the spread of the curves with increasing L_D/r_0 and different W_0-values. However, for this configuration, where $Q_1 = Q_1[r_1]$, the crossing of the yield surfaces for $W_0 = 1$ and $W_0 = 3$ occur at a lower value of ρ than for the conventional material. This indicates that by changing normalisation radius to one that is unique for the given void shape, it is possible to predict shape-dependent yield surfaces. Figure 6.6b shows the gradient enriched GLD yield surface with $Q_1 = Q_1[r_1]$ and $Q_2 = Q_2[r_2]$ for three different initial void shapes: $W_0 = 1/3$, 1 and 3. The results are compared to corresponding predictions from the unit cell model. The shift along the von Mises stress axis is captured. The gradient enriched GLD model does not accurately predict the shift along the mean stress axis. However, the spread in the yield surfaces consistent with increasing length scale parameter and different initial void shapes is captured. This is again indicative of the possibility of predicting shape-dependent yield surfaces by using different void radii for the different void shapes in the gradient enriching Q_1 and Q_2-parameters.

Neither of the gradient enriched GLD yield surfaces presented here accurately predicts the corresponding results from the unit cell. The issue lies with the mean stress axis. In the original model by Niordson and Tvergaard [1], the Q_2 parameter scales the mean stress directly. However, as the mean stress does not directly enter the GLD model, the generalised hydrostatic stress, σ_{gh}, has been scaled instead. Better results could perhaps be yielded if the generalised hydrostatic stress was expressed as a function of a gradient enriched mean stress. However, the poor predictions of from the gradient enriched GLD model for the different W_0-vales considered imply that perhaps the Q_2 parameter should be void shape-dependent. Hypothetically, a new analytical expression for Q_2 where void shape is considered, could be derived by a method analogous to that of Niordson and Tvergaard. This option has not been investigated, but is considered the next step for the current work.

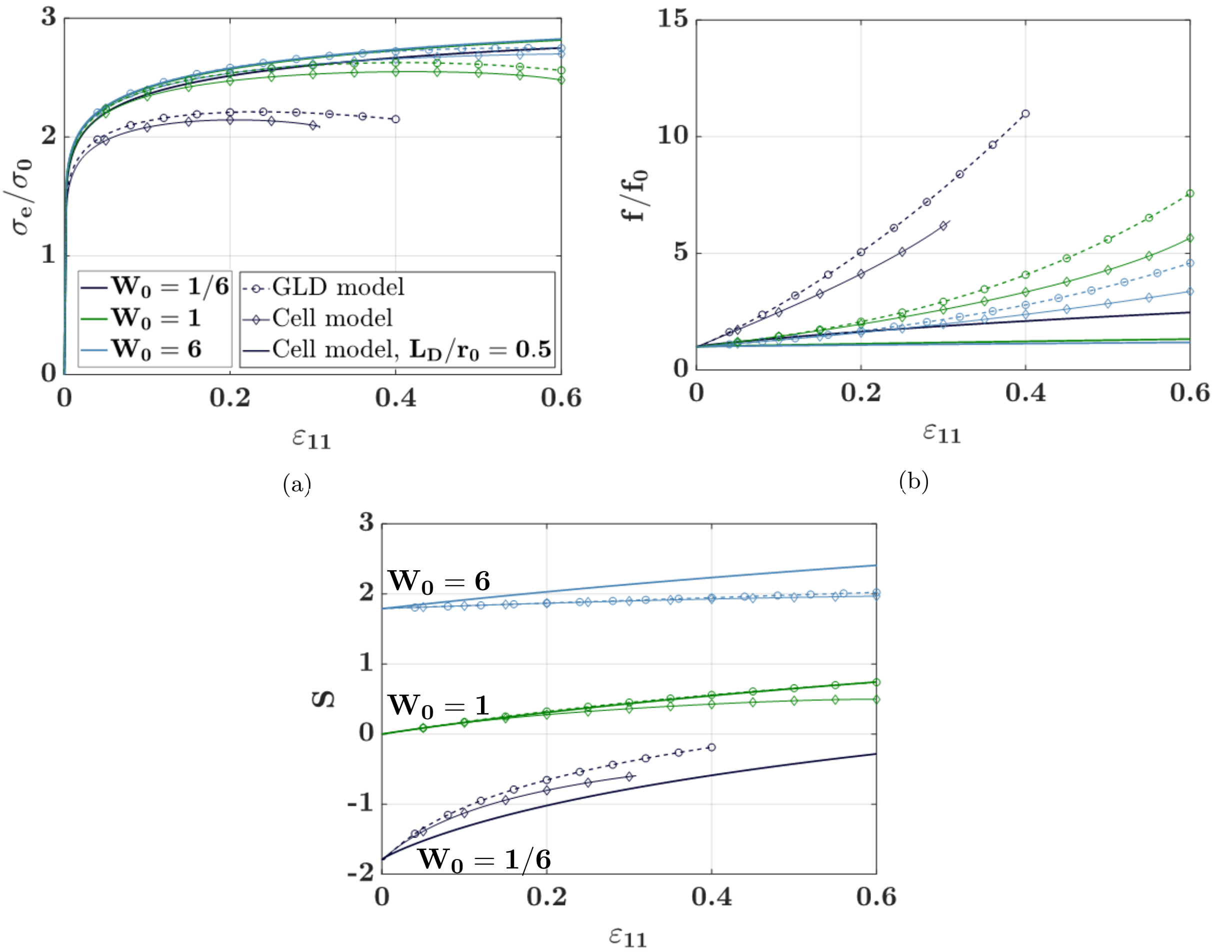

Figure 6.7. Comparison between the Gologanu-Leblond-Devaux model (∘) and void cell computations (⋄) for a conventional material with $f_0 = 0.01$, $N = 0.1$, and $W_0 = 1/6, 1$ and 1 under loading conditions giving $T = 1$. The full drawn lines are results from cell model analysis of a gradient strengthening material with $L_D/r_{eq} = 0.5$. Presented are (a) response curves showing axial stress vs. axial strain, (b) porosity evolution, and (c) void shape evolution. The logarithmic strain is given as $\varepsilon_{11} = \ln(1 + e_{11})$, where e_{11} is the engineering strain.

A preliminary investigation of combined void size and shape effects in a strain hardening material with strain hardening exponent $N = 0.1$ has been performed. The analyses are run into the plastic range to see how the response curves, void evolution, and void shape evolve with continuous deformation for voids of initial shape $W_0 = 1/6$, 1 and 6. A conventional material with $f_0 = 0.01$ has been modelled under two imposed stress states giving $T = 1$ and 3 by the Gologanu-Leblond-Devaux model. Results are compared to corresponding predictions from the unit cell model. Cell model results for a gradient strengthening material with $L_D/r_0 = 0.5$ are also presented to show the effect of gradients on the material throughout the deformation history. Figure 6.7 shows the response curves, (a), porosity evolution, (b), and the void shape evolution, (c), for all material and void shape configurations subject to loading conditions giving $T = 1$. The Gologanu-Leblond-Devaux model results are denoted ⋄, while the corresponding predictions from the unit cell models are given as ∘. The predictions from the unit cell model with a gradient strengthening material matrix are given by the fully drawn lines. It is seen that the gradient strengthening heightens the response curves and inhibits void growth. This is especially prominent for the initially oblate void, $W_0 = 1/6$. Oblate voids are more prone to localisation as the inter-void ligaments perpendicular to the main loading axis are smaller, and lower deformation values are therefore required to initiate coalescence. Gradient strengthening in the inter-void ligaments will delay localisation, reflected in the heightened response curves in Fig. 6.7a. The porosity evolution curves show the same trend of suppressed void growth with gradient strengthening. At this low value of triaxiality, $T = 1$, the relative stresses in the transverse direction are insufficient to invoke localisation for the initially spherical and prolate void. The void shape evolution curves in Fig. 6.7c show that the voids are stretched along the main axis regardless of the initial void shape for this low value of triaxiality. This is in line with results presented in Fig. 5.3 in Section 5.1. For the initially oblate void with $W_0 = 1/6$, the void shape evolution plots for the conventional material show that the void grows towards a spherical shape. However, the void shape evolution curve flattens at an axial strain value of $\varepsilon_{11} \approx 0.2$. This is the same axial stress as the peak of the response curve is found for the same configuration in Fig. 6.7a. This indicates that the localisation process has started, and the voids will ultimately grow towards coalescence. The void shape plot for the gradient strengthening material with $W_0 = 1/6$ shows no sign of stagnation, which is in line with the delay in the onset of localisation associated with gradient strengthening and the associated heightened response curve.

Similar results are presented for a loading condition giving $T = 3$ in Fig. 6.8. The response curve for the initially oblate void, $W_0 = 1/6$, in a conventional material predicted by the cell model is seen to stop as a relatively low value of axial strain. The given stress state gives large relative stresses in the transverse direction, and the voids are susceptible to transverse growth towards coalescence. Coalescence has been found to initiate at this value of strain [39] for the given configuration, and results from continued deformation are omitted. The corresponding results from the Gologanu-Leblond-Devaux model do not capture this as no coalescence criterion is applied. The model instead predicts continued material softening. This can be remedied by applying a coalescence criterion, such as the Thomson plastic limit-load model [67], to the Gologanu-Leblond-Devaux model. The conventional material responses from the Gologanu-Leblond-Devaux model are seen to deviate from the cell model for the initially spherical and prolate void in Fig. 6.8. The cell model predicts more rapid softening than the Gologanu-Leblond-Devaux model. The Gologanu-Leblond-Devaux model predicts softening only due to void growth and void shape evolution. Interaction between voids is not considered in the model, and it can theoretically predict continued softening, even if the voids are believed to have undergone coalescence. However, the cell model simulates arrays of discrete voids, and interaction between them will be taken into account. When the voids grow toward each other in the transverse direction, the surrounding plasticity fields will affect each other and accelerate the localisation process. The Gologanu-Leblond-Devaux model will not capture this and will not predict as severe softening as the cell model. The voids shape evolution plots in Fig. 6.8c show that the unit cell model and the Gologanu-Leblond-Devaux model follow each other for low axial strains until the unit cell predicts a more severe void shape change. The change in void shape evolution is seen to occur at the same value of axial strain as the onset of rapid softening for the unit cell model, $\varepsilon_{11} \approx 0.08$.

The effect of gradient strengthening is pronounced for the higher value of triaxiality, $T = 3$. At this value of triaxiality, the relative stresses in the transverse direction are sufficient to invoke localisation for the conventional material for all values of W_0 considered. The gradient strengthening material has a sizeable dissipative length scale parameter relative to the initial void, $L_D/r_0 = 0.5$, and the gradient strengthening is expected to be profound. The response curves show that the gradients are sufficient to impede localisation, and the material will be able to withstand higher stresses, heightening the response curves. The effect is most prominent for the initially oblate void, $W_0 = 1/6$, as this is the void shape most prone to localisation in a

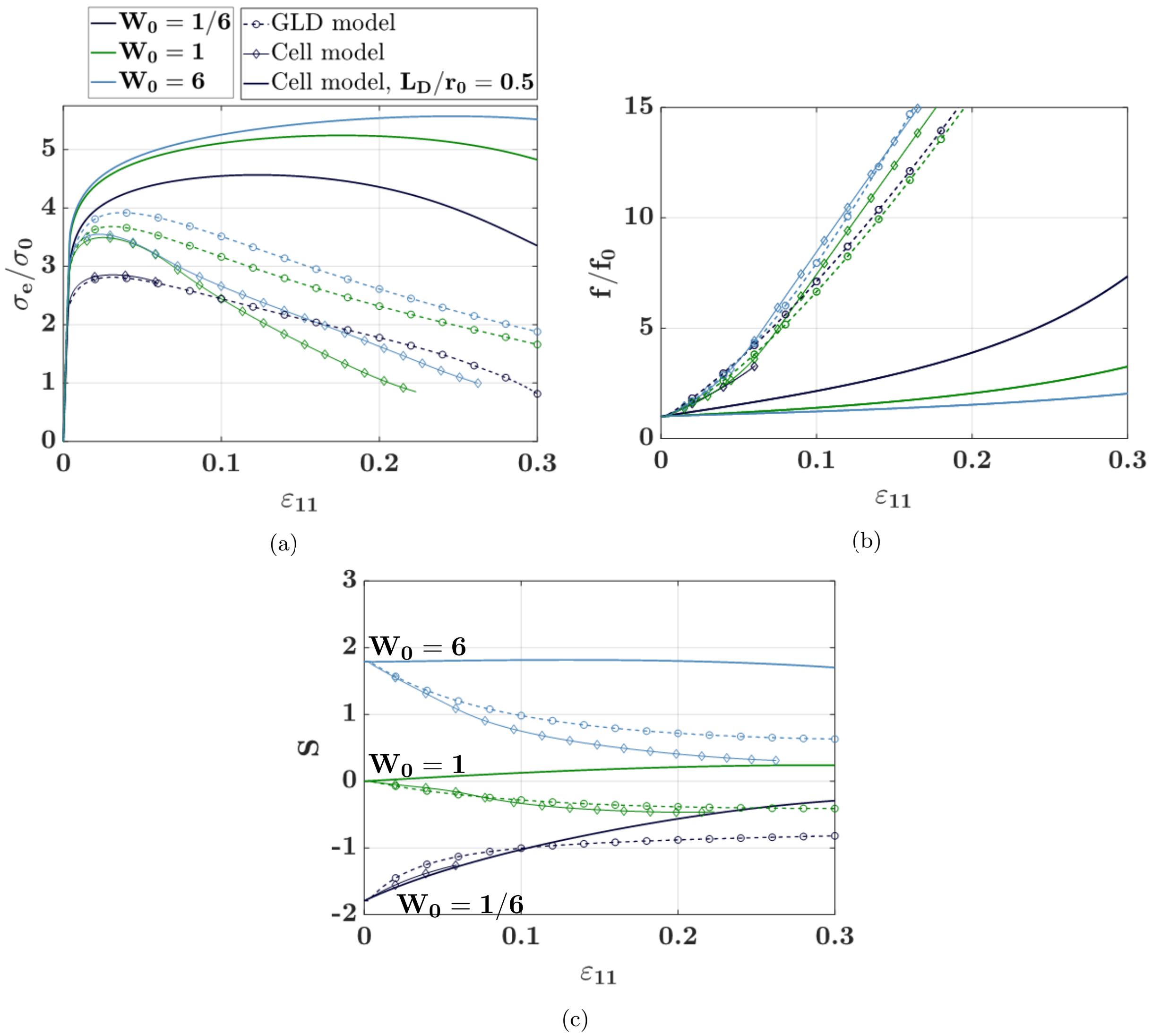

Figure 6.8. Comparison between the Gologanu-Leblond-Devaux model (○) and void cell computations (◇) for a conventional material with $f_0 = 0.01$, $N = 0.1$, and $W_0 = 1/6, 1$ and 1 under loading conditions giving $T = 3$. The full drawn lines are results from cell model analysis of a gradient strengthening material with $L_D/r_{eq} = 0.5$. Presented are (a) response curves showing axial stress vs. axial strain, (b) porosity evolution, and (c) void shape evolution. The logarithmic strain is given as $\varepsilon_{11} = \ln(1 + e_{11})$, where e_{11} is the engineering strain.

conventional material. The void shape evolution curves in Fig. 6.8c show that the void shape evolution changes with gradient strengthening. For the initially oblate void, $W_0 = 1/6$, the void in the gradient strengthening material matrix is seen to grow towards a spherical shape for the state of deformation considered here. This indicates an absence of localisation, following the heightened response curve. For the initially spherical and prolate void with $W_0 = 1$ and 6, the void shape evolution trend significantly changes with gradient strengthening. The initially spherical void is seen to grow slightly towards a prolate shape. The plastic strain gradients surrounding the void are sufficient to impede void growth in the transverse direction and thus hinder localisation. The initially prolate void is seen to keep its shape for the state of deformation considered here and will not grow towards a spherical shape nor undergo localisation.

The Gologanu-Leblond-Devaux model has not been extended to incorporate gradient strengthening effects throughout deformation. Doing so, and incorporating a coalescence criterion, is considered the next step in the ongoing work following the investigation of incorporating void shape effects in the Q_2-parameter. The goal is to predict material response, porosity evolution, and void shape evolution accurately through a gradient enriched Gologanu-Leblond-Devaux model implemented for a single-point.

6.2 Combined effects of void clustering and void size

An interesting observation for the results for the conventional material presented in Section 5.2 is that the load-carrying capacity is observed to increase with the inter-void ligament size up to a certain point, after which it will drop. This indicates that a perfectly even array is not an optimal distribution of voids, and that anisotropy in the microstructure is favoured. Melander [68] developed a theory to calculate the fracture strain of a material with a random distribution of voids. The analyses were done on unit cells with voids of equal size and cylindrical shape with a square cross-section. A perfectly plastic material was considered. The assumption is that a material deforms homogeneously until localised deformation along a row of voids intervenes. Fracture is assumed to initiate rapidly thereafter, and the fracture strain is considered equal to the strain to inhomogeneous deformation. The results showed that the fracture strain for a microstructure with a random array of voids was substantially larger than in one with a regular array. This is in line with the results presented in Section 5.2 Fig. 5.8. The stagnation or even dip of σ_e^c/σ_0 as the unit cells become cubic ($l_3/r_0 = 2.75$) indicate that a perfect array of voids results in sub-optimal material performance. The shift in deformation mechanism, from localisation of plastic flow to macroscopic, homogeneous plastic flow, associated with low triaxiality stress states or large plastic strain gradients, gives rise to higher σ_e^c/σ_0.

In continuation of the work in [P2], multi-voided cells are analysed to quantify clustering effects. Three-dimensional unit cells with a random distribution of voids are generated and meshed in MATLAB. The number of voids, their radius, and thereby also the void volume fraction are input parameters in the mesh generator. The setup allows for generating meshes with voids of different initial radii with initial void volume fraction, mean void radius, and standard deviation as input parameters. For this work, the initial void radii are kept constant. Results for the random distributions have been compared to those of a known, homogeneous distribution. The FCC unit cell with voids positioned at each corner of the cell and at the centre of each face, as shown in Fig. 6.9a, is used as the benchmark configuration for this work. The unit cell has been shifted in positive x-, y- and z-direction, rendering a unit cell with four voids placed at equal distance from each other in the representative volume element, shown in Fig. 6.9b.

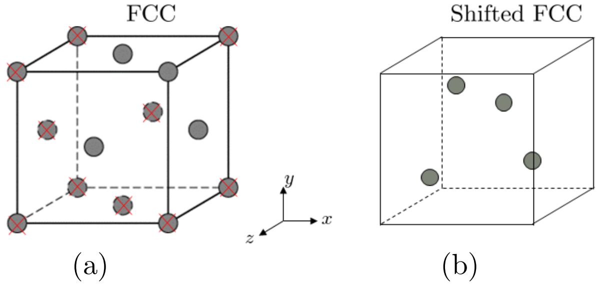

Figure 6.9. (a) An FCC unit cell where the Xs show which voids fall out of the cell when shifted in the positive x-, y- and z-direction. (b) The shifted FCC cell is the one used as a benchmark for assessment of clustering.

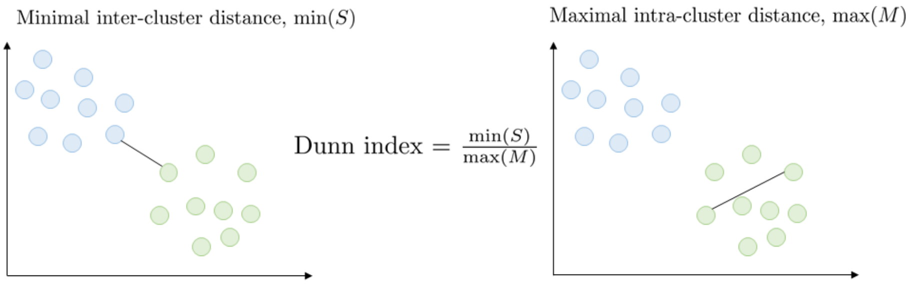

Figure 6.10. The Dunn index compares the minimum distance between voids in different clusters (left) and the largest distance within a cluster (right).

To assess the effect of clustering, the clusters generated through random positioning of the voids must be characterised. The Dunn index has been used. This is a so-called internal evaluation of clustering that aims to identify dense and well-separated clusters by quantifying the ratio between minimal inter-cluster distance and maximal intra-cluster distance. In other words, the smallest distance between voids in different clusters and the largest distance within the cluster. The Dunn index is given by

$$D = \frac{\min(S)}{\max(M)}, \tag{6.3}$$

where S is an inter-cluster distance and M an intra-cluster distance. The physical interpretation of S and M is shown in Fig. 6.10. Intuition tells that the Dunn index will get larger if the intra-cluster distance remains the same, but the closest pair between clusters are moved apart. Conversely, the Dunn index will increase if the inter-cluster distance is kept constant and the cluster is made denser by shrinking the largest intra-cluster distance. The clusters resulting in the largest Dunn index will be the ones with the largest minimum distance between clusters and smallest maximum distance between voids within a cluster. Dense, far apart clusters will have a large Dunn index.

The determination of the Dunn index should be independent of the unit cell's positioning in the material. The same cluster should have the same index regardless of how many of the cluster's voids are visible in the generated unit cell or simply present through boundary conditions. To ensure this, the Dunn index has been evaluated by first considering the coordinates of the centres of each void in the generated unit cell. The Euclidean distance to all other voids within the unit cell has then been calculated. Since the unit cell size is known, the distance from each void to all other voids in the eight neighbouring unit cells can be calculated. All the distances are put in a vector and sorted according to length. As the number of voids in a cluster is known, and the maximum intra-cluster distance can be determined as the nth smallest distance, where n is the number of voids in a cluster. The smallest inter-cluster distance will then be the $n + 1$ smallest distance. This will give a Dunn index independent of the placement of the cluster within the unit cell. A drawback of this method is that the Dunn index does not account for the smallest inter-void ligament, which is important for localisation. Different configurations may have the same Dunn index while having significantly different minimum inter-void ligament sizes. Care must therefore be taken when using this method, and a second criterion might be used. The smallest inter-void ligament is a natural measure and can be combined with the Dunn index, which has been done in this work. The clusters are categorised by the Dunn index and the smallest inter-void ligament size, and the FCC distribution values are considered as benchmarks.

The voids are embedded in a strain gradient enriched matrix using a user element subroutine (UEL), following the implementation presented in Section 4.3 for elements corresponding to the

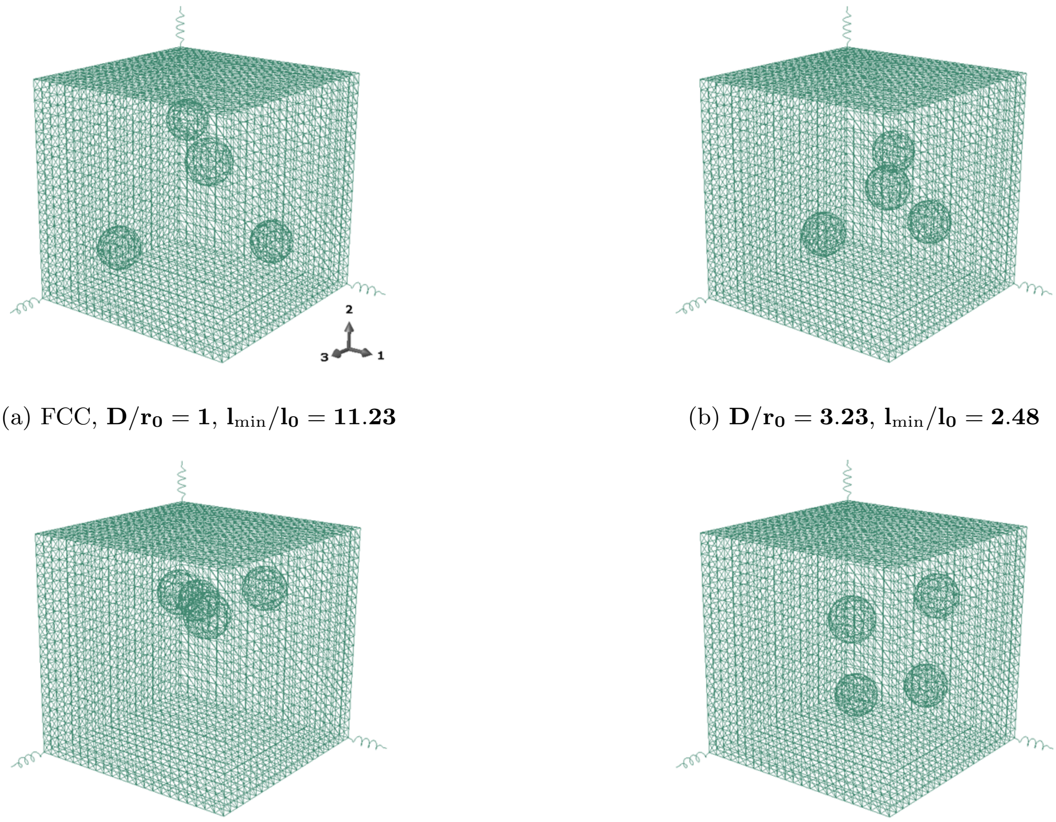

(a) FCC, $\mathbf{D/r_0 = 1}$, $\mathbf{l_{min}/l_0 = 11.23}$

(b) $\mathbf{D/r_0 = 3.23}$, $\mathbf{l_{min}/l_0 = 2.48}$

(c) $\mathbf{D/r_0 = 1.55}$, $\mathbf{l_{min}/l_0 = 1.03}$

(d) $\mathbf{D/r_0 = 1.23}$, $\mathbf{l_{min}/l_0 = 2.89}$

Figure 6.11. Finite element meshes for the FCC distribution (a) and three different clusters (b)-(d).

C3D10 elements in the ABAQUS library. See [64] for details on implementation. The finite element calculations are performed using the commercial finite element solver ABAQUS. To account for different three-dimensional stress states, prescribed stress ratios, given in Eq. (4.6), have been applied to the unit cell through the user subroutine MPC as described in Section 4.3. As symmetry cannot be exploited, the full representative volume element, must be modelled using full periodic boundary conditions. This ensures that the entire cell is constrained to predict material response under prescribed loading conditions governed by a given stress triaxiality, Eq. (4.7), and Lode parameter, Eq. (4.8). A total of five clusters have been generated. An FCC configuration based on Fig. 6.9b is generated and used as a reference. The initial void radius is the same for all four voids in the models giving the same initial void volume fraction. The initial void radius is set to $r_0 = 0.1$. The cell dimensions are 1x1x1, giving an initial void volume fraction of $f_0 = 0.017$. Examples of finite element meshes used for analysis are shown in Fig. 6.11. Figure 6.11a shows the mesh for the shifted FCC distribution with Dunn index $D/r_0 = 1$ and smallest inter-void ligament size $l_{\text{min}}/l_0 = 11.23$, where l_0 is the mesh size. The scale of the Dunn index has been shifted so that FCC has a Dunn index of 1 and the clusters have $D > 1$. Keep in mind that increasing the minimum inter-cluster distance, i.e., moving two clusters apart, and decreasing the maximum intra-cluster distance, i.e., making the cluster denser, will both increase the Dunn index. Therefore, the FCC distribution will have the smallest normalised Dunn index as the minimum inter-cluster distance, and maximum intra-cluster distance are the same for a homogeneous distribution of voids. The minimum inter-void ligament, l_{min}, is taken as the minimum distance between two void centres minus two initial void radii. Figure 6.11 shows the meshes of three of the five clusters used for analysis. The cluster with the largest normalised Dunn index, $D/r_0 = 3.23$, is shown in Fig. 6.11b. The configuration with the smallest normalised inter-void ligament, $l_{\text{min}} = 1.03$, is shown in Fig. 6.11c. An example of a cluster without any extremities is given in Fig. 6.11d. It is not obvious by looking at the meshes where the different clusters lie on the scale of Dunn indices or minimum inter-void ligament size.

Throughout simulations, the following parameters are used: $\sigma_0/E = 0.001$, $\nu = 0.3$ and $m = 0.01$, where σ_0 is the yield stress, E is Young's modulus, ν is the Poisson ratio, and m is the strain rate sensitivity exponent. The value of m is considered sufficiently small for the rate-independent material response to be approximated. A limit-load type analysis is conducted, and the material is idealised as perfectly-plastic in the absence of strain gradients. Axi-symmetric loading conditions are considered corresponding to a Lode parameter value of $L = -1$. The triaxiality illustrates the influence of imposed stress state. For all imposed stress states, ρ_2 and ρ_3 in Eqs. (4.6) will always be equal and smaller than one. In gradient strengthening materials, the dissipative length scale parameter, L_D/r_0, is normalised with the initial void radius and kept constant throughout the deformation history. The material's load-carrying capacity is determined by the critical equivalent stress found from the equivalent stress-strain curve. Figure 6.12 shows equivalent stress-strain curves for the FCC configuration for two gradient strengthening materials, $L_D/r_0 = 0.7$ and 1, and a conventional material. The overall equivalent stress, σ_e, is given by

$$\sigma_e = \frac{1}{\sqrt{2}}\sqrt{(\Sigma_{11}-\Sigma_{22})^2 + (\Sigma_{22}-\Sigma_{33})^2 + (\Sigma_{33}-\Sigma_{11})^2}, \tag{6.4}$$

where the overall stress components σ_{ij} are given by $\Sigma_{ij} = \int_V \sigma_{ij} \mathrm{d}V/V$, where V is the volume of the unit cell, including the volume of the voids. The overall equivalent strain, $\overline{E}_e$, is given by

$$\overline{E}_e = \frac{\sqrt{2}}{3}\sqrt{(E_{11}-E_{22})^2 + (E_{22}-E_{33})^2 + (E_{33}-E_{11})^2}, \tag{6.5}$$

where the strain components E_{ij} are found in a way analogous to the stress components. Figure 6.12 shows a clear size effect with increasing length scale parameters giving higher yield stress. The critical equivalent stress, σ_e^c/σ_0, is taken to be at the plateau of the equivalent stress-strain curve and is considered the onset of localisation.

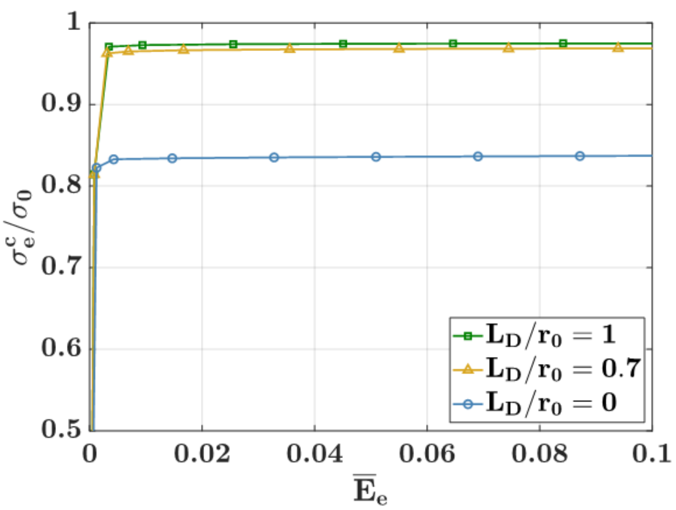

Figure 6.12. Equivalent stress strain curves for an FCC distribution under loading conditions giving $T = 2$ for a conventional material, $L_D/r_0 = 0$, and two gradient strengthening materials with dissipative length scale parameters $L_D/r_0 = 0.7$ and 1.

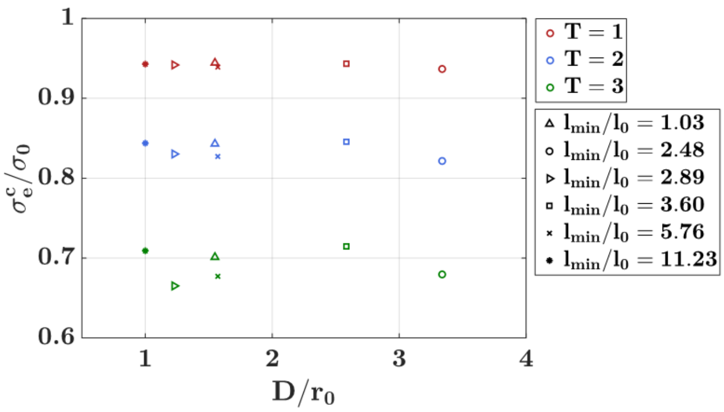

Figure 6.13. Critical equivalent stress vs. Dunn index for three values of stress triaxiality for a conventional material. The FCC configuration used as benchmark has a normalised Dunn index of $D/r_0 = 1$.

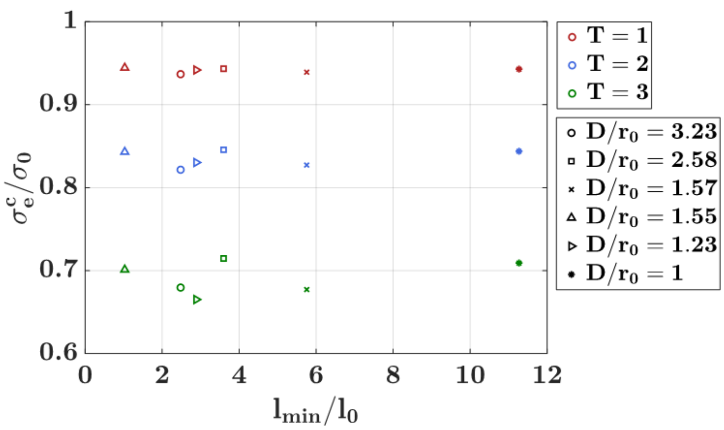

Figure 6.14. Critical equivalent stress vs. minimum inter-void ligament size in the clusters for three values of stress triaxiality for a conventional material. The FCC configuration used as benchmark has a normalised minimum inter-void ligament size of $l_{\min}/l_0 = 11.23$, where l_0 is the initial element size.

The study starts with a conventional material, i.e., $L_D/r_0 = 0$, and gradient strengthening is not present. Three values of stress triaxiality are considered: $T = 1, 2$ and 3. Five clusters with different D/r_0 and $l_{\min}/l_0$ values are analysed. The combined effects of Dunn index and triaxiality are shown in Fig. 6.13, where the critical equivalent stress, σ_e^c/σ_0, is shown as function of the normalised Dunn index, D/r_0, for all three values of stress triaxiality considered. Increasing the stress triaxiality spreads the response from the clusters with different Dunn index. Keep in mind that the FCC configuration has a Dunn index of $D/r_0 = 1$. For a low value of stress triaxiality, $T = 1$, the Dunn index has little effect on the material response. The relative stress ratio in the transverse directions, ρ_2 and ρ_3, are small for this loading state, and the dominating deformation mechanism is macroscopic plastic flow. Hence, the entire unit cell will flow at the onset of plasticity, and the response of the material will not be strongly dependent on the Dunn index. This is also why high values of critical equivalent stress found for all clusters at $T = 1$ compared to higher triaxialities. As stress is not expected to localise in the inter-void ligaments for the low triaxiality, the material can carry higher stresses before it ultimately succumbs to macroscopic yielding. Increasing the triaxiality will not only lower the critical equivalent stress of the clusters but spread it out compared to the FCC distribution. Localisation of plastic flow in the inter-void ligaments is presumed to initiate more readily for higher triaxialities, and the cluster configuration will affect the results. However, no obvious trend relating changes in critical equivalent stress to the Dunn parameter is seen in Fig. 6.13. Increasing the Dunn parameter does not give either enhanced nor diminished material performance. An interesting observation is the change in critical equivalent stress for the cluster with Dunn index $D/r_0 = 1.23$, given as $\triangleright$, compared to the cluster with Dunn index $D/r_0 = 1.57$, given as $\times$, in Fig. 6.13. The cluster with $D/r_0 = 1.23$ is seen to have a critical equivalent stress equal to the cluster with $D/r_0 = 1.57$ for $T = 1$ and $T = 2$. For $T = 3$, however, a significant drop in load-carrying capacity for the cluster with the lower Dunn index when compared to the cluster with a slightly larger Dunn index is observed. The cluster with Dunn index $D/r_0 = 1.23$ has a $l_{\min}/l_0$-value of 2.89. In contrast, the cluster with Dunn index $D/r_0 = 1.57$ has smallest inter-void ligament $l_{\min}/l_0 = 5.76$, which is significantly larger, indicating that perhaps the inter-void ligament size in a cluster is of importance for the critical equivalent stress. However, for the results for the cluster with a similar Dunn parameter, $D/r_0 = 1.55$, a significant drop in critical equivalent stress is not observed when compared to the two other clusters despite this configuration having the smallest minimum inter-void ligament of all configurations, $l_{\min}/l_0 = 1.03$. Figure 6.14 shows the combined effects of triaxiality and $l_{\min}/l_0$ on critical equivalent stress. No obvious trend based on the minimum ligament-size is observed. Take again the configuration denoted by $\triangleright$, which is now seen to experience a drop in load-carrying capacity when compared to the configuration denoted by $\circ$ with increasing triaxiality. The two clusters have similar minimum inter-void ligament sizes, $l_{\min}/l_0 = 2.48$ and $l_{\min}/l_0 = 2.89$, but significantly different Dunn indices: $D/r_0 = 1.23$ and $D/r_0 = 3.23$. The cluster with the smallest Dunn index exhibits lower critical equivalent stress than the cluster with the larger Dunn index. However, it is difficult to determine the effect of a single parameter, such as the Dunn index or the minimum inter-void ligament size, when neither parameter has been isolated.

The preliminary results show no apparent dependence of material response on either Dunn index or smallest inter-void ligament size. It is difficult to observe a trend with few results, and ideally, a big group of different clusters should be analysed to see if a trend will present itself. Another option is to predetermine either the Dunn index or the minimum inter-void ligament size and generate clusters. This will allow for investigation of each of the parameters alone and give more in-depth understanding of how these affect the material response. As the clusters are generated randomly, the generation process must be further developed to obtain predetermined values of the Dunn index, the smallest inter-void ligament size or both. A third option is to use the smallest inter-void ligament's position with respect to the main loading axis as a third characterisation criterion. The unit cells could then be rotated to give the same cluster configurations under a different axi-symmetric loading condition. Given that previous results presented in Section 5.1 and 5.2 show that the void shape and inter-void ligament size profoundly affect on the material response, it is natural to pose the hypothesis that the smallest inter-void ligament's direction to the main loading axis will also affect results. During deformation, a plane with maximum shear stress will initiate through the representative volume element. If voids are placed within this plane, localisation will presumably initiate prematurely and lower the load-carrying capacity of the material. Contrarily, suppose the voids are placed along the plane normal, i.e., perpendicular to the plane itself. In that case, the maximum shear will not act in the inter-void ligaments, and the material will be more robust. These two examples are the extremes, and a random distribution of voids will have void configurations somewhere in between. However, the notion that the placement of a given void configuration with respect to the loading axes is of importance is further rationalised by the very notion of a maximum shear plane within the representative volume element.

The effect of length scale in combination with the different clusters has been briefly investigated. The critical equivalent stress for the five clusters generated and the FCC distribution has been determined for loading conditions giving $T = 2$ for a conventional material and a gradient

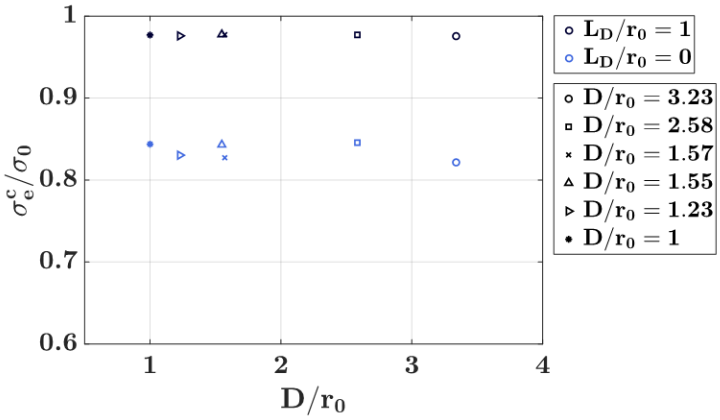

Figure 6.15. Critical equivalent stress vs. Dunn index for $T = 2$ for a conventional material and a gradient strengthening material with $L_D/r_0 = 1$. The FCC configuration used as a benchmark has a normalised Dunn index of $D/r_0 = 1$.

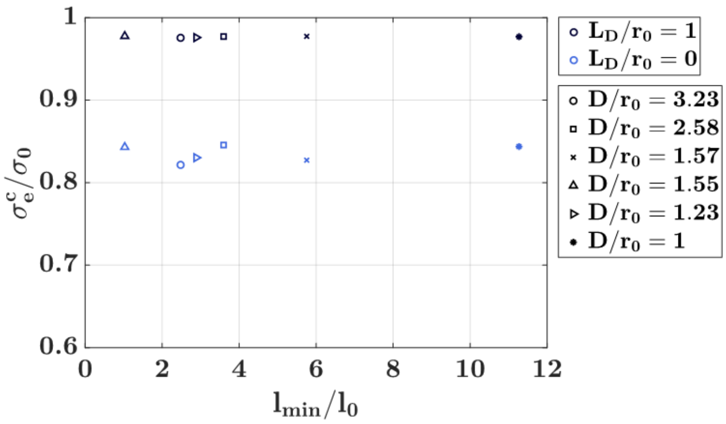

Figure 6.16. Critical equivalent stress vs. minimum inter-void ligament size in the clusters for $T = 2$ for a conventional material and a gradient strengthening material with $L_D/r_0 = 1$. The FCC configuration used as a benchmark has a normalised minimum inter-void ligament size of $l_{\min}/l_0 = 11.23$, where l_0 is the initial element size.

strengthening material with $L_D/r_0 = 1$. The results are presented in as critical coalescence stress as function of Dunn index in Fig. 6.15 and as function of minimum inter-void ligament in Fig 6.16. The general observation is that the plastic strain gradients arising in a material with such a large dissipative length scale parameter will overpower the effect of clustering and yield the same critical equivalent stress for all cluster configurations. This is in line with the results presented in Section 5.2, where a sufficiently large dissipative length scale parameter, i.e., a small microstructure, was found to increase the critical equivalent stress to a threshold value for all configurations of geometry and loading conditions considered. The gradient strengthening will impede plastic flow localisation in the inter-void ligaments and the material can withstand higher stresses until macroscopic plastic flow is initiated in the entire unit cell. The results are rendered independent of both Dunn index and inter-void ligament size. As discussed, it is difficult to characterise the clusters efficiently with only five different configurations making it challenging to quantify the effect of dissipative length scale parameters on the different cluster configurations. Further investigations into both cluster quantification and length scale effects have to be conducted to obtain conclusive results.

7. Conclusions

This thesis focuses on numerical analysis of ductile fracture from the micron-scale to the macroscale. The analysis methods span from established macroscale models such as the Gurson-Tvergaard model and the Gologanu-Leblond-Devaux model with and without extensions to account for gradient effects from the micron scale, to discrete voids embedded in a material matrix obeying a strain gradient plasticity theory. Three-dimensional unit cell analyses of both a single void and clusters of voids have been conducted to investigate the effect of plastic strain gradients on flow localisation for a range of different loading conditions.

The gradient enriched Gurson-Tvergaard model approach, Section 5.1, allows for analysis of a voided metal with damage accounted for through the void volume fraction, f, extended to incorporate gradient contributions from the micron-scale through the two length scale-dependent parameters Q_1 and Q_2. The length scale-dependent parameters enter the constitutive equations as prefactors of the usual q_1 and q_2 parameters. The gradient enriched Gurson-Tvergaard model is implemented for a single point representing a porous continuum with gradient effects accounted for in the constitutive equations. A cell model with a discrete void in a strain gradient plasticity governed matrix is used as benchmark in this work. A parametric study of stress triaxiality, T, and strain hardening exponent, N, is performed on five gradient strengthening materials. Corresponding results for a conventional material are used as a reference for the discussion of gradient effects. The gradient enriched Gurson-Tvergaard model was found to capture the elevated yield point associated with gradient strengthening. However, the length scale parameter was found to affect the void shape evolution, which will ultimately affect the material response. The gradient enriched Gurson-Tvergaard model will not capture this as the voids are accounted for solely through the damage parameter, f, the void volume fraction. The void shape evolution was found to be of significance as the inter-void ligaments, i.e., the regions between voids perpendicular to the main straining axis, are of greater importance for the material response than the void volume fraction itself. Oblate voids can withstand lower axial stresses than prolate voids due to the size of the inter-void ligaments. However, with a sufficient amount of gradient strengthening, the material will not be affected by such effects as the gradient strengthening will inhibit void evolution and thereby also localisation.

The ongoing work with the **gradient enriched Gologanu-Leblond-Devaux model**, Section 6.1, is a direct continuation of the work presented for the gradient enriched Gurson-Tvergaard model. The purpose is to predict the response of a gradient strengthening, porous metal with non-spherical void growth when subjected to a range of stress states. The starting point is an investigation of yield surfaces. Currently, gradient enriched yield surfaces following the transformation presented by Niordson and Tvergaard [1] with Q_1 and Q_2 as prefactors to f and σ_m have been produced and compared to corresponding results from an axi-symmetric unit cell model. The yield surfaces are presented in a mean stress, von Mises stress space (σ_m, σ_e). The dissipative length scale parameter associated with gradient strengthening has been investigated in relation to the several measures of the void radii found in non-spherical voids. The preliminary results show that the gradient enriched Gologanu-Leblond-Devaux model captures the adjustment along the von Mises stress axis associated with gradient strengthening. However, the shift along the mean stress axis with gradient strengthening is not well captured by the current prefactors, regardless of the void radius considered. The parameter Q_2 is directly appended to the mean stress, and better results might be presented if the Q_2 parameter is extended to include a void shape-dependent term.

The preliminary results for voids of different initial void shape deformed into the plastic range show that the void shape evolution depends to a great extent on gradient strengthening. Materials that exhibit gradient strengthening are found to have substantially less void growth in the transverse direction, which will heighten the material response curves. This is due to the gradients inhibiting plastic flow localisation. A gradient enriched Gologanu-Leblond-Devaux model, extended to account for micron-scale effects through Q_1 and a void shape dependent Q_2-parameter could in the near future predict the combined effects of void shape and size for continuous plastic deformation.

The **combined effects of inter-void ligament size and void size** on flow localisation, Section 5.2, are investigated for various stress states. The stress states are characterised by fixed values of triaxiality and Lode parameter. Three-dimensional finite element calculations of a single, initially spherical void embedded in a gradient strengthening material are performed. A conventional material is modelled and used as a reference. For the conventional material, results show that the critical coalescence stress increases with increasing inter-void ligament size. The imposed stress triaxiality determines the extent of this effect. For higher values of stress triaxiality, the relative stress in the transverse direction is increased, and the inter-void ligament size effect becomes prominent. However, above a certain threshold of inter-void ligament size, the results show a slight decrease in critical coalescence stress. This is caused by geometry and loading conditions giving rise to a transition from plastic flow localisation in the smallest inter-void ligament to $\approx 45°$ to the main loading axis. The effect is especially prominent for loading conditions corresponding to an overall state of shear and hydrostatic stress.

For the void embedded in a gradient strengthening matrix material, the critical coalescence stress is observed to increase with increasing length scale parameter, i.e., increased gradient strengthening. The propensity for plastic flow localisation in the inter-void ligaments with a high value of imposed stress triaxiality or small inter-void ligament, makes the effect of length scale parameter more prominent for configurations with either high triaxiality, small inter-void ligament sizes, or both. Localisation of plastic flow introduces large plastic strain gradients in the inter-void ligaments, which, in turn, will strengthen the ligament and delay further localisation. A large length scale parameter, i.e. small voids compared to the material length scale, will ultimately dominate the material response. There is a natural upper bound where gradient strengthening is so severe that the effects of the imposed stress state and the inter-void ligament size vanish. The critical equivalent stress becomes identical for all combinations of the unit cell geometry and loading conditions considered. A shift in localisation mechanism from plastic flow localisation to macroscopic plastic flow is observed with increasing length scale.

The ongoing work with **void clustering and void size**, Section 6.2, is done by numerical simulation of multi-voided three-dimensional unit cells with a random distribution of voids. Five different clusters have been generated along with a standard, homogeneous FCC distribution, used as a reference. The clusters are embedded in a gradient strengthening matrix material. The simulation setup allows for analysis under a range of imposed stress states characterised by fixed values of triaxiality and Lode parameter. Two criteria for cluster characterisation are put forth, the Dunn index and minimum inter-void ligament size. However, these criteria are found to be unsuitable for characterisation of the limited selection of clusters tentatively analysed. A multitude of clusters must be analysed to see how the randomly distributed voids will affect the critical coalescence stress. Another method to remedy the cluster characterisation deficiency is to add some directional measure, for example, the angle between the normal to the smallest inter-void ligament size and the main loading axis. This will allow for a cluster to be analysed under different rotations. The Dunn index will be constant, and the directional measure will change, allowing for a more consistent characterisation of clusters.

The preliminary results show that the spread in critical coalescence stress for the different clusters increases with increasing triaxiality. The deformation mechanism will shift from macroscopic plastic flow to flow localisation with increasing triaxiality. The increased spread in critical coalescence stress is therefore expected as the intra-cluster ligament sizes affect material response during localisation. Results from analyses of the clusters in a gradient strengthening material show that the gradient strengthening will decrease the spread in critical coalescence stress associated with the different clusters. This is expected and in line with previous results from work on combined effects of inter-void ligament size and void size. The gradients are found to contribute sufficient strengthening for plastic flow localisation to be limited. The unit cell will undergo macroscopic plastic flow, and the intra-cluster ligament sizes will become insignificant to the material response.

This thesis provides an investigation of extensions to the micron-scale of existing material models for ductile failure concerning material response to different loading conditions. The analysis method has given non-trivial results and is shown to be adequate for this type of study. The results obtained show that the proposed extensions to the material models contribute to better predictions of material behaviour but are, even with extensions, insufficient to provide satisfactory descriptions of the material behaviour. The thesis also investigates the micro-mechanical mechanisms that drive the void growth process. The study has demonstrated how loading conditions, inter-void ligament size and microstructure size affect the material response and damage accumulation. The results contribute to a better understanding of material behaviour. However, there is a need to continue this type of research to develop better material descriptions and understanding of the ductile failure mechanisms.

References

[1] C.F. Niordson and V. Tvergaard. A homogenized model for size-effects in porous metals. *Journal of the Mechanics and Physics of Solids*, 123:222–233, 2019.

[2] W. D. Nix. Mechanical properties of thin films. *Metallurgical transactions A*, 20(11):2217, 1989.

[3] M.S. De Guzman, G. Neubauer, P. Flinn, and W.D. Nix. The role of indentation depth on the measured hardness of materials. *MRS Online Proceedings Library Archive*, 308, 1993.

[4] N.A. Stelmashenko, M.G. Walls, L.M. Brown, and Yu.V. Milman. Microindentations on W and Mo oriented single crystals: an stm study. *Acta Metallurgica et Materialia*, 41(10): 2855–2865, 1993.

[5] Q. Ma and D.R. Clarke. Size dependent hardness of silver single crystals. *Journal of Materials Research*, 10(4):853–863, 1995.

[6] W.J. Poole, M.F. Ashby, and N.A. Fleck. Micro-hardness of annealed and work-hardened copper polycrystals. *Scripta Materialia*, 34(4):559–564, 1996.

[7] K.W. McElhaney, J.J. Vlassak, and W.D. Nix. Determination of indenter tip geometry and indentation contact area for depth-sensing indentation experiments. *Journal of Materials research*, 13(5):1300–1306, 1998.

[8] J.S. Stölken and A.G. Evans. A microbend test method for measuring the plasticity length scale. *Acta Materialia*, 46(14):5109–5115, 1998.

[9] N.A. Fleck, G.M. Muller, M.F. Ashby, and J.W. Hutchinson. Strain gradient plasticity: theory and experiment. *Acta Metallurgica et Materialia*, 42(2):475–487, 1994.

[10] L. Valdevit and John W. Hutchinson. *Plasticity Theory at Small Scales*, pages 2147–2154. Springer Netherlands, Dordrecht, 2012.

[11] R.E. Rudd and J.F. Belak. Void nucleation and associated plasticity in dynamic fracture of polycrystalline copper: an atomistic simulation. *Computational materials science*, 24(1-2): 148–153, 2002.

[12] E.T. Seppälä, J.F. Belak, and R.E. Rudd. Effect of stress triaxiality on void growth in dynamic fracture of metals: a molecular dynamics study. *Physical Review B*, 69(13):134101, 2004.

[13] E.T. Seppälä, J.F. Belak, and R.E. Rudd. Onset of void coalescence during dynamic fracture of ductile metals. *Physical review letters*, 93(24):245503, 2004.

[14] E.T. Seppälä, J.F. Belak, and R.E. Rudd. Three-dimensional molecular dynamics simulations of void coalescence during dynamic fracture of ductile metals. *Physical Review B*, 71 (6):064112, 2005.

[15] J. Marian, J. Knap, and M. Ortiz. Nanovoid cavitation by dislocation emission in aluminum. *Physical review letters*, 93(16):165503, 2004.

[16] J. Marian, J. Knap, and M. Ortiz. Nanovoid deformation in aluminum under simple shear. *Acta Materialia*, 53(10):2893–2900, 2005.

[17] E.M. Traiviratana, S.and Bringa, D.J. Benson, and M.A. Meyers. Void growth in metals: atomistic calculations. *Acta Materialia*, 56(15):3874–3886, 2008.

[18] V.A. Lubarda, M.S. Schneider, D.H. Kalantar, B.A. Remington, and M.A. Meyers. Void growth by dislocation emission. *Acta Materialia*, 52(6):1397–1408, 2004.

[19] A.L. Gurson. Continuum theory of ductile rupture by void nucleation and growth. part I: yield criteria and flow rules for porous ductile media. *Journal of Engineering Materials and Technology*, 99(1):2–15, 1977.

[20] V. Tvergaard. Influence of voids on shear band instabilities under plane strain conditions. *International Journal of Fracture*, 17(4):389–407, 1981.

[21] V. Tvergaard. Ductile fracture by cavity nucleation between larger voids. *Journal of the Mechanics and Physics of Solids*, 30(4):265–286, 1982.

[22] M. Gologanu, J.-B. Leblond, and J. Devaux. Approximate models for ductile metals containing non-spherical voids—case of axisymmetric prolate ellipsoidal cavities. *Journal of the Mechanics and Physics of Solids*, 41(11):1723–1754, 1993.

[23] M. Gologanu, J.-B. Leblond, and J. Devaux. Approximate models for ductile metals containing nonspherical voids—case of axisymmetric oblate ellipsoidal cavities. *Journal of Engineering Materials and Technology*, 116:290–297, 1994.

[24] M. Gologanu, J.-B. Leblond, G. Perrin, and J. Devaux. Recent extensions of gurson's model for porous ductile metals. In *Continuum micromechanics*, pages 61–130. Springer Verlag, Berlin, 1997.

[25] H. Gao and Y. Huang. Geometrically necessary dislocation and size-dependent plasticity. *Scripta Materialia*, 48(2):113–118, 2003.

[26] R.K. Abu Al-Rub and G.Z. Voyiadjis. Analytical and experimental determination of the material intrinsic length scale of strain gradient plasticity theory from micro-and nano-indentation experiments. *International Journal of Plasticity*, 20(6):1139–1182, 2004.

[27] M.F. Ashby. The deformation of plastically non-homogeneous materials. *The Philosophical Magazine: A Journal of Theoretical Experimental and Applied Physics*, 21(170):399–424, 1970.

[28] J.F. Nye. Some geometrical relations in dislocated crystals. *Acta metallurgica*, 1(2):153–162, 1953.

[29] A.H. Cottrell. *The Mechanical Properties of Matter*. Wiley Series on the Science and Technology of Materials. Wiley, 1964.

[30] W.M. Garrison Jr and N.R. Moody. Ductile fracture. *Journal of Physics and Chemistry of Solids*, 48(11):1035–1074, 1987.

[31] J.R. Rice and R. Thomson. Ductile versus brittle behaviour of crystals. *The Philosophical Magazine: A Journal of Theoretical Experimental and Applied Physics*, 29(1):73–97, 1974.

[32] J.W. Hutchinson and N. Fleck. Strain gradient plasticity. *Advances in applied mechanics*, 33:295–361, 1997.

[33] B. Liu, X. Qiu, Y. Huang, K.C. Hwang, M. Li, and C. Liu. The size effect on void growth in ductile materials. *Journal of the Mechanics and Physics of Solids*, 51(7):1171 – 1187, 2003.

[34] F.A. McClintock. A criterion for ductile fracture by the growth of holes. *Journal of Applied Mechanics*, 35(2):363–371, 1968.

[35] J.R. Rice and D.M. Tracey. On the ductile enlargement of voids in triaxial stress fields. *Journal of the Mechanics and Physics of Solids*, 17(3):201–217, 1969.

[36] V. Tvergaard. Influence of voids on shear band instabilities under plane strain conditions. *International Journal of fracture*, 17(4):389–407, 1981.

[37] V. Tvergaard. On localization in ductile materials containing spherical voids. *International Journal of fracture*, 18(4):237–252, 1982.

[38] V. Tvergaard and A. Needleman. Analysis of the cup-cone fracture in a round tensile bar. *Acta metallurgica*, 32(1):157–169, 1984.

[39] T. Pardoen and J.W. Hutchinson. An extended model for void growth and coalescence. *Journal of the Mechanics and Physics of Solids*, 48(12):2467–2512, 2000.

[40] L. Dormieux and D. Kondo. An extension of gurson model incorporating interface stresses effects. *International Journal of Engineering Science*, 48(6):575–581, 2010.

[41] G. Monchiet, V.and Bonnet. A gurson-type model accounting for void size effects. *International Journal of Solids and Structures*, 50(2):320–327, 2013.

[42] A. Needleman. Void growth in an elastic-plastic medium. *Journal of Applied Mechanics*, 39(4):964–970, 1972.

[43] J. Koplik and A. Needleman. Void growth and coalescence in porous plastic solids. *International Journal of Solids and Structures*, 24(8):835–853, 1988.

[44] E.C. Aifantis. On the microstructural origin of certain inelastic models. *Journal of Engineering Materials and Technology*, 106(4):326–330, 1984.

[45] E. C. Aifantis. The physics of plastic deformation. *International journal of plasticity*, 3(3): 211–247, 1987.

[46] E.C. Aifantis. On the role of gradients in the localization of deformation and fracture. *International Journal of Engineering Science*, 30(10):1279–1299, 1992.

[47] E.C. Aifantis. Strain gradient interpretation of size effects. In *Fracture Scaling*, pages 299–314. Springer, 1999.

[48] H.-B. Mühlhaus and E.C. Alfantis. A variational principle for gradient plasticity. *International Journal of Solids and Structures*, 28(7):845–857, 1991.

[49] H. Gao, Y. Huang, W.D. Nix, and J.W. Hutchinson. Mechanism-based strain gradient plasticity—i. theory. *Journal of the Mechanics and Physics of Solids*, 47(6):1239–1263, 1999.

[50] Y. Huang, S. Qu, K.C. Hwang, M. Li, and H. Gao. A conventional theory of mechanism-based strain gradient plasticity. *International Journal of Plasticity*, 20(4-5):753–782, 2004.

[51] N.A. Fleck and J.W. Hutchinson. A reformulation of strain gradient plasticity. *Journal of the Mechanics and Physics of Solids*, 49(10):2245–2271, 2001.

[52] N.A. Fleck and J.W. Hutchinson. A phenomenological theory for strain gradient effects in plasticity. *Journal of the Mechanics and Physics of Solids*, 41(12):1825–1857, 1993.

[53] C.F. Niordson and J.W. Hutchinson. On lower order strain gradient plasticity theories. *European Journal of Mechanics-A/Solids*, 22(6):771–778, 2003.

[54] M. Kuroda and V. Tvergaard. A finite deformation theory of higher-order gradient crystal plasticity. *Journal of the Mechanics and Physics of Solids*, 56(8):2573–2584, 2008.

[55] P. Gudmundson. A unified treatment of strain gradient plasticity. *Journal of the Mechanics and Physics of Solids*, 52(6):1379–1406, 2004.

[56] M.E. Gurtin and L. Anand. A theory of strain-gradient plasticity for isotropic, plastically irrotational materials. part i: Small deformations. *Journal of the Mechanics and Physics of Solids*, 53(7):1624–1649, 2005.

[57] M.E. Gurtin. A gradient theory of small-deformation isotropic plasticity that accounts for the burgers vector and for dissipation due to plastic spin. *Journal of the Mechanics and Physics of Solids*, 52(11):2545–2568, 2004.

[58] N.A. Fleck and J.R. Willis. A mathematical basis for strain-gradient plasticity theory: Part II: tensorial plastic multiplier. *Journal of the Mechanics and Physics of Solids*, 57(7): 1045–1057, 2009.

[59] J.F.W. Bishop and R. Hill. A theory of the plastic distortion of a polycrystalline aggregate under combined stresses. *The London, Edinburgh, and Dublin Philosophical Magazine and Journal of Science*, 42(327):414–427, 1951.

[60] T. Pardoen. Numerical simulation of low stress triaxiality ductile fracture. *Computers & structures*, 84(26-27):1641–1650, 2006.

[61] M.E. Gurtin. A gradient theory of single-crystal viscoplasticity that accounts for geometrically necessary dislocations. *Journal of the Mechanics and Physics of Solids*, 50(1):5–32, 2002.

[62] N. Ohno and D. Okumura. Higher-order stress and grain size effects due to self-energy of geometrically necessary dislocations. *Journal of the Mechanics and Physics of Solids*, 55 (9):1879–1898, 2007.

[63] N.A. Fleck and J.R. Willis. A mathematical basis for strain-gradient plasticity theory—part I: Scalar plastic multiplier. *Journal of the Mechanics and Physics of Solids*, 57(1):161–177, 2009.

[64] E. Martínez-Pañeda, V.S. Deshpande, C.F. Niordson, and N.A. Fleck. The role of plastic strain gradients in the crack growth resistance of metals. *Journal of the Mechanics and Physics of Solids*, 126:136–150, 2019.

[65] K.L. Nielsen and C.F. Niordson. A 2d finite element implementation of the fleck–willis strain-gradient flow theory. *European Journal of Mechanics-A/Solids*, 41:134–142, 2013.

[66] C. Tekoğlu, J.W. Hutchinson, and T. Pardoen. On localization and void coalescence as a precursor to ductile fracture. *Philosophical Transactions of the Royal Society A: Mathematical, Physical and Engineering Sciences*, 373(2038):20140121, 2015.

[67] P.F. Thomason. Three-dimensional models for the plastic limit-loads at incipient failure of the intervoid matrix in ductile porous solids. *Acta Metallurgica*, 33(6):1079–1085, 1985.

[68] A. Melander. Computer simulation of ductile fracture in a random distribution of voids. *Materials Science and Engineering*, 39(1):57–63, 1979.

[69] D. Lassance, D. Fabregue, F. Delannay, and T. Pardoen. Micromechanics of room and high temperature fracture in 6xxx al alloys. *Progress in materials science*, 52(1):62–129, 2007.

A. Yield surface parameters and derivatives

A.1 Yield surface parameters

Gologanu et al. [22–24] derived the yield surface in Eq. (3.31) by considering a spheroidal prolate or oblate void with semi-axes R_1 and R_2, embedded in a representative cell which has the shape of a confocal spheroid with semi-axes r_1 and r_2, illustrated in Fig. A.1. We let $c \equiv \left|R_1^2 - R_2^2\right|^{1/2} \equiv \left|r_1^2 - r_2^2\right|^{1/2}$ denote the focal distance, and e_1 and e_2 the eccentricities of the inner and outer spheroids. Such a geometry can be characterised by two dimensionless parameters, for instance, porosity, f, and the shape parameter, S. These parameters are defined by $f \equiv (R_1 R_2^2)/(r_1 r_2^2)$ and $S \equiv \ln(R_1/R_2)$, respectively. The inner and outer eccentricities can be calculated in terms of these parameter through

$$e_1 = \sqrt{1 - \frac{1}{\exp(2|S|)}}, \tag{A.1}$$

$$\frac{(1-e_2^2)^n}{e_2^3} = \frac{1}{f}\frac{(1-e_1^2)^n}{e_1^3} \quad \text{with} \quad \begin{cases} n = 1, & \text{for prolate voids,} \quad S \geq 0 \\ n = 1/2, & \text{for oblate voids,} \quad S < 0. \end{cases} \tag{A.2}$$

where Eq. (A.1) delivers e_1 directly and a solution for e_2 is approximated by iterations of Eq. (A.2).

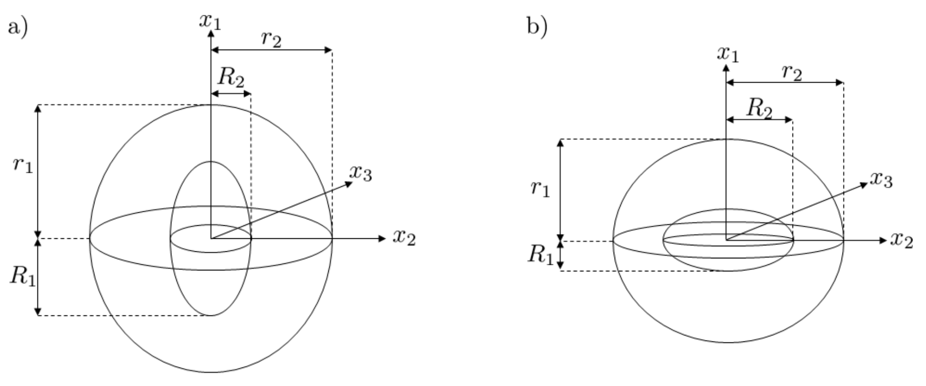

Figure A.1. Spheroidal prolate (a) and oblate (b) voids in a confocal spheroidal cell.

The dummy parameters dependent on void shape and porosity for the GLD yield surface in Eq. (3.31) are defined by Gologanu et al. [24], Pardoen and Hutchinson [39] given below:

Yield surface parameters and derivatives

Prolate voids ($S > 0$)

$$g = 0 \tag{A.3}$$

$$\alpha_1 = \frac{e_1 - (1-e_1^2)\tanh^{-1}(e_1)}{2e_1^3}, \quad \tanh^{-1}(e_1) = \frac{1}{2}\ln\left(\frac{2}{1-e_1} - 1\right) \tag{A.4}$$

$$\alpha_1^G = \frac{1}{3-e_1^2} \tag{A.5}$$

$$\alpha_2 = \frac{1-e_2^2}{3+e_2^4} \tag{A.6}$$

$$\kappa^{-1} = \frac{1}{\sqrt{3}} + \frac{1}{\ln(f)}\left(\left(\sqrt{3}-2\right)\ln\left(\frac{e_1}{e_2}\right)\right) + \frac{1}{\ln(f)}\left(\frac{1}{\sqrt{3}}\ln\left(\frac{3+e_2^2+2\sqrt{3+e_2^4}}{3+e_1^2+2\sqrt{3+e_1^4}}\right) + \ln\left(\frac{\sqrt{3}+\sqrt{3+e_1^4}}{\sqrt{3}+\sqrt{3+e_2^4}}\right)\right) \tag{A.7}$$

Oblate voids ($S < 0$)

$$g = \frac{e_2^3}{\sqrt{1-e_2^2}} \tag{A.8}$$

$$\alpha_1 = \frac{-e_1(1-e_1^2) + \sqrt{1-e_1^2}\sin^{-1}(e_1)}{2e_1^3} \tag{A.9}$$

$$\alpha_1^G = \frac{1-e_1^2}{3-2e_1^2} \tag{A.10}$$

$$\alpha_2 = \frac{(1-e_2^2)(1-2e_2^2)}{3-6e_2^2+4e_2^4} \tag{A.11}$$

$$g_f = \frac{g}{g+f} \tag{A.12}$$

$$g_1 = \frac{g}{g+1} \tag{A.13}$$

$$\kappa^{-1} = \frac{2}{3} + \frac{1}{\ln(g_f/g_1)}\left(\frac{2}{3}(g_f - g_1) + \frac{2}{5}\left(g_f^{5/2} - g_1^{5/2}\right)\left(\frac{4}{3} - g_f^{5/2} - g_1^{5/2}\right)\right) \tag{A.14}$$

while for both prolate and oblate voids

$$sh \equiv \sinh(2\kappa(\alpha_1 - \alpha_2)) \tag{A.15}$$

$$ch \equiv \cosh(2\kappa(\alpha_1 - \alpha_2)) \tag{A.16}$$

$$\eta = -\frac{\kappa(1-f)(g+1)(g+f)sh}{(g+1)^2 + q^2(g+f)^2 + 2q(g+1)(g+f)[\kappa(\alpha_1-\alpha_2)sh - ch]} \tag{A.17}$$

$$C = -\frac{\kappa(g+1)(g+f)sh}{\eta(1-f+2\eta(\alpha_1-\alpha_2))} \tag{A.18}$$

The parameters h_1 and h_2 in the evolution law for S in Eq. (3.34) are given by

$$h_1 = \frac{9}{2}\frac{\alpha_1 - \alpha_1^G}{1-3\alpha_1}\left(1-\sqrt{f}\right)^2 \tag{A.19}$$

and

$$h_2 = \frac{1-3\alpha_1}{f} + 3\alpha_2 - 1. \tag{A.20}$$

Finally, q is the analogue of the q_1 introduced by Tvergaard [20] in the Gurson criterion [19] for spherical voids. This is considered to depend upon void shape according to

$$q = 1 + 2(q_0 - 1)\frac{\mathrm{e}^{S}}{1+\mathrm{e}^{2S}}, \tag{A.21}$$

where q_0 is the value of q for spherical voids commonly set to $q_0 = 1.47$. For a perfectly plastic material, used to find yield surfaces in Section 6.1, the heuristic parameter h_T depends upon the triaxiality through

$$h_T = \begin{cases} 1 - T^2 & \text{if} \quad (\sigma_{11} - \sigma_{22})\mathbf{tr}(\sigma_{ij}) > 0 \\ 1 - T^2/2 & \text{if} \quad (\sigma_{11} - \sigma_{22})\mathbf{tr}(\sigma_{ij}) < 0. \end{cases} \tag{A.22}$$

Pardoen and Hutchinson [39] suggested an extension to the yield surface by Gologanu et al. [24] based on cell model studies for a material following power law hardening, as given by Eq. (3.1) where N is the hardening exponent. The expression for q used in this study is presented by Lassance et al. [69] and given by

$$\begin{aligned} q &= 1.5\left|\frac{b-1}{\pi}\right| + \frac{1}{2}(b+1) \\ b &= 1 + \left(0.65 - 1.75N - 0.533f^{1/4}\right)\left(\frac{1}{2} + \frac{\tan^{-1}(2(1.2 - S_0))}{\pi} - \frac{1}{44\exp(S_0)}\right), \end{aligned} \tag{A.23}$$

which is valid for $W_0 > 0.01$. Otherwise, $q = q(W_0 = 0.01)$. The expression from Pardoen and Hutchinson [39] is dependent on triaxiality which further complicates the partial derivatives of the potential surface. As such, the parameters from Lassance et al. [69] are used for this work. The heuristic parameter h_T, however, is adjusted by Pardoen and Hutchinson [39] to dependon triaxiality, T, and the strain hardening exponent, N through

$$\begin{aligned} h_T &= 1 - 0.555T^2 - 0.045T^4 + 0.002T^6 \quad \text{for} \quad N = 0.1 \\ h_T &= 1 - 0.54T^2 - 0.034T^4 + 0.00124T^6 \quad \text{for} \quad N = 0.3. \end{aligned} \tag{A.24}$$

A.2 Yield surface derivatives

For calculating the plastic strain rate, $\dot{\varepsilon}^p_{ij} = \Lambda\frac{\partial\Phi}{\partial\sigma_{ij}}$, as well as the rate of microscopic reference stress, shown in Eq. (A.25), the yield surface derivatives should be used

$$\dot{\Phi} = 0 \quad \rightarrow \quad \dot{\sigma}_M = -\left[\frac{\partial\Phi}{\partial\sigma_M}\right]^{-1}\left[\frac{\partial\Phi}{\partial\sigma_{ij}}\dot{\sigma}_{ij} + \frac{\partial\Phi}{\partial f}\dot{f} + \frac{\partial\Phi}{\partial S}\dot{S}\right]. \tag{A.25}$$

These derivatives are shown in the following. The derivatives of the yield surface constants $(C, \eta, \kappa, g, \sigma_{gh}, q)$ are omitted, but may be supplied by the author upon request. They have been derived and controlled by a numerical finite difference check.

$$\frac{\partial \Phi}{\partial \sigma_{ij}} = \frac{C}{\sigma_M^2}\frac{\partial (B_0)^2}{\partial \sigma_{ij}} + 2q(g+1)(g+f)\sinh\left[\kappa\frac{\sigma_{gh}}{\sigma_M}\right]\frac{\kappa}{\sigma_M}\frac{\partial \sigma_{gh}}{\partial \sigma_{ij}} \tag{A.26}$$

$$\begin{aligned}\frac{\partial \Phi}{\partial f} = &\frac{\partial C}{\partial f}\frac{B_0^2}{\sigma_M^2} + \frac{C}{\sigma_M}\frac{\partial (B_0^2)}{\partial f} \\ &+ 2q(g+1)(g+f)\sinh\left[\kappa\frac{\sigma_{gh}}{\sigma_M}\right]\left(\frac{\partial \kappa}{\partial f}\frac{\sigma_{gh}}{\sigma_M} + \frac{\kappa}{\sigma_M}\frac{\partial \sigma_{gh}}{\partial \sigma_M}\right) \\ &+ 2(g+f)\left(q\cosh\left[\kappa\frac{\sigma_{gh}}{\sigma_M}\right] - \frac{g+1}{g+f}\right)\frac{\partial g}{\partial f} \\ &+ 2q(g+f)\left(\frac{g+1}{g+f}\cosh\left[\kappa\frac{\sigma_{gh}}{\sigma_M}\right] - q\right)\left(1 - \frac{\partial g}{\partial f}\right)\end{aligned} \tag{A.27}$$

$$\begin{aligned}\frac{\partial \Phi}{\partial S} = &\frac{\partial C}{\partial S}\frac{B_0^2}{\sigma_M^2} + \frac{C}{\sigma_M^2}\frac{\partial (B_0)^2}{\partial S} \\ &+ 2q(g+1)(g+f)\sinh\left[\kappa\frac{\sigma_{gh}}{\sigma_M}\right]\left(\frac{\partial \kappa}{\partial S}\frac{\sigma_{gh}}{\sigma_M} + \frac{\kappa}{\sigma_M}\frac{\partial \sigma_{gh}}{\partial S}\right) \\ &+ 2q(g+f)\left[\left(1 + \frac{g+1}{g+f}\right)\cosh\left[\kappa\frac{\sigma_{gh}}{\sigma_M}\right] - q - \frac{1}{q}\frac{g+1}{g+f}\right]\frac{\partial g}{\partial S}\end{aligned} \tag{A.28}$$

$$\frac{\partial \Phi}{\partial \sigma_M} = -2\frac{C}{\sigma_M}\frac{B_0^2}{\sigma_M^2} - 2q(g+1)(g+f)\sinh\left[\kappa\frac{\sigma_{gh}}{\sigma_M}\right]\frac{\kappa}{\sigma_M}\frac{\sigma_{gh}}{\sigma_M} \tag{A.29}$$

B. Void evolution plots

These plots serve as addition to the discussion presented in Section 5.1. The plots show the evolution of the relative void volume, f/f_0, as function of axial strain for all configurations presented in Section 5.1.

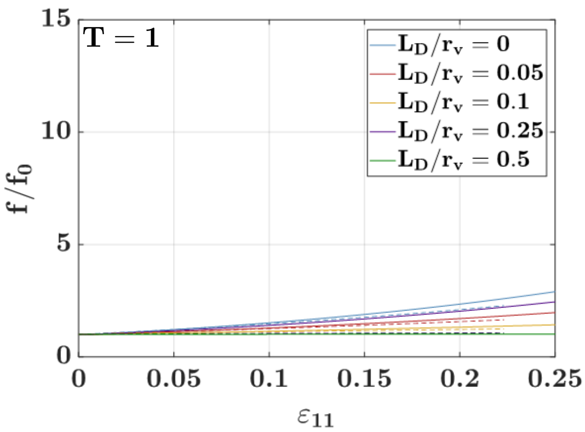

(a)

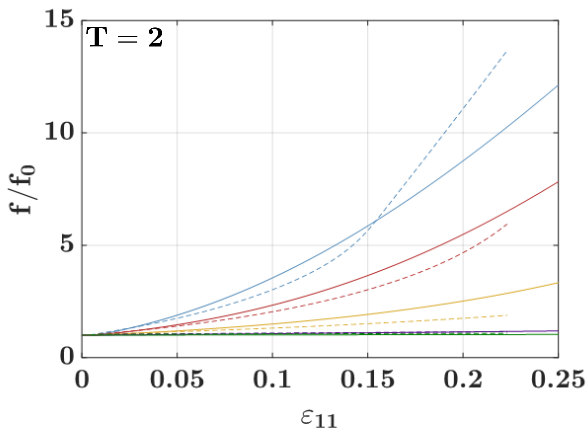

(b)

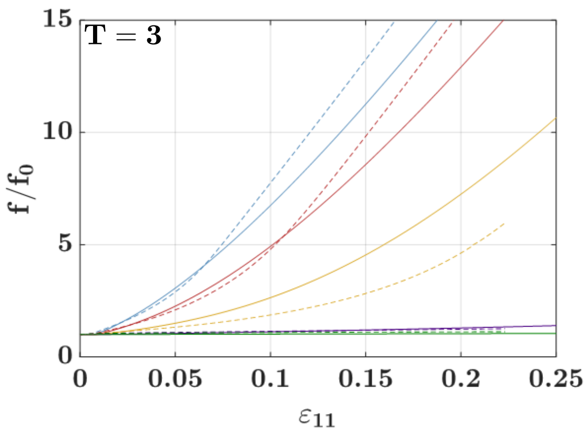

(c)

Figure B.1. Void evolution plots for $f_0 = 0.0104$, $n = 0.1$ and loading conditions giving a) $T = 1$, b) $T = 2$ and c) $T = 3$.

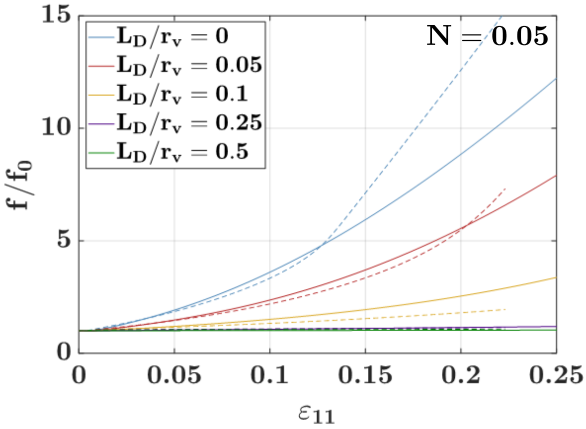

(a)

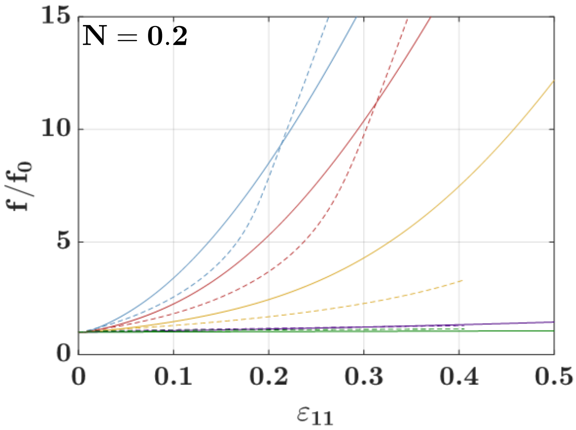

(b)

Figure B.2. Void evolution plots for $f_0 = 0.0104$ and $T = 2$ $n = 0.1$ for strain hardening materials with a) $N = 0.05$ and b) $N = 0.2$.

[P1]

Investigation of a gradient enriched Gurson-Tvergaard model for porous strain hardening materials

Ingrid Holte, Christian F. Niordson, Kim L. Nielsen, Viggo Tvergaard

Published in *European Journal of Solid Mechanics / A Solids*, **75**, 472–484, 2019

European Journal of Mechanics / A Solids 75 (2019) 472–484

Contents lists available at ScienceDirect

European Journal of Mechanics / A Solids

journal homepage: www.elsevier.com/locate/ejmsol

Investigation of a gradient enriched Gurson-Tvergaard model for porous strain hardening materials

I. Holte*, C.F. Niordson, K.L. Nielsen, V. Tvergaard

Department of Mechanical Engineering, Solid Mechanics, Technical University of Denmark, DK-2800, Kgs. Lyngby, Denmark

ARTICLE INFO

This article was presented at the IUTAM Symposium on Size-Effects in Microstructure and Damage Evolution at Technical University of Denmark 2018.

Keywords:
Size-effects
Voids
Strain-gradient plasticity

ABSTRACT

Size effects in a strain hardening porous solid are investigated using the Gurson-Tvergaard (GT) model enriched by a constitutive length parameter, as proposed by Niordson and Tvergaard [C.F. Niordson, V. Tvergaard, A homogenised model for size effects in porous metals, J. Mech. Phys. Solids (2019)]. The results are compared with unit cell calculations of regularly distributed voids embedded in a strain gradient enhanced matrix material. The strain gradient plasticity theory proposed by Fleck and Willis [N.A. Fleck, J.R. Willis, A mathematical basis for strain gradient plasticity theory. Part II: tensorial plastic multiplier, J. Mech. Phys. Solids 57 (2009) 1045–1057], extended to finite strains, is adopted for the cell model, consistent with the gradient enriched Gurson model. The gradient model allows for a material length parameter to enter the constitutive framework for dimensional consistency, while the enriched GT model has the same length parameter introduced through prefactors of the usual q_1 and q_2 factors. The continuum model featuring size-dependent Tvergaard-constants is used to investigate a strain hardening material with the strain gradient plasticity enriched cell model as reference. The two models are compared for three triaxialities, three initial void volume fractions, and three hardening exponents. The enriched GT model captures the effect of elevated yield point and suppressed void growth with increasing length parameter for all the cases investigated. The agreement between the models is good until severe void distortion or plastic flow localisation between neighbouring voids. The response curves and void growth curves for the enriched GT model deviate from those of the cell model at high axial strains. Void shape plots, which are only available for the cell model, show that the length parameter influences the shape of the void which in turn has impact on the material response curves and the void evolution. This is not captured by the enriched GT model as the voids are accounted for solely through a volume fraction parameter.

1. Introduction

Size effects in metal plasticity, exhibiting the general trend that *smaller is stronger* due to hardening associated with strain gradients, have been confirmed in many experiments. Fleck et al. (1994) showed a size effect in torsion of thin copper wires, with the onset of yielding delayed for diminishing specimen size. Stelmashenko et al. (1993) and Ma and Clarke (1995) have shown that material hardness increases with decreasing indentation size, while Stölken and Evans (1998) documented size effects in bending. Following the work of Ashby (1970), the apparent flow stress is known to be influenced by both statistically stored dislocations, created during homogeneous strain, and geometrically necessary dislocations which are related to plastic strain gradients. To account for the strain gradient effect, a number of phenomenological theories of plasticity have been developed. One such theory, proposed by Fleck and Hutchinson (1997), includes higher order stresses that are work conjugate to plastic strain gradients. Gudmundson (2004) presented a thermodynamical consistent framework and constitutive laws extending the theory presented by Fleck and Hutchinson (1997). The contribution by Gudmundson (2004), was later reformulated mathematically by Fleck and Willis (2009) and the variational structures of both rate-dependent (visco-plastic) and rate-independent versions was laid out. In the present paper, the visco-plastic formulation of the Fleck-Willis theory is used to perform cell model studies of a discrete void in a gradient enhanced strain hardening matrix. The strain gradient plasticity framework has been implemented numerically by Nielsen and Niordson (2013, 2014), and extended to finite strains in a visco-plastic setting by Niordson and Tvergaard (2019).

For porous, ductile media, the voids and their evolution affect material behaviour. In gradient hardening materials, a small void will generate large gradients, and the void evolution will not be correctly

* Corresponding author.
E-mail address: inghol@mek.dtu.dk (I. Holte).

https://doi.org/10.1016/j.euromechsol.2019.03.001
Received 30 November 2018; Received in revised form 21 February 2019; Accepted 2 March 2019
Available online 09 March 2019
0997-7538/

captured by classic plasticity theories. Wen et al. (2005) put forth an extension to the Gurson-Tvergaard (GT) model (Tvergaard, 1981, 1982) by accounting for dislocation hardening based on the theory of plasticity introduced by Gao and Huang (2001). In this theory, Taylor's dislocation hardening model and the density of geometrically necessary dislocations are linked to non-local plasticity. Monchiet and Bonnet (2013) extended the GT model to account for strain gradient effects on cavity growth. Dormieux and Kondo (2010) introduced effects of interface stresses at the cavity surface to the GT model. The interface effect was found to be controlled by a parameter depending on the cavity size, which also affected the macroscopic yield strength of the media. Monchiet and Kondo (2013) extended this to account for non-spherical voids.

Niordson and Tvergaard (2019) investigated size-effects in a porous metal based in cell model analyses of axi-symmetric loading states. They proposed that conventional yield surfaces for porous metals can be extended to account for size-effects by introducing an effective void volume fraction smaller than the actual void volume fraction, and a decreased mean stress sensitivity. The aim of the present paper is to verify the applicability of this proposal to the GT model. The conventional GT model accounts for the presence of voids solely through the void volume fraction, f. To account for size-effects originating from strain gradient effects, Niordson and Tvergaard (2019) proposed to introduce two size dependent parameters, Q_1 and Q_2, as prefactors of the void volume fraction and the mean stress, respectively, in the yield condition. A parametric study with this representation of size effects in an extended GT model is presented and the predictions are compared with corresponding unit cell model predictions, where a discrete void is embedded in a finite strain gradient matrix material of the Fleck-Willis type.

The paper is structured as follows. The work is outlined in Section 2. The material models are presented in Section 3, the gradient cell model in Section 3.1, and the enriched GT model in Section 3.2. The results are presented and discussed in Section 4, while the work is concluded in Section 5.

2. Problem formulation

Material porosity is modelled using two different approaches. One has voids represented discretely, while the other is based on a homogenised yield function of the Gurson-Tvergaard type.

The discrete model is a unit cell with matrix material governed by the gradient theory by Fleck and Willis (2009) in a finite strain generalisation, and a discretely modelled embedded void (Section 3.1). The cell model approximates an array of voids arranged in a layered hexagonal pattern (see e.g. Niordson and Tvergaard, 2019). Due to symmetry, only half of the cell is modelled with the hexagonal cell approximated by an axi-symmetric unit cell model as shown in Fig. 1b. Fig. 1a shows one cylinder with three planes of voids. The initial void plane distance is $2H_c$, the initial in-plane void distance is $2R_c$, and the initial void radius is denoted R_0. The initial void volume fraction is thereby given as

$$f_0 = \frac{2R_0^3}{3R_c^2 H_c}. \tag{1}$$

The discretely modelled void is initially spherical, but changes shape upon loading, and the shape is characterised by the aspect ratio given by

$$S = \frac{R_0 + \Delta_A}{R_0 + \Delta_B} \tag{2}$$

where Δ_A is the displacement in axial direction of the node at the boundary between the discrete void and the matrix aligned with the x_1-axis, while Δ_B is the displacement in radial direction of the node at the boundary between the discrete void and the matrix aligned with the

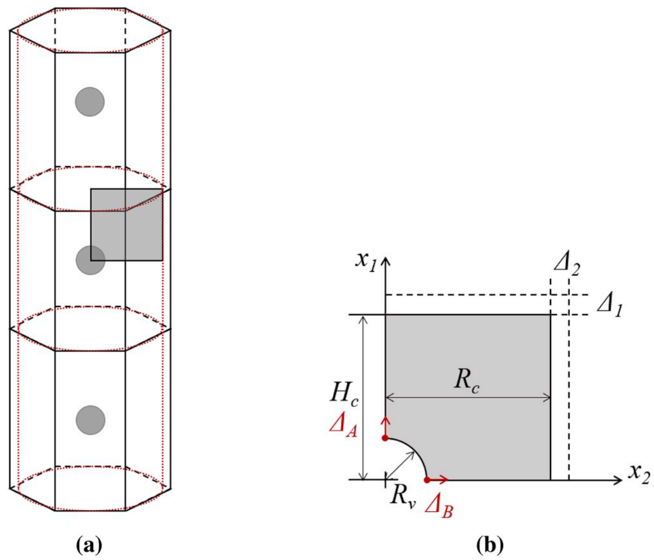

Fig. 1. a) Voids are assumed periodically arranged in hexagonal cylinders, which are modelled as circular through axi-symmetric boundary conditions. The voids are assumed to be placed in equally spaced planes. The shaded area indicates the unit cell approximation. b) the unit cell model approximation.

x_2-axis (see Fig. 1b). Thus, $S>1$ means the void is prolate, and $S<1$ corresponds to an oblate void. For a spherical void, $S = 1$. The numerical analyses are carried out using the finite element method with a mesh consisting of 480 elements, with 24 elements discretising one quarter of the circumference of the void, whereas 20 graded elements are employed in the radial direction. To determine the displacement field, eight-node, isoparametric, axi-symmetric elements are used, whereas for the plastic strain rate field, the corresponding four node elements are used (see also Section 3.1).

The homogenised model is a single point model representing a homogeneous continuum governed by the gradient enriched GT model as proposed by Niordson and Tvergaard (2019), where the porosity is represented by a void volume fraction denoted by f (see Section 3.2). The gradient enriched GT model is solved directly by forward Euler integration of an imposed stress/strain history. The strain gradient plasticity cell model has been used as benchmark for investigation of the enriched GT model in a parametric study. The investigated parameter space is given in Table 1.

In both models, a Rayleigh-Ritz method is employed to ensure a constant ratio, ρ, of transverse to axial true stresses for each increment of the analyses with a prescribed tensile displacement. The stress triaxiality is related to the stress ratio through

Table 1
Values for the parametric study of the gradient enriched GT model. The stress state triaxiality from Eq. (3) is denoted by T, while n is the hardening exponent in Eq. (8), f_0 is the initial void volume fraction in Eq. (1), and L_D is the intrinsic length parameter.

Varied parameter		Fixed parameters	Length scales, L_D/R_c
T	1, 2, 3	$n = 0.1$ $f_0 = 0.0104$	0[a], 0.05, 0.1, 0.25, 0.5
n	0.05, 0.1, 0.2	$T = 2$ $f_0 = 0.0104$	0, 0.05, 0.1, 0.25, 0.5
f_0	0.0052, 0.0104, 0.042	$T = 2$ $n = 0.1$	0, 0.05, 0.1, 0.25, 0.5

[a] The simulation has been carried out with an intrinsic length scale of $\frac{L_D}{R_c} = 10^{-4}$, which is considered sufficiently small for the material to be referred to as a conventional material.

$$T = \frac{1}{3}\left[\frac{1+2\rho}{1-\rho}\right] \quad \text{with} \quad \rho = \frac{\sigma_{22}}{\sigma_{11}}. \tag{3}$$

3. Material models

3.1. Strain gradient plasticity model

The strain gradient plasticity model is based on the visco-plastic strain gradient plasticity theory proposed by Gudmundson (2004) in the context of the mathematical formulation in terms of minimum principles as proposed by Fleck and Willis (2009). Here, the model presentation is kept brief and the reader is referred to Niordson and Tvergaard (2019) and Nielsen and Niordson (2013) for details on the finite strain extension. The theory accounts for internal elastic energy storage due to elastic strain and for dissipation due to the plastic strain rate, $\dot{\varepsilon}_{ij}^{P}$ and its spatial gradient, $\dot{\varepsilon}_{ij,k}^{P}$. The principle of Virtual Work (PVW) in Cartesian components is expressed by

$$\int_V (\sigma_{ij}\delta\dot{\varepsilon}_{ij} + (q_{ij} - s_{ij})\delta\dot{\varepsilon}_{ij}^{P} + \tau_{ijk}\delta\dot{\varepsilon}_{ij,k}^{P})\mathrm{d}V = \int_S (T_i\delta\dot{u}_i + t_{ij}\delta\dot{\varepsilon}_{ij}^{P})\mathrm{d}S \tag{4}$$

where σ_{ij} and $s_{ij} = \sigma_{ij} - \frac{1}{3}\delta_{ij}\sigma_{kk}$ are the Cauchy stress tensor and the stress deviator, respectively. The micro-stress, q_{ij}, is work conjugate to the plastic strain rate, $\dot{\varepsilon}_{ij}^{P}$, and τ_{ijk} is a higher order stress, work conjugate to the plastic strain rate gradient, $\dot{\varepsilon}_{ij,k}^{P}$. The outward unit normal to the surface S is n_i. The right hand side of the PVW includes the conventional traction, $T_i = \sigma_{ij}n_j$ work conjugate to the boundary displacement rate, $\dot{u}_i$, and the higher order traction, $t_{ij} = \tau_{ijk}n_k$, work conjugate to the plastic strain rate, $\dot{\varepsilon}_{ij}^{P}$. Balance laws for the stress quantities follow directly:

$$\sigma_{ij,j} = 0 \tag{5}$$

$$q_{ij} - s_{ij} - \tau_{ijk,k} = 0 \tag{6}$$

where, the first set of equations are the conventional equilibrium equations in the absence of body forces, and the second set are the higher order equilibrium equations.

3.1.1. Constitutive equations

The rate-dependent visco-plastic formulation employs a visco-plastic potential to account for plastic dissipation as follows

$$\Phi[\dot{E}^P, E^P] = \int_0^{\dot{E}^P} \sigma_c[\dot{E}^{P'}, E^P]\mathrm{d}\dot{E}^{P'} \tag{7}$$

Here, σ_c is the gradient enhanced effective stress, related to the current matrix flow stress through $\sigma_c = \sigma_F[E^P]\left(\frac{\dot{E}^P}{\dot{\varepsilon}_0}\right)^m$, with $\dot{\varepsilon}_0$ denoting the reference strain rate, and m denoting the rate-sensitivity exponent. For the strain hardening material in this paper, the matrix flow stress is given by the isotropic power law

$$\sigma_F = \sigma_y\left(1 + \frac{E^P}{\sigma_y/E}\right)^n \tag{8}$$

where σ_y is the initial matrix material yield stress. A gradient enhanced effective plastic strain rate is introduced by

$$(\dot{E}^P)^2 = \frac{2}{3}\dot{\varepsilon}_{ij}^{P}\dot{\varepsilon}_{ij}^{P} + L_D^2\dot{\varepsilon}_{ij,k}^{P}\dot{\varepsilon}_{ij,k}^{P} \tag{9}$$

and the associated work conjugate gradient enhanced effective stress is given by

$$\sigma_c^2 = \frac{3}{2}q_{ij}q_{ij} + \frac{1}{L_D^2}\tau_{ijk}\tau_{ijk} \tag{10}$$

where L_D is a dissipative constitutive length parameter that enters for dimensional consistency. The dissipative stress quantities are given by

$$q_{ij}^D = \frac{2}{3}\sigma_c\frac{\dot{\varepsilon}_{ij}^{P}}{\dot{E}^P}, \quad \tau_{ijk}^D = L_D^2\sigma_c\frac{\dot{\varepsilon}_{ij,k}^{P}}{\dot{E}^P}. \tag{11}$$

The superscript D refers to dissipative quantities.

3.1.2. Solution method

The incremental boundary value problem is solved using the Finite Element Method based on the two minimum principles set forward by Fleck and Willis (2009) (see Niordson and Tvergaard (2019) for details on the finite strain formulation). A forward Euler integration scheme is employed throughout Minimum Principle I, which for the time dependent solutions includes the visco-plastic potential, and reads

$$H = \inf_{\dot{\varepsilon}_{ij}^{P}} \int_V (\Phi[E^P, \dot{E}^P] + \tau_{ijk}^E\dot{\varepsilon}_{ij,k}^{P} - s_{ij}\dot{\varepsilon}_{ij}^{P})\mathrm{d}V - \int_S t_{ij}\dot{\varepsilon}_{ij}^{P}\mathrm{d}S. \tag{12}$$

The superscripts E refers to the energetic contributions Assuming that the current state of stress, σ_{ij}, and the plastic deformation, ε_{ij}^{P}, are known everywhere in the volume, the plastic strain rate field, $\dot{\varepsilon}_{ij}^{P}$, for each time step is found by requiring Eq. (12) stationary through

$$\int_V \left(q_{ij}^D\delta\dot{\varepsilon}_{ij}^{P} + \tau_{ijk}^D\delta\dot{\varepsilon}_{ij,k}^{P}\right)\mathrm{d}V = \int_V (s_{ij}\delta\dot{\varepsilon}_{ij}^{P} - \tau_{ijk}^E\delta\dot{\varepsilon}_{ij,k}^{P})\mathrm{d}V + \int_S t_{ij}\delta\dot{\varepsilon}_{ij}^{P}\mathrm{d}S. \tag{13}$$

Equation (13) is solved by an iterative procedure. This problem is taken to be purely dissipative and τ_{ijk}^E is zero. The dissipative stress quantities, q_{ij}^D and τ_{ijk}^D are found from Eq. (11). Once the plastic strain rate field is determined, Minimum Principle II (Eq. (14))

$$J[\dot{u}_i] = \frac{1}{2}\int_V L_{ijkl}(\dot{\varepsilon}_{ij} - \dot{\varepsilon}_{ij}^{P})(\dot{\varepsilon}_{kl} - \dot{\varepsilon}_{kl}^{P})\mathrm{d}V - \int_S \dot{T}_i\dot{u}_i\mathrm{d}S. \tag{14}$$

is used to calculate the corresponding displacement field in an updated Lagrangian setting following McMeeking and Rice (1975). The incrementation of the Fleck and Willis theory is conducted using a forward Euler integration scheme built into an in-house FORTRAN code. For details on the finite strain implementation, the reader is referred to Niordson and Tvergaard (2019) and Nielsen and Niordson (2013).

3.2. The gradient enriched Gurson model

The basis for the gradient enriched continuum model is a finite-strain formulation of the Gurson-Tvergaard model, which describes the behaviour of a porous elastic-plastic solid as dilating, pressure sensitive plastic flow of a solid with the yield condition $\Phi(\sigma_{ij}, \sigma_M, f) = 0$ (see Gurson, 1977; Tvergaard, 1982). Here, σ_{ij} is the average macroscopic Cauchy stress tensor, σ_M is the equivalent tensile flow stress of the matrix material, and f is the current void volume fraction. The Gurson model used here is time-independent while the gradient model is visco-plastic. Comparison is reasonable as the rate sensitivity exponent is taken to be very small. Niordson and Tvergaard (2019) recently presented a simple method for transforming a conventional yield surface for a porous material so that it accounts for size-effects. In the context of the GT model their proposal is to introduce two size-dependent parameters, Q_1 and Q_2, as prefactors to the conventional Tvergaard parameters q_1 and q_2, so that the yield condition reads:

$$\Phi = \frac{\sigma_e^2}{\sigma_M^2} + 2Q_1q_1f\cosh\left\{\frac{Q_2q_2}{2}\frac{\sigma_{kk}}{\sigma_M}\right\} - [1 + (Q_1q_1f)^2] = 0 \tag{15}$$

where $\sigma_e = (3s_{ij}s_{ij}/2)^{1/2}$ is the macroscopic equivalent stress, $s_{ij} = \sigma_{ij} - \frac{1}{3}\delta_{ij}\sigma_{kk}$ is the macroscopic Cauchy stress deviator, and δ_{ij} is the Kronecker delta. The gradient enriched Q_1 and Q_2 factors are given by:

$$Q_1 \approx \frac{0.364}{1 + 1.8\left(\frac{L_D}{R_V}\right) + 10\left(\frac{L_D}{R_V}\right)^2} + 0.636, \tag{16}$$

$$Q_2 \approx \frac{1}{1 + 1.8\left(\frac{L_D}{R_V}\right)^{3/2}} \tag{17}$$

In order to capture the evolution of size-effects with void volume fraction, the ratio of the material length scale to void size is taken to

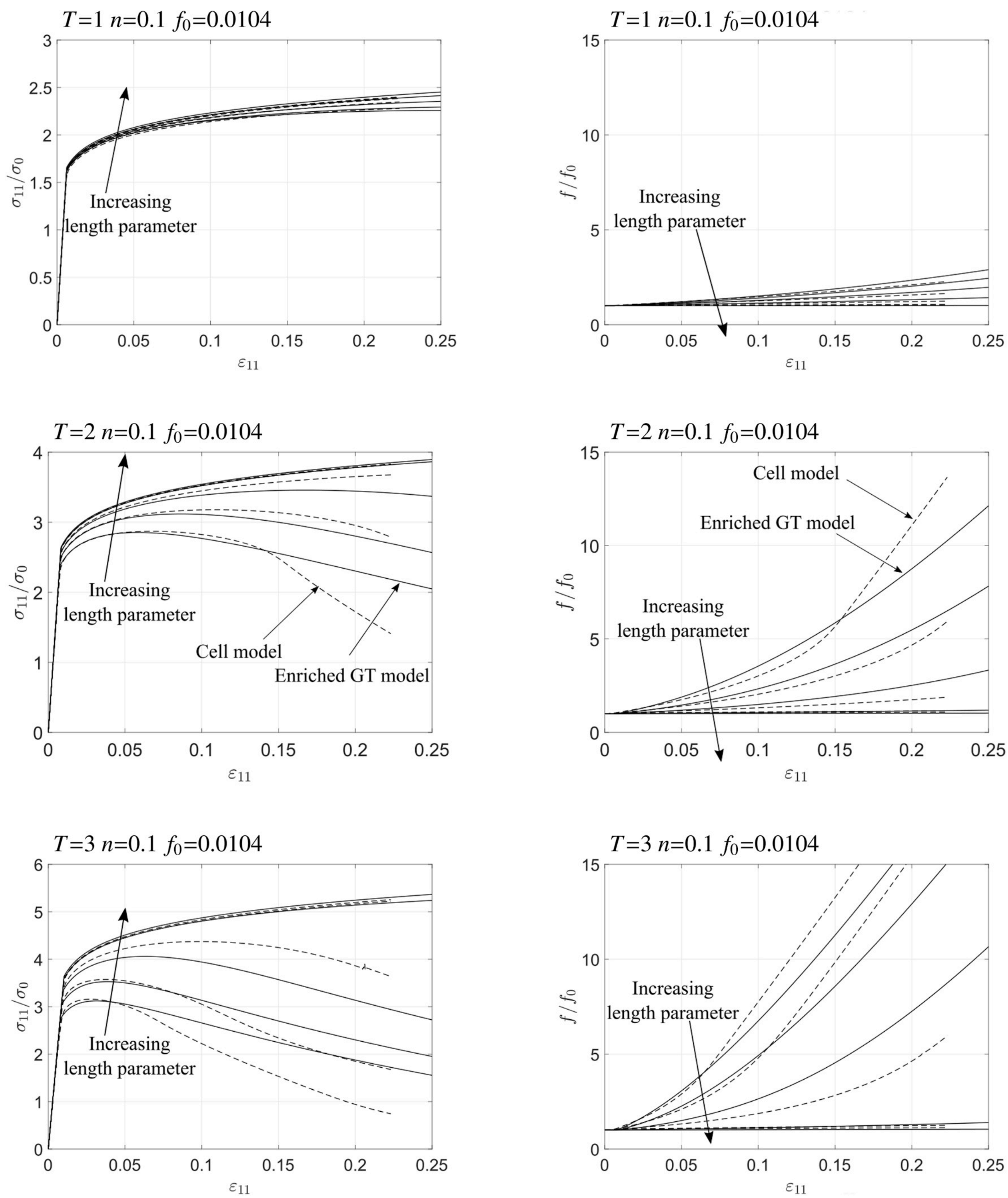

Fig. 2. Finite element results for $f_0 = 0.0104$ and $n = 0.1$ with stress triaxialities $T = 1$, 2 and 3 (from the top down.) The left column shows the macroscopic true axial stress-logarithmic axial strain response. The logarithmic strain is given as $\varepsilon_{11} = \ln(1 + e_{11})$, where e_{11} is the engineering strain. The right column shows the void volume fraction as function of logarithmic axial strain. The solid lines are the results for the enriched Gurson model, and the cell model results are displayed through the dashed lines. The five length parameters are $\frac{L_D}{R_c} = 0$, 0.05, 0.1, 0.25 and 0.5.

develop with the cubic root of the inverse void volume fraction as follows:

$$\frac{L_D}{R_V} = \frac{L_D}{R_0}\left(\frac{f_0}{f}\right)^{1/3}. \tag{18}$$

Here, the intrinsic length parameter is L_D, R_0 is the initial void radius corresponding to the initial void volume fraction, f_0, and R_v is the current void radius corresponding to a current void volume fraction, f, assuming spherical voids. Eq. (18) shows how the current void radius, R_V, relates to the void growth. It should be noted that for $L_D = 0$, the prefactors (Q_1 and Q_2) become one and the yield condition reduces to that of Gurson (1977) modified by Tvergaard (1981, 1982) through the Tvergaard-constants, here taken to be $q_1 = 1.5$ and $q_2 = 1$.

The incremental relationship between the microscopic equivalent plastic strain and the microscopic equivalent stress is $h_M = \mathrm{d}\sigma_M/\mathrm{d}\varepsilon_M^P$, with microscopic equivalent plastic strain, ε_M^P, in the matrix varying according to the equivalent plastic work expression

$$\sigma_{ij}\dot{\varepsilon}_{ij}^P = (1 - f)\sigma_M\dot{\varepsilon}_M^P. \tag{19}$$

Combining the plastic work expression and the incremental relationship between microscopic stress and strain, gives the following expression for $\dot{\sigma}_M$

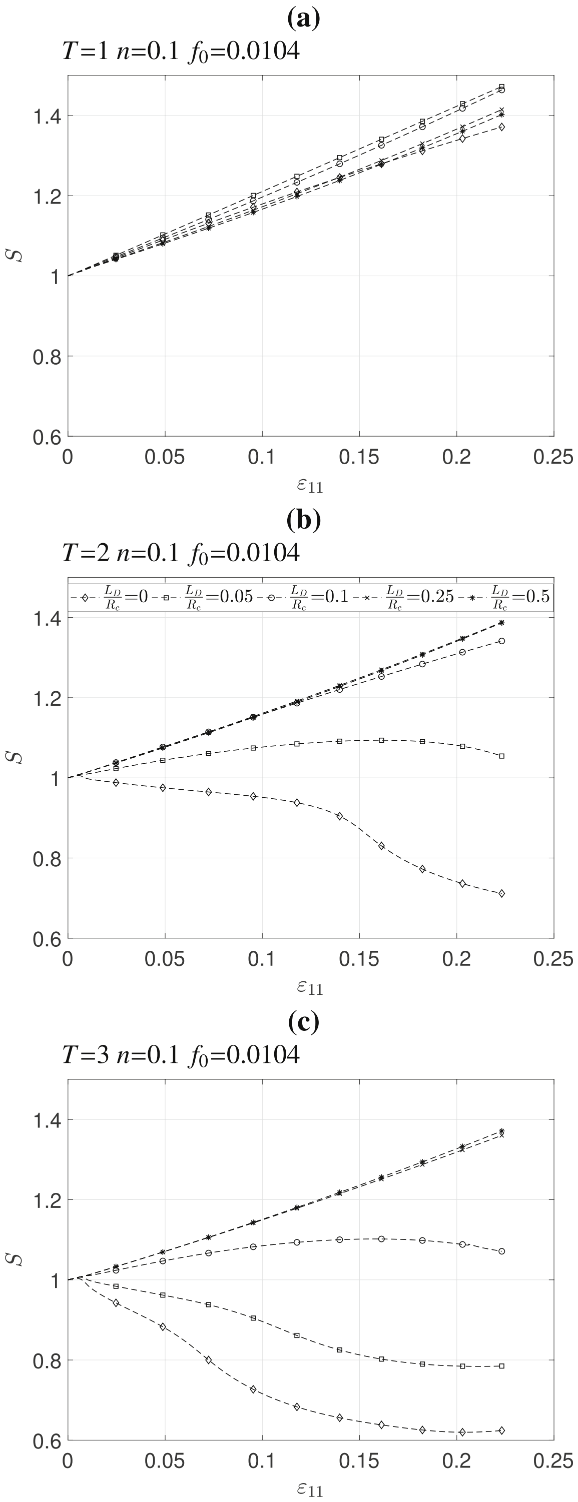

Fig. 3. Aspect ratio of the void as function of logarithmic axial strain for $f_0 = 0.0104$ and $n = 0.1$ with stress triaxialites: (a) $T = 1$, (b) $T = 2$ and (c) $T = 3$.

$$\dot{\sigma}_M = h_M \frac{\sigma_{ij}\dot{\varepsilon}_{ij}^P}{(1-f)\sigma_M}. \tag{20}$$

The matrix material satisfies the plastic incompressibility condition. However, the presence and growth of voids are associated with volume changes, thus the trace of the plastic deformation rate becomes non-zero. In this work, neither void nucleation nor coalescence is considered and the porosity growth rate is taken only to be dependent on the plastic deformation rate through

$$\dot{f} = (1-f)\dot{\varepsilon}_{kk}^P. \tag{21}$$

Following Bishop and Hill (1951) and Gurson (1977) normality locally within the matrix implies macroscopic normality. Thus, the plastic strain rate tensor must be normal to the yield surface according to

$$\dot{\varepsilon}_{ij}^P = \Lambda \frac{\partial \Phi}{\partial \sigma_{ij}}. \tag{22}$$

The plastic multiplier, Λ, is determined by substituting Eqs. (20) and (21) into the consistency condition during plastic straining. The current void radius is a function of f, hence evolution of the parameters Q_1 and Q_2 must be accounted for in the consistency condition, which then reads $\dot{\Phi}(\sigma_{ij}, \sigma_M, f, Q_1, Q_2) = 0$, with $\dot{Q}_1$ and $\dot{Q}_2$ being functions of f. By solving for Λ, Eq. (22) can be written as

$$\dot{\varepsilon}_{ij}^P = \frac{1}{H} n_{ij} n_{kl} \dot{\sigma}_{kl}, \quad \text{with} \quad n_{ij} = \frac{3}{2}\frac{s_{ij}}{\sigma_M} + \alpha\delta_{ij}, \tag{23}$$

where H is given by

$$H = \frac{h_M}{(1-f)}\left(\omega + \alpha\frac{\sigma_{kk}}{\sigma_M}\right)^2 - 3\sigma_M(1-f)\alpha\left[\gamma\left(1 + \frac{f}{Q_1 q_1}\frac{\partial Q_1}{\partial f}\right) + \frac{\alpha}{Q_2 q_2}\frac{\sigma_{kk}}{\sigma_M}\frac{\partial Q_2}{\partial f}\right] \tag{24}$$

$$\alpha = \frac{1}{2} Q_1 q_1 Q_2 q_2 f \sinh\left(\frac{Q_2 q_2}{2}\frac{\sigma_{kk}}{\sigma_M}\right) \tag{25}$$

$$\gamma = Q_1 q_1 \cosh\left(\frac{Q_2 q_2}{2}\frac{\sigma_{kk}}{\sigma_M}\right) - (Q_1 q_1)^2 f \tag{26}$$

$$\omega = \frac{\sigma_e^2}{\sigma_M^2} \tag{27}$$

The total strain increment is given by $\dot{\varepsilon}_{ij} = \dot{\varepsilon}_{ij}^E + \dot{\varepsilon}_{ij}^P$, with the elastic rate of deformation taken to be

$$\dot{\varepsilon}_{ij}^E = \frac{1+\nu}{E}\overset{\triangledown}{\sigma}_{ij} - \frac{\nu}{E}\delta_{ij}\overset{\triangledown}{\sigma}_{kk} \tag{28}$$

with, $\overset{\triangledown}{\sigma}_{ij}$ denoting the Jaumann stress rate. For the single-point model, there is no distinction between the deformed and reference configuration which allows for the rigid body rotations to be omitted. The spin tensor is zero and the incremental Cauchy stress may therefore be used directly. Adding the elastic and plastic rate of deformation, and inverting, gives the following relation between the stress and strain increment

$$\dot{\sigma}_{ij} = \mathbb{L}_{ijkl}\dot{\varepsilon}_{ij} \tag{29}$$

with $\mathbb{L}_{ijkl}$

$$\mathbb{L}_{ijkl} = \mathscr{L}_{ijkl} - \mu M_{ij} M_{kl} \tag{30}$$

where $\mathscr{L}_{ijkl}$ is the elastic stiffness tensor. M_{ij} and μ are given by

$$M_{ij} = \mathscr{L}_{ijkl} n_{kl}, \qquad \mu = \frac{1}{H + \mathscr{L}_{ijkl} n_{ij} n_{kl}}. \tag{31}$$

It is important to note that the parameters Q_1 and Q_2 enter the hardening modulus in Eq. (24), and complicates the implementation of the enriched GT model. However, it will be discussed in Section 4.4 that the effect of omitting the variation of Q_1 and Q_2 with f is minor. The enriched GT model is solved with a forward Euler integration scheme.

4. Numerical results and discussion

Solutions based on the gradient enriched GT model are presented through a parametric study and compared to corresponding predictions

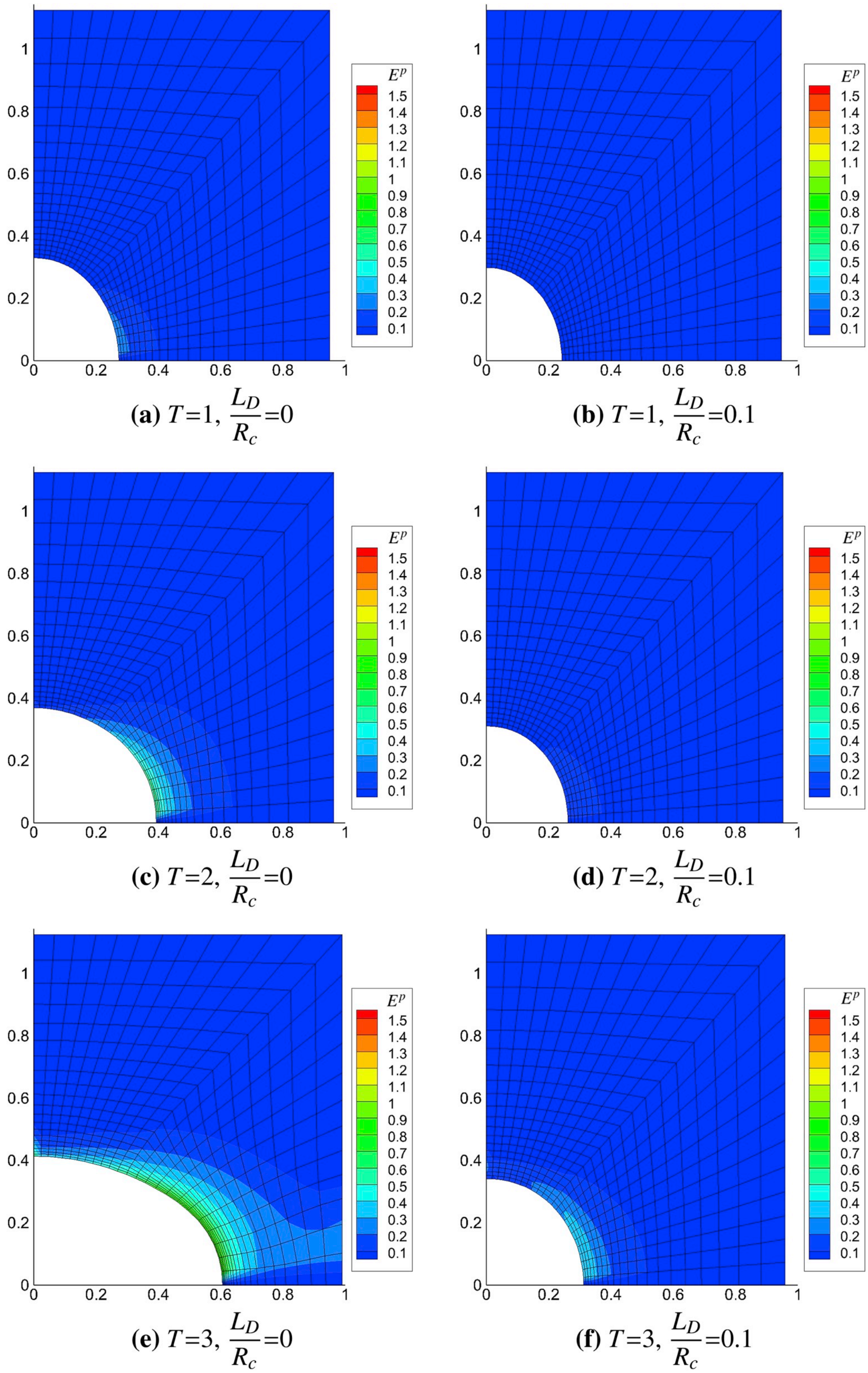

Fig. 4. Deformed meshes and contours of E^p for $f_0 = 0.0104$ and $n = 0.1$ at $\varepsilon_{11} = 0.118$ for three triaxialities, from top to bottom: $T = 1$, 2 and 3, at two measures of logarithmic axial strain. The left column shows results at $\frac{L_D}{R_c} = 0$ and the right column at $\frac{L_D}{R_c} = 0.1$. The initial radius, R_0, is 0.25.

from the unit cell model. Throughout the parameters $\sigma_y/E = 0.005$, $\nu = 0.3$ and $m = 0.01$ are used. The strain rate sensitivity parameter, m, enters the cell model only, and care has been taken that visco-plastic effects are very limited (see also 20). The enriched GT model is run with a step size of $\varepsilon_0/100$, where $\varepsilon_0 = \sigma_y/E$, to match the results from the Fleck and Willis governed cell model. The loading rate in the cell model is equal to the reference strain, ε_0. The influence of the stress state triaxiality, T, the matrix material strain hardening, n, and the initial void volume fraction, f_0 will be studied in this section. Finally, the effect of neglecting the effect of the derivatives of Q_1 and Q_2 in the consistency condition will be discussed.

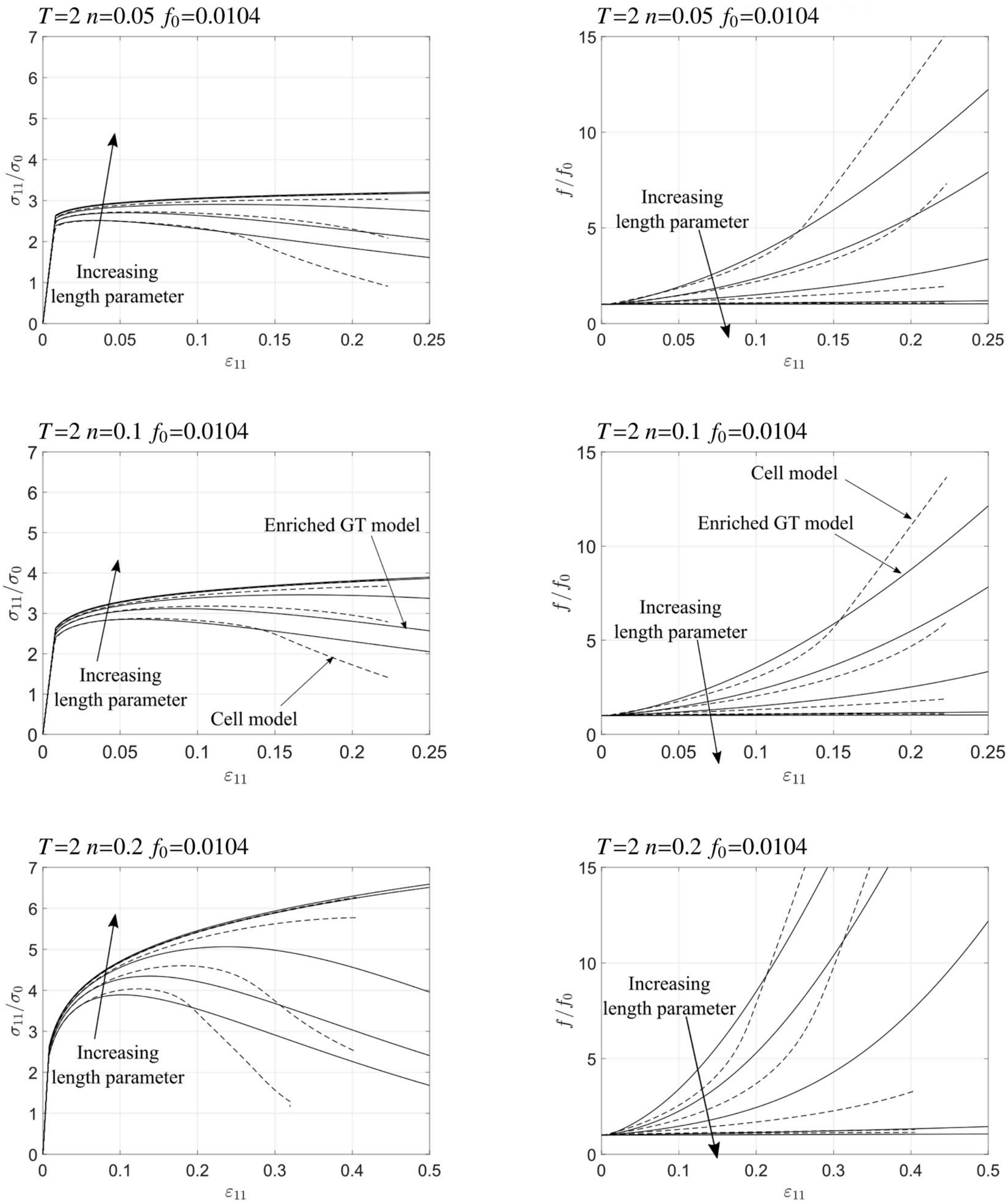

Fig. 5. Finite element results for $f_0 = 0.0104$ and $T = 2$ with hardening exponents $n = 0.05$, 0.1 and 0.2 (from the top down). The left column shows the macroscopic true axial stress-logarithmic axial strain response. The right column shows the void volume fraction as function of logarithmic axial strain. The solid lines are the results from the enriched Gurson model, and the cell model results are displayed through the dashed lines. The five length parameters are $\frac{L_D}{R_c} = 0$, 0.05, 0.1, 0.25 and 0.5.

4.1. Effect of triaxiality

To investigate the effect of stress triaxiality, the hardening exponent is kept constant at $n = 0.1$ and the initial void volume fraction at $f_0 = 0.0104$. The triaxialities investigated are $T = 1$, 2 and 3, which corresponds to ρ-values of 0.4, 0.625 and 0.727 (see Eq. (3)). The response curves and void growth curves for a conventional material are presented alongside results from simulations of materials with four different length parameters: $\frac{L_D}{R_c} = 0.05$, 0.1, 0.25 and 0.5 in Fig. 2. The conventional material is modelled with an intrinsic length parameter approaching zero. A small intrinsic length parameter corresponds to a microstructure where plastic gradient effects play little part such that the effective plastic strain in Eq. (9) equals the von Mises equivalent strain. In contrast, a larger intrinsic length parameter gives rise to greater gradient contributions. It should be noted that increasing the intrinsic length parameter corresponds to a material with smaller voids, but of the same initial void volume fraction (void are smaller and located closer together). The response curves show the true axial stress as a function of logarithmic axial strain, while the void growth curves show the relative void volume fraction as a function of logarithmic axial strain. It is seen that the gradient enriched GT model captures the increased gradient hardening reflected in all response curves, as well as predicts suppressed void growth with increasing length parameter seen for all void growth curves. For the lowest stress triaxiality considered ($T = 1$), the results from the enriched Gurson model fit well with the results from the cell model and only a small variation in gradient hardening is predicted. At this stress state, the stresses in axial direction are sufficiently large compared to those in the radial direction to

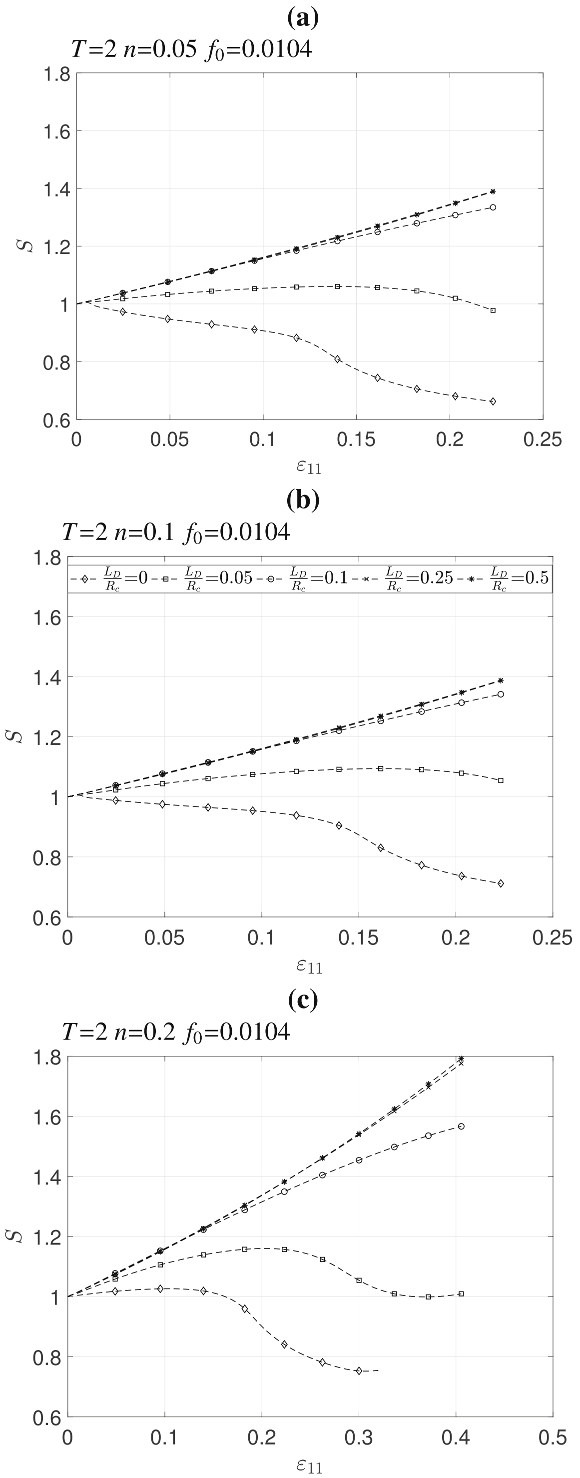

Fig. 6. Aspect ratio of the void as function of axial strain for $f_0 = 0.0104$ and $T = 2$ with different hardening exponents. (a) $n = 0.05$; (b) $n = 0.1$; (c) $n = 0.2$.

develop localisation in the intervoid ligaments, and the material will experience only strain and gradient hardening. Little void growth occurs for these simulations, and the voids are merely stretched along the main straining axis for the values of logarithmic axial strain presented here. The void shape evolution curves from the cell model simulations presented in Fig. 3 show the shape parameter, S, plotted against logarithmic axial strain (see Eq. (2)). Recall that for $S>1$ the void is prolate and for $S<1$ the void is oblate. Fig. 3a shows that the voids grow into a prolate shape for all the materials simulated under $T = 1$ loading conditions. At the state of deformation considered, the unit cell is not stretched sufficiently for localisation and material softening to occur.

For the higher triaxiality, $T = 2$, a greater effect of the gradients is predicted. The enriched Gurson model captures the yield point for all unit cell simulations. Moreover, materials with large intrinsic length parameters $\left(\frac{L_D}{R_c} = 0.25 \text{ and } 0.5\right)$, matches both the response curves and the void growth curves. For such large length parameters, the material does not soften nor does it experience significant void growth. The void shape curves in Fig. 3b prove that the voids grow to a prolate shape and the material behaviour resembles that of a conventional material under low stress triaxiality loading conditions. For the conventional material subject to $T = 2$, however, both material softening and extensive void growth occurs, and the gradient enriched GT model deviates from the cell model results at high axial strains. The void shape curve for $\frac{L_D}{R_c}\rightarrow 0$ in Fig. 3b shows that the void rapidly grows oblate at the axial strain where the material begins to soften. The oblate shape indicates that the void growth occurs in the radial direction and the voids deform towards coalescence. The enriched GT model will not capture this as it incorporates neither void shape changes nor a localisation criterion.

The response curves and void growth curves for the highest triaxiality, $T = 3$, are a continuation of the development found for $T = 2$. The conventional material undergoes localisation rapidly and the enriched GT model results deviate from those of the cell model. The materials with the two highest intrinsic length parameters $\left(\frac{L_D}{R_c} = 0.25 \text{ and } 0.5\right)$ also here exhibit the same behaviour as materials subject to low stress triaxiality loading, and neither significant void growth nor material softening will initiate at the deformation state considered. Fig. 3c shows that voids in a material with insufficient gradient hardening subject to a high stress triaxiality will grow oblate and soften the material through void coalescence.

Deformed meshes and contour plots of the gradient enhanced effective plastic strain, E^p, is shown in Fig. 4 as obtained by the cell model analyses. The results illustrate the limitations of the gradient enriched Gurson model. Fig. 4 presents results for both the conventional material and the gradient hardening material with intrinsic length parameter $\frac{L_D}{R_c} = 0.1$ for the three different stress triaxialities. It is seen that the voids are more prone to grow oblate at high triaxiality, which is in agreement with results from Koplik and Needleman (1988). Budiansky et al. (1982) studied void shape evolution for a linearly viscous material and found that the void equator lengthens more rapidly than the meridians for a void in a high triaxiality stress field. Gradient hardening, however, affects the void growth for micron scale voids and hence the void shape is affected. Fig. 4 shows the difference in void evolution for the conventional material and the material with intrinsic length parameter $\frac{L_D}{R_c} = 0.1$. The conventional material does not experience gradient hardening and significant void growth takes place. For the material with intrinsic length parameter $\frac{L_D}{R_c} = 0.1$, gradient hardening is sufficient to restrict void growth almost entirely. The void is stretched along the main straining axis and shortened along the equator, growing into a prolate shape. The unit cell is strained accordingly and the relative void volume fraction will therefore not change significantly. For $T = 3$, the void in the conventional material matrix grows to an oblate shape, while the void in the gradient hardening in the material with an intrinsic length parameter $\frac{L_D}{R_c} = 0.1$, becomes prolate.

4.2. Effect of the strain hardening exponent

Results for three values of the strain hardening exponent, n, are presented in the following: $n = 0.05$, 0.1 and 0.2. The stress triaxiality is kept constant at $T = 2$ and the initial void volume fraction constant at $f_0 = 0.0104$. The results for the conventional material, $\frac{L_D}{R_c}\rightarrow 0$, are presented alongside results from the same four length parameters as for the investigation of stress triaxiality presented in Section 4.1. The response

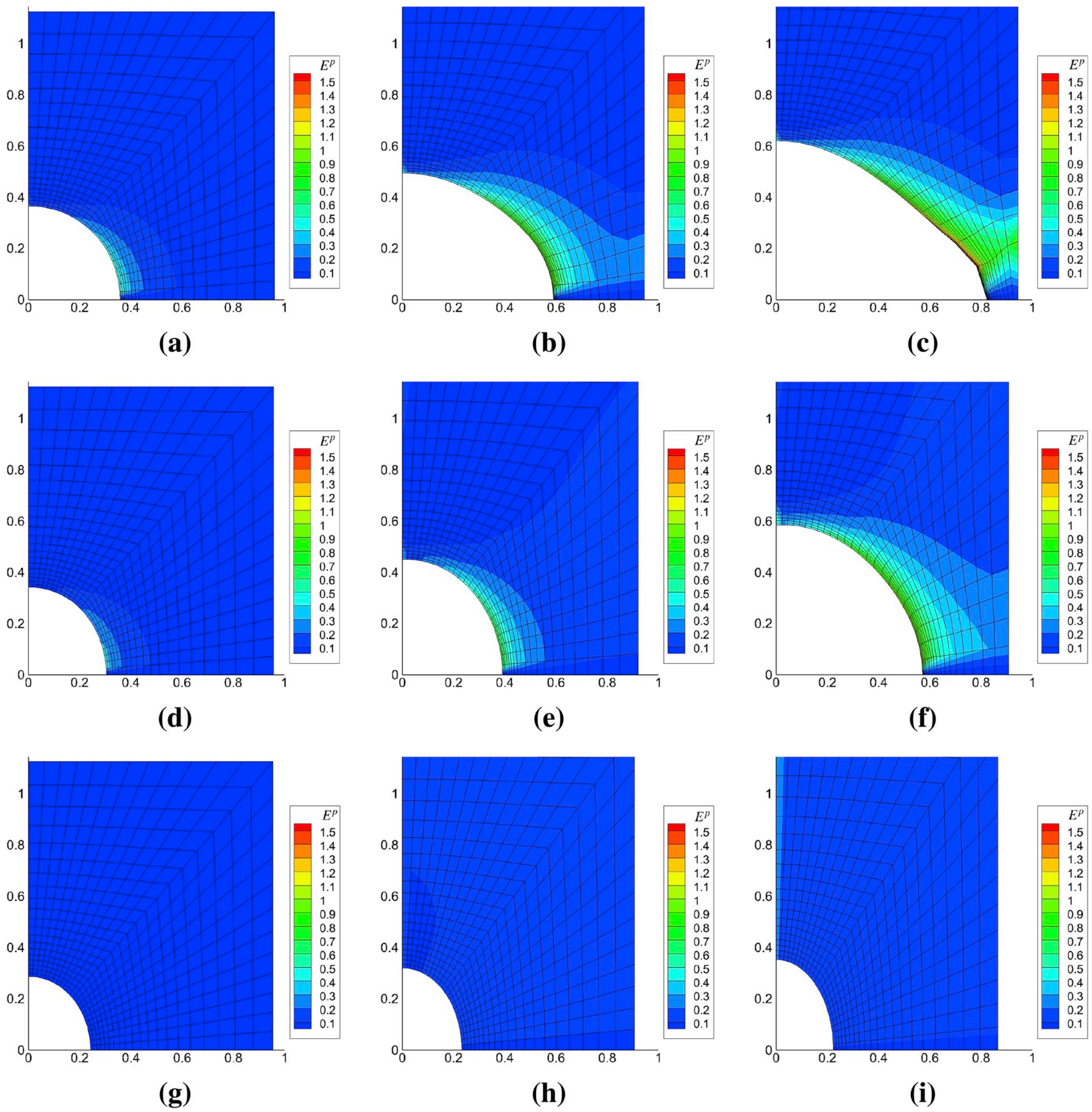

Fig. 7. Deformed meshes and contours of E^p for $f_0 = 0.0104$, $T = 2$ and $n = 0.2$ for three different intrinsic length parameters. The top row shows results for $\frac{L_D}{R_c} \to 0$, the middle row for $\frac{L_D}{R_c} = 0.05$ and the last row for $\frac{L_D}{R_c} = 0.5$. The columns represent axial strain of, from left to right: $\varepsilon_{11} = 0.118$, 0.223 and 0.318.

curves and void growth curves are given in Fig. 5, while the void shape curves are presented in Fig. 6. The same quantities as for the triaxiality results in Fig. 2 are plotted for consistency. The strain hardening exponent largely influences the peak of the response curves, and the results for the different values of n can therefore not be compared directly. The simulations for $n = 0.2$ are therefore taken to twice as large axial strain compared to the other simulations. The response curves in Fig. 5 show that the enriched Gurson model captures the yield point for all configurations of strain hardening and gradient hardening. The trend of a rising response curve with increasing hardening exponent is also captured. For $n = 0.05$, the strain hardening is small and the response curves only show little hardening. The spread in the curves is due to gradient hardening, which is seen to have a small effect for this low value of n. For materials with large intrinsic length parameters $\left(\frac{L_D}{R_c} = 0.25 \text{ and } 0.5\right)$ softening is not observed at the state of deformation considered. The void growth curves show that the relative void volume fraction is nearly constant throughout the simulations, while the void shape curves show that the voids become prolate (see Fig. 6a). The gradient effects are the same here as for the results from the triaxiality study. The response curve for the conventional material with $n = 0.05$ follow that of the cell model well until an abrupt change in load carrying capacity of the materials is observed. The logarithmic axial strain at localisation, i.e. the abrupt change in load bearing capacity, corresponds to the strain at which the void shape rapidly grows oblate in Fig. 6a.

Materials with the highest hardening exponent, $n = 0.2$, shows the greatest effect of the gradient hardening. The response curves and void growth curves have a larger spread when compared to those from simulations with $n = 0.05$ and 0.1. This indicates the synergy effect between strain hardening and gradient hardening related to Eq. (9). The materials that do not undergo sufficient gradient hardening to impede the void growth experience extensive hardening before a sudden and rapid material softening. This is not captured well by the enriched GT model, which suggest that the effect of gradient hardening on the void

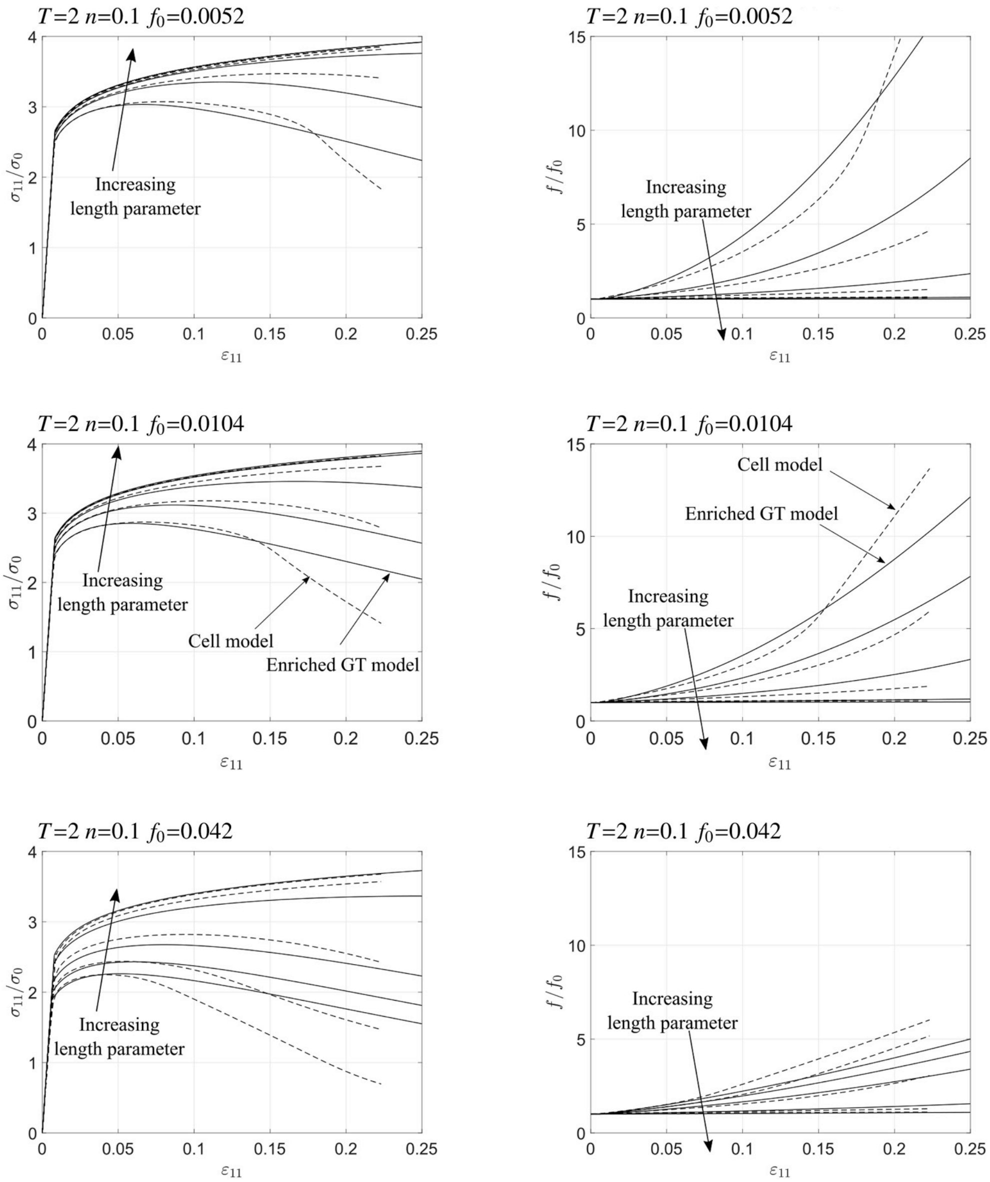

Fig. 8. Finite element results for $T = 2$ and $n = 0.1$ with initial void volume fraction $f_0 = 0.51\%$, 0.0104 and 0.042 (from the top down.) The left column shows the macroscopic true axial stress-logarithmic axial strain response. The right column shows the void volume fraction as function of logarithmic axial strain. The solid lines are the results from the enriched Gurson model, and the cell model results are displayed through the dashed lines. The five length parameters are $\frac{L_D}{R_c} = 0$, 0.05, 0.1, 0.25 and 0.5.

shape evolution is prominent. The void shape curves in Fig. 6c provide further insight on this. It is seen that voids in all the materials with $n = 0.2$ become prolate at low axial strains which indicates that the hardening in the material matrix is sufficient to delay excessive void growth in the radial direction. The conventional material experiences the least amount of hardening at lower deformation levels as compared to larger values of $\frac{L_D}{R_c}$. The other materials show increased hardening with increasing length parameter. High stresses are required to maintain plastic flow in a material with a large hardening exponent, and the localisation will be dramatic making the subsequent softening abrupt. The matrix material is carrying high stresses that will be released at the onset of localisation and the void will grow in the radial direction changing the shape. When comparing Fig. 5 for $n = 0.2$ and Fig. 6c for the conventional material and the material with the lowest length parameter, is it seen that the curves peak at the same value of logarithmic axial strain. Representing the effect of the voids through a single parameter, namely the void volume fraction, f, is not sufficient to capture these combined effects, and the enriched GT model will therefore not accurately represent both the response and void growth curves of the cell model. The materials with larger intrinsic length parameter and thereby increased gradient hardening will not undergo extensive void growth nor localisation and the gradient enriched Gurson model therefore captures both the response curves and the void growth curves well.

The effect of gradient hardening on the void evolution can be seen in Fig. 7 for the highest value of strain hardening. Deformed meshes and contour plots of E^p are depicted for both the conventional material and the materials with smallest and largest intrinsic material length parameters $\left(\frac{L_D}{R_c} = 0.05 \text{ and } 0.5\right)$ are presented for three different values of logarithmic axial strain. For the conventional material, localisation is seen to have initiated at an intermediate axial strain value, while severe deformation is predicted in the transverse void ligament at the highest

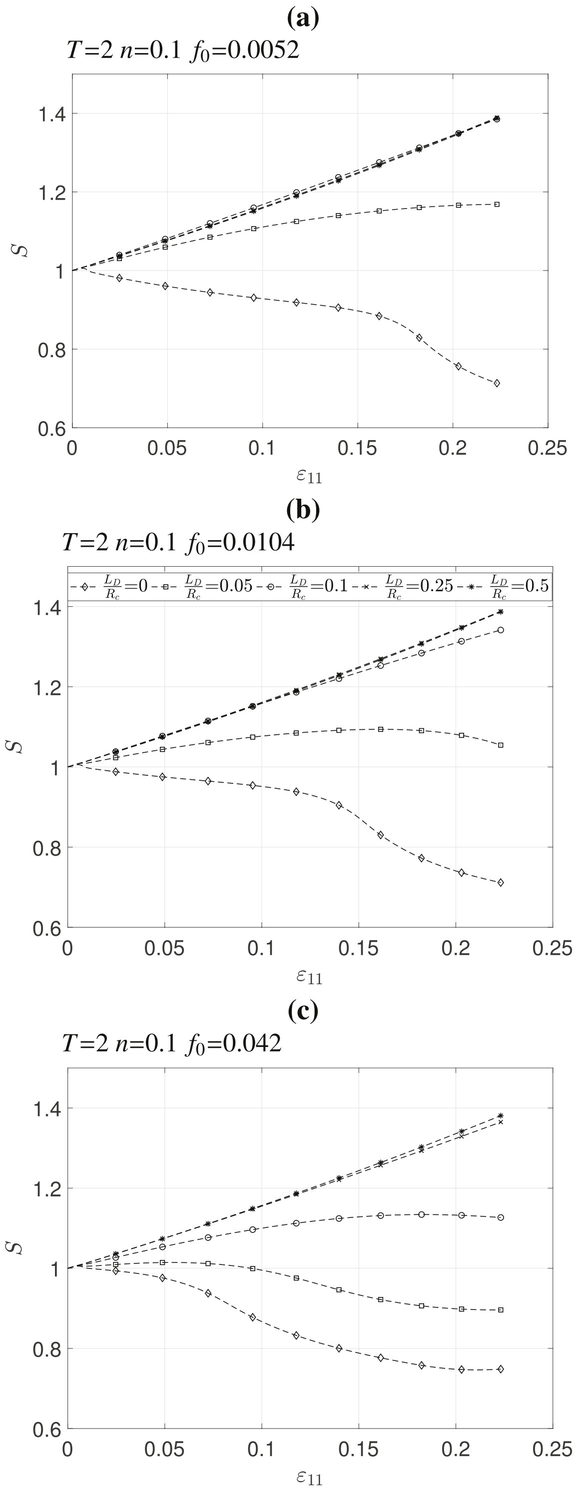

Fig. 9. Aspect ratio of void as function of axial strain for $T = 2$, $n = 0.1$ with different initial void volume fractions. (a) $f_0 = 0.0052$; (b) $f_0 = 0.0104$; (c) $f_0 = 0.042$.

value of axial strain. For the material with the lowest intrinsic length parameter, $\frac{L_D}{R_c} = 0.05$, the void is seen to develop in a more restrained manner. At the intermediate axial strain, the void has grown, but still has a prolate shape. For the largest axial strain, the void has returned to a spherical shape, indicating that the void growth occurs mainly in the transverse direction and that localisation has initiated. The material with the highest amount of gradient hardening exhibits only little void growth, but also stretching in conjunction with the unit cell itself.

4.3. Effect of the initial void volume fraction

Keeping the triaxiality constant at $T = 2$ and the hardening exponent at $n = 0.1$, the effect of the initial void volume fraction is investigated. Three initial porosities are considered: $f_0 = 0.0052$ 0.0104 and 0.042. For a square unit cell, given in Fig. 1b with $\frac{H_c}{R_c} = 1$, this corresponds to initial void radii: $R_v = 0.2$, 0.25 and 0.4, respectively. The response curves and void growth curves for the three f_0-values for a conventional material are presented in Fig. 8 together with four materials with length parameters. The void shape evolution is presented in Fig. 9.

The response curves in Fig. 8 show that increasing f_0 decreases the yield point, which corresponds well with results from Niordson and Tvergaard (2019). For the two materials with most gradient hardening, the material does not soften for either value of f_0 at the state of deformation considered. The void growth curves show that the relative void volume fraction is essentially constant through the simulation for the materials with intrinsic length parameters $\frac{L_D}{R_c} = 0.25$ and 0.5. This indicates that the effect of gradient hardening surpasses the effect of f_0. However, f_0 has an effect on both the response curves and the void growth curves for all materials considered independent of length parameter. For an initial void volume fraction of 0.0052, the conventional material undergoes localisation which is not captured by the enriched Gurson model. The void shape curve for this material shows that the void grows oblate at an accelerated speed at the value of axial strain corresponding to localisation in Fig. 8. Increasing f_0, gives a larger spread in the response curve yield point indicating that for large voids, gradient hardening has a more prominent effect on the material behaviour than softening.

The material response curves for the largest initial void volume fraction, $f_0 = 0.042$, exhibits a great dependence on the intrinsic length parameter. The conventional material along with the material with the smallest intrinsic length parameter, $\frac{L_D}{R_c} = 0.05$, both soften extensively. It is seen that the voids in the conventional material and the material with the smallest intrinsic length parameter grow to an oblate shape. The connection between oblate voids and material softening corresponds well with the results presented for both the investigation of triaxiality and the strain hardening exponent. It is discovered that increasing the initial void volume fraction leads to suppressed relative void growth rate. This seems to be contradictory to previous results, where material softening was an effect of an increasing void volume fraction due to void growth. Deformed meshes and the contours of E^p are presented in Fig. 10 for all three values of f_0 with $\frac{L_D}{R_c} = 0.05$ at two values of logarithmic axial strain. These meshes provide an explanation for the suppressed void growth with increasing initial void volume fraction. Although the growth for $f_0 = 0.042$ seems to be considerably more than for the other two values of f_0, the relative void evolution is not. The deformed meshes in Fig. 10 are from the material with the lowest intrinsic length parameter, which only undergoes localisation for the largest initial void volume fraction. The size of the discrete void makes the transverse ligament too small to sustain the loads. The plastic flow will localise, as shown in Fig. 10, while the void is stretched in conjunction with the unit cell, making the void volume fraction nearly constant while the material softens. Increasing the gradient hardening will suppress this effect such that the material will not undergo localisation.

4.4. Approximation of the consistency condition for the enriched Gurson model

For all previous figures, the full effect of Eq. (24) has been accounted for. The effect of neglecting $\dot{Q}_1$ and $\dot{Q}_2$ is investigated in the following by running simulations with an approximation of the consistency condition where $\dot{Q}_1$ and $\dot{Q}_2$ are omitted. The results are presented in Fig. 11 for simulations with $T = 2$, $n = 0.1$ and $f_0 = 0.0104$.

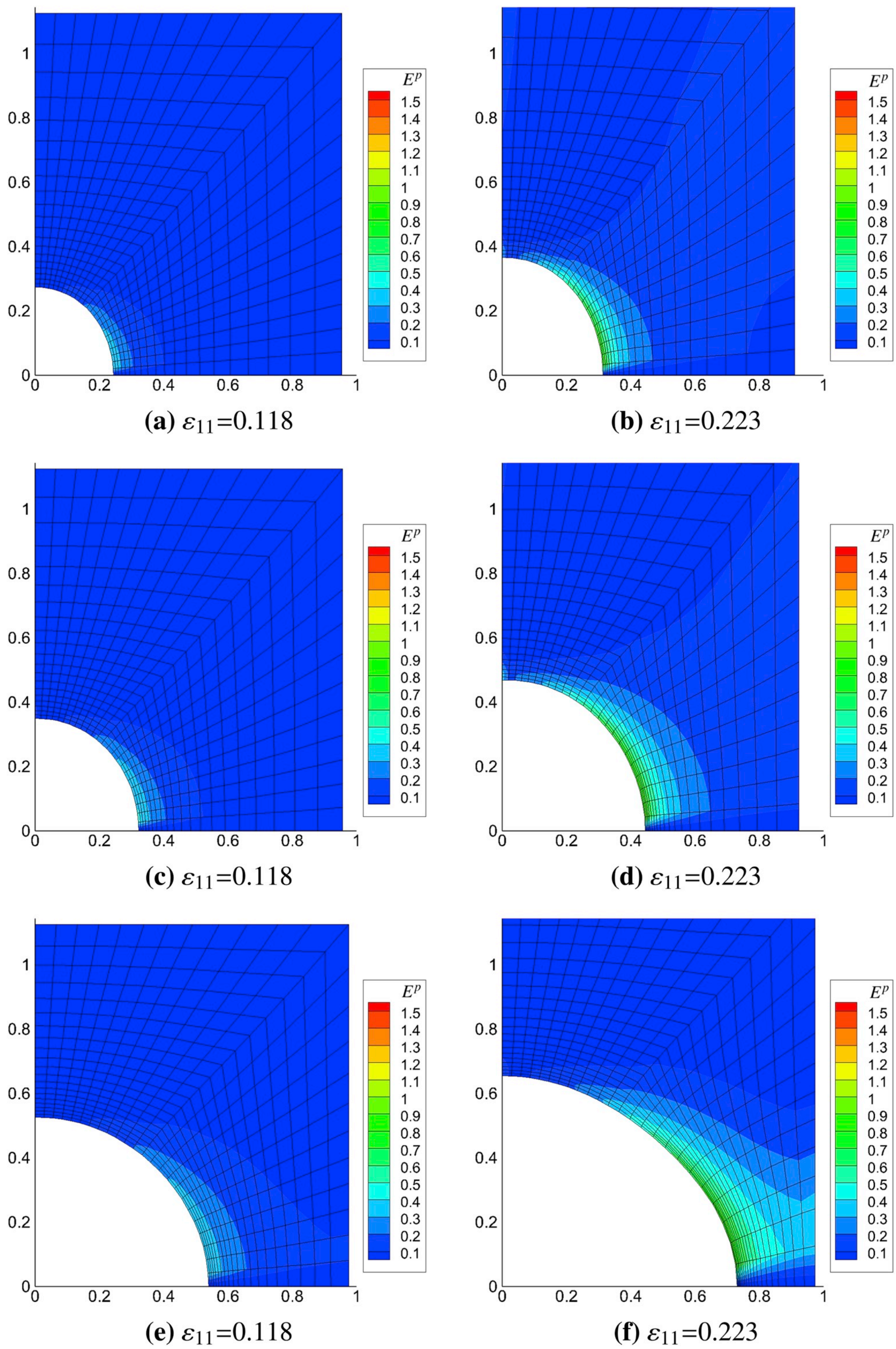

Fig. 10. Deformed meshes and contours of E^p for n = 0.1, T = 2 and $\frac{L_D}{R_c}$ = 0.05 for three different initial void volume fractions at two different measures of logarithmic axial strain: (a–b) f_0 = 0.0052 (R_0 = 0.2); (c–d) f_0 = 0.0104 (R_0 = 0.25); (e–f) f_0 = 0.042 (R_0 = 0.4).

The increment size is $\varepsilon_0/100$, where $\varepsilon_0 = \sigma_y/E$. As must be expected, an increasing discrepancy between results for increasing length parameters is seen. Essentially, the hardening modulus, H, from Eq. (24), exhibits the largest difference with and without accounting for $\dot{Q}_1$ and $\dot{Q}_2$ when L_D increases until the length parameter becomes large enough for the results to fall on top of each other. For $\frac{L_D}{R_c}\rightarrow 0$, the results will coincide as the gradient effects are small and the material approaches that of the conventional Gurson-Tvergaard model, which does not incorporate a length parameter. Q_1 and Q_2 will approach unity and the response curves in Fig. 11 will fall on top of each other for materials with length parameters approaching zero. For large length parameters, i.e. small void sizes, both Q_1 and Q_2 will approach the lower bound value, and $\dot{Q}_1$ and $\dot{Q}_2$ will approach zero, according to the analyses by Niordson and Tvergaard (2019). For $\frac{L_D}{R_c}$ = 0.25 and above, $\dot{Q}_1$ and $\dot{Q}_2$ have been found to have a negligible effect on the material response.

We conclude that all though the rigorous inclusion of the derivatives

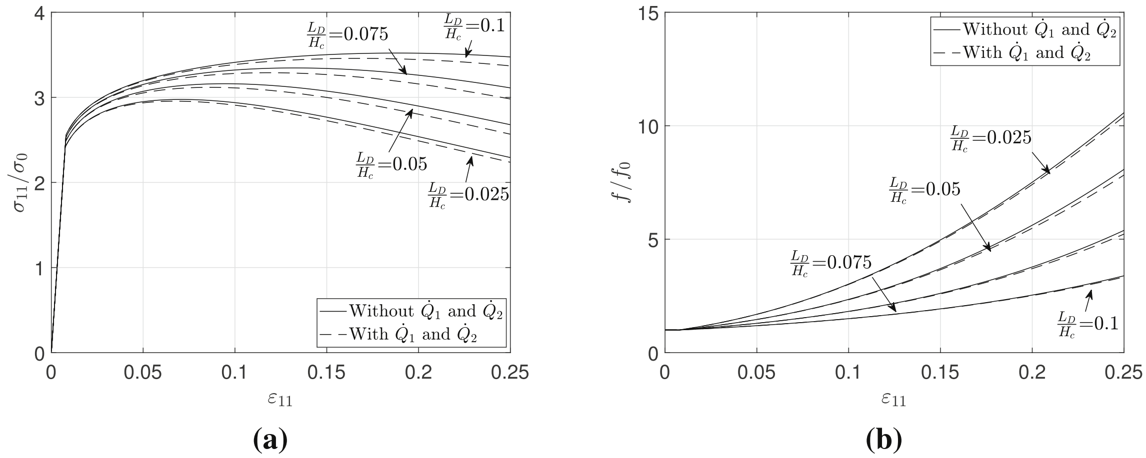

Fig. 11. Response curves (a) and void evolution (b) for four different length parameters. The solid lines are results for the enriched Gurson model without $\dot{Q}_1$ and $\dot{Q}_2$. The dashed lines show results for the enriched Gurson model with $\dot{Q}_1$ and $\dot{Q}_2$ accounted for in the consistency condition. $T = 2$, $n = 0.1$ and $f_0 = 0.0104$.

of Q_1 and Q_2 in the yield condition is needed for a self-consistent framework, the simpler framework where they are neglected provides a reasonable approximation, that could potentially be simpler to implement in existing computational frameworks for porous metal plasticity.

5. Conclusion

The present work has investigated a gradient enriched strain hardening Gurson-Tvergaard model incorporating an intrinsic length parameter tied to the void size in a ductile material model, as proposed by Niordson and Tvergaard (2019). The length scale parameter enters the constitutive equations through prefactors of the usual q_1 and q_2 parameters. The enriched GT model was modelled as a single point representing a porous continuum. A cell model incorporating a discrete void in a strain gradient plasticity governed matrix was used as benchmark for the simulation. A parametric study of stress triaxiality, strain hardening exponent and initial void volume fraction has been carried out. Three values of all the parameters in the study have been investigated for five values of the intrinsic length parameter. The enriched Gurson model is found to capture the elevated yield point and suppressed void growth with increasing gradient hardening for all parameters investigated. The length parameter influenced the void shape evolution, which is not captured by the enriched Gurson model as the voids are accounted for solely through the damage parameter f, the void volume fraction. Void shape was found significant for the material response as the region between the voids perpendicular to the main straining axis is of greater importance than the void volume itself, i.e. oblate voids can withstand less axial stress than prolate voids due to the size of the intervoid ligaments. A material with sufficient gradient hardening will not be affected by such effects as the gradients inhibit void evolution and thereby localisation, overall softening and coalescence.

Acknowledgement

This research was financially supported by Danish Council for Independent Research through the research project ”Advanced Damage Models with InTrinsic Size Effects” (Grant no: DFF-7017-00121).

References

Ashby, M., 1970. The deformation of plastically non-homogeneous materials. Phil. Mag. 21 (170), 399–424. https://doi.org/10.1080/14786437008238426.

Bishop, J., Hill, R., 1951. A theory of the plastic distortion of a polycrystalline aggregate under combined stresses. In: The London, Edinburgh, and Dublin Philosophical Magazine and Journal of Science, vol. 42. pp. 414–427. https://doi.org/10.1080/14786445108561065. (327).

Budiansky, B., Hutchinson, J., Slutsky, S., 1982. Void growth and collapse in viscous solids. In: Mechanics of Solids: the Rodney Hill 60th Anniversary Volume. Elsevier, pp. 13–45. https://doi.org/10.1016/B978-0-08-025443-2.50009-4.

Dormieux, L., Kondo, D., 2010. An extension of gurson model incorporating interface stresses effects. Int. J. Eng. Sci. 48 (6), 575–581. https://doi.org/10.1016/j.ijengsci.2010.01.004.

Fleck, N., Muller, G., Ashby, M., Hutchinson, J., 1994. Strain gradient plasticity: theory and experiment. Acta Metall. Mater. 42 (2), 475–487. https://doi.org/10.1016/0956-7151(94)90502-9.

Fleck, N.A., Hutchinson, J.W., 1997. Strain gradient plasticity. Adv. Appl. Mech. 33, 296–361.

Fleck, N.A., Willis, J.R., 2009. A mathematical basis for strain-gradient plasticity theory: Part II: tensorial plastic multiplier. J. Mech. Phys. Solids 57 (7), 1045–1057. https://doi.org/10.1016/j.jmps.2009.03.007.

Gao, H., Huang, Y., 2001. Taylor-based nonlocal theory of plasticity. Int. J. Solids Struct. 38 (15), 2615–2637. https://doi.org/10.1016/S0020-7683(00)00173-6.

Gudmundson, P., 2004. A unified treatment of strain gradient plasticity. J. Mech. Phys. Solids 52 (6), 1379–1406. https://doi.org/10.1016/j.jmps.2003.11.002.

Gurson, A.L., 1977. Continuum theory of ductile rupture by void nucleation and growth. part I: yield criteria and flow rules for porous ductile media. J. Eng. Mater. Technol. 99 (1), 2–15. https://doi.org/10.1115/1.3443401.

Koplik, J., Needleman, A., 1988. Void growth and coalescence in porous plastic solids. Int. J. Solids Struct. 24 (8), 835–853. https://doi.org/10.1016/0020-7683(88)90051-0.

Ma, Q., Clarke, D.R., 1995. Size dependent hardness of silver single crystals. J. Mater. Res. 10 (4), 853–863. https://doi.org/10.1557/JMR.1995.0853.

McMeeking, R., Rice, J.R., 1975. Finite-element formulations for problems of large elastic-plastic deformation. Int. J. Solids Struct. 11 (5), 601–616. https://doi.org/10.1016/0020-7683(75) 90033–5.

Monchiet, V., Bonnet, G., 2013. A gurson-type model accounting for void size effects. Int. J. Solids Struct. 50 (2), 320–327. https://doi.org/10.1016/j.ijsolstr.2012.09.005.

Monchiet, V., Kondo, D., 2013. Combined voids size and shape effects on the macroscopic criterion of ductile nanoporous materials. Int. J. Plast. 43, 20–41. https://doi.org/10.1016/j.ijplas.2012.10.007.

Nielsen, K.L., Niordson, C.F., 2013. A 2d finite element implementation of the fleck–willis strain-gradient flow theory. Eur. J. Mech. A Solid. 41, 134–142. https://doi.org/10.1016/j.euromechsol.2013.03.002.

Nielsen, K.L., Niordson, C.F., 2014. A numerical basis for strain-gradient plasticity theory: rate-independent and rate-dependent formulations. J. Mech. Phys. Solids 63, 113–127. https://doi.org/10.1016/j.jmps.2013.09.018.

Niordson, C.F., Tvergaard, V., 2019. A homogenized model for size-effects in porous metals. J. Mech. Phys. Solids 123, 222–233. https://doi.org/10.1016/j.jmps.2018.09.004.

Stelmashenko, N., Walls, M., Brown, L., Milman, Y.V., 1993. Microindentations on W and Mo oriented single crystals: an STM study. Acta Metall. Mater. 41 (10), 2855–2865. https://doi.org/10.1016/0956-7151(93)90100-7.

Stölken, J.S., Evans, A., 1998. A microbend test method for measuring the plasticity length scale. Acta Mater. 46 (14), 5109–5115. https://doi.org/10.1016/S1359-6454(98)00153-0.

Tvergaard, V., 1981. Influence of voids on shear band instabilities under plane strain conditions. Int. J. Fract. 17 (4), 389–407. https://doi.org/10.1007/BF00036191.

Tvergaard, V., 1982. Ductile fracture by cavity nucleation between larger voids. J. Mech. Phys. Solids 30 (4), 265–286. https://doi.org/10.1016/0022-5096(82)90033-3.

Wen, J., Huang, Y., Hwang, K., Liu, C., Li, M., 2005. The modified gurson model accounting for the void size effect. Int. J. Plast. 21 (2), 381–395. https://doi.org/10.1016/j.ijplas.2004.01.004.

[P2]

Interaction of void spacings and material size effect on inter-void flow localisation

Ingrid Holte, Ankit Srivastava, Emilio Martìnez-Pañeda, Christian F. Niordson, Kim L. Nielsen

Published in *Journal of Applied Mechanics*, **88**(2), xxx–xxx, 2020

Interaction of void spacing and material size effect on inter-void flow localisation

Ingrid Holte
Department of Mechanical Engineering
Technical University of Denmark, Kgs. Lyngby, Denmark
E-mail: inghol@mek.dtu.dk

Ankit Srivastava
Department of Materials Science and Engineering
Texas A&M University, College Station Texas, USA
E-mail: ankit.sri@tamu.edu

Emilio Martínez-Pañeda
Department of Civil and Environmental Engineering
Imperial College, London, UK
E-mail: e.martinez-paneda@imperial.ac.uk

Christian F. Niordson[1], **Kim L. Nielsen**[2]
Department of Mechanical Engineering
Technical University of Denmark, Kgs. Lyngby, Denmark
[1]E-mail: cn@mek.dtu.dk
[2]E-mail: kin@mek.dtu.dk

The ductile fracture process in porous metals due to growth and coalescence of micron scale voids is not only affected by the imposed stress state but also by the distribution of the voids and the material size effect. The objective of this work is to understand the interaction of the inter-void spacing (or ligaments) and the resultant gradient induced material size effect on void coalescence for a range of imposed stress states. To this end, three dimensional finite element calculations of unit cell models with a discrete void embedded in a strain gradient enhanced material matrix are performed. The calculations are carried out for a range of initial inter-void ligament sizes and imposed stress states characterised by fixed values of the stress triaxiality and the Lode parameter. Our results show that in the absence of strain gradient effects on the material response, decreasing the inter-void ligament size results in an increase in the propensity for void coalescence. However, in a strain gradient enhanced material matrix, the strain gradients harden the material in the inter-void ligament and decrease the effect of inter-void ligament size on the propensity for void coalescence.

1 Introduction

In porous metals, void coalescence often drives the onset of the macroscopic flow localisation that marks the end of uniform deformation and acts as a precursor to failure, as well as the initiation and propagation of ductile cracks [1–3]. Previous studies suggest that for conventional plasticity theory, where no material length scale enters the constitutive law (absence of stress/strain gradient induced size effect), a decrease in the inter-void spacing promotes void coalescence [4, 5] and results in the collapse of the yield surface [6, 7]. While for a fixed inter-void spacing, it is well established that the imposed stress state has a pronounced effect on the onset of void coalescence in conventional plasticity theory. For example, it has been shown that an increase in the imposed stress triaxiality (a ratio of the first to second stress invariant) promotes void growth and early onset of void coalescence [8–11]. Void coalescence is simply the event where the plastic flow localises within the inter-void ligaments and successively links the neighboring voids [9]. The plastic flow localisation within the inter-void ligament, however, will induce plastic strain gradients that in turn may affect the strengthening and hardening of the material. This raises a fundamental question: how does the interaction of inter-void spacing (or ligament size) and the gradient induced material size effect, affect the localisation of plastic flow causing void coalescence for a given stress state?

The gradient induced size effect resulting in strengthening and hardening in metals has been confirmed in many material tests involving non-uniform deformation including indentation [12, 13], torsion [14], and bending [15]. The size dependent material response on the micron scale in metal plasticity implies that the growth of micron sized voids also exhibits significant size effects [16, 17]. In general, it has been shown that the gradient induced size effect leads to slower growth rates for smaller voids [18–22]. An accurate representation of void coalescence due to plastic flow localisation within micron sized inter-void ligaments, therefore, also requires material models that represent stresses over the relevant length scales. Phenomenological theories describing the strengthening and hardening due to plastic strain gradients express the plastic work in terms of both plastic strain and plastic strain gradient, thereby introducing a length scale into the material model. Herein, the strain gradient plasticity theory proposed by Gudmundson [23] is used, which includes both dissipative (non-recoverable) and energetic (recoverable) gradient contributions within a small strain formulation based on visco-plasticity. The mathematical formulation and associated variational structure originate from Fleck and Willis [24], and the material model is implemented into the commercial finite element software ABAQUS using a user element (UEL) subroutine [25].

The objective of this work is to understand the interaction of the inter-void spacing (or ligament size) and the resultant gradient induced material size effect on void coalescence for a range of imposed stress states. To achieve this, three dimensional finite element unit cell calculations for a periodic array of initially spherical voids embedded in a strain gradient enhanced material matrix are carried out. Several unit cell geometries have been analyzed to investigate the effect of inter-void ligament size under multiple loading conditions. The imposed stress states are characterised by fixed values of the stress triaxiality and the Lode parameter (a measure of the third stress invariant). The value of the Lode parameter is shown to affect the evolution of voids in computations involving conventional plasticity theory [5, 26–29] and in experiments [30–32] only at relatively low stress triaxiality levels. However, it is likely that in an anisotropic material matrix [33] with anisotropy introduced by the void distribution [5], as for the present investigation, the effect of the Lode parameter can be important even at high stress triaxialities.

Our results show that for a conventional material matrix, increasing the inter-void ligament size results in an increase in the critical stress to void coalescence, up to a threshold value of inter-void ligament size. The sensitivity of the critical stress to the inter-void ligament size is found to increase with increasing stress triaxiality. The quantitative effect of the Lode parameter is found to be small for the stress triaxiality values varying from 1 to 3. However, for inter-void ligament sizes below the threshold value, the critical stress is smallest for a Lode parameter value of -1, whereas above the threshold value the critical stress is smallest for a Lode parameter value of 0. For a void in a strain gradient enhanced material matrix, the value of the critical stress for void coalescence increases with increasing length parameter i.e. increasing gradient effect. This effect of the length parameter on the critical stress magnitude is found to increase with increasing imposed stress triaxiality and decreasing inter-void ligament size. This is because at higher stress triaxiality values and for smaller inter-void ligament sizes, there is an increase in the propensity for plastic flow localisation that introduces strong plastic strain gradients and in turn hardens the ligament. This mechanism leads to a decrease in the dependence of critical stress on the inter-void ligament size with increasing length parameter. The gradient induced strengthening also tends to homogenize the deformation in the unit cell thus decreasing the effect of the Lode parameter.

The structure of the manuscript is as follows. Section 2 frames the study and presents the numerical method. The unit cell geometries considered, the method utilized to impose proportional loading throughout the deformation history, and the strain gradient plasticity material model are also presented in Section 2. The numerical results are presented and discussed in Section 3. Finally, the key results and conclusions of this work are summarized in Section 4.

2 Problem formulation and modelling approach

This work considers a limit load-type analysis to determine the critical stress level at which a given microstructure configuration loses load carrying capacity. Hence, an elastic-perfectly plastic material model is employed. The configuration of the unit cell and the simulation setup is described in Section 2.1, while the approach to prescribe a constant value of stress triaxiality and Lode parameter is outlined in Section 2.2.

2.1 Unit cell geometry and FE mesh

Three dimensional finite element calculations are carried out to model the response of an array of spherical voids with initial radius r_0, Fig. 1. The unit cell has edge lengths $2a_i^0$ along the three coordinate axes, x_i $(i = 1, 2, 3)$, and inter-void spacings thereby equal $2l_i^0 = 2a_i^0 - 2r_0$. Symmetry about three planes perpendicular to the coordinate axes implies that only $1/8$ of the unit cell needs to be modelled.

For all unit cells considered, the initial void volume fraction is $f_0 = 0.01$, where $f_0 = (4/3\pi r_0^3)/(8a_1^0 a_2^0 a_3^0)$. The initial void radius, r_0, is kept constant, while the cell dimensions are varied to achieve various initial inter-

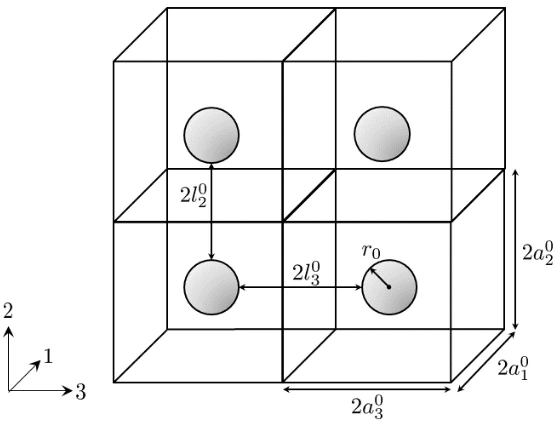

Fig. 1: Schematic showing the periodic arrangement of voids in the x_2- and x_3-plane. The distribution along the x_1-direction is not shown for simplicity.

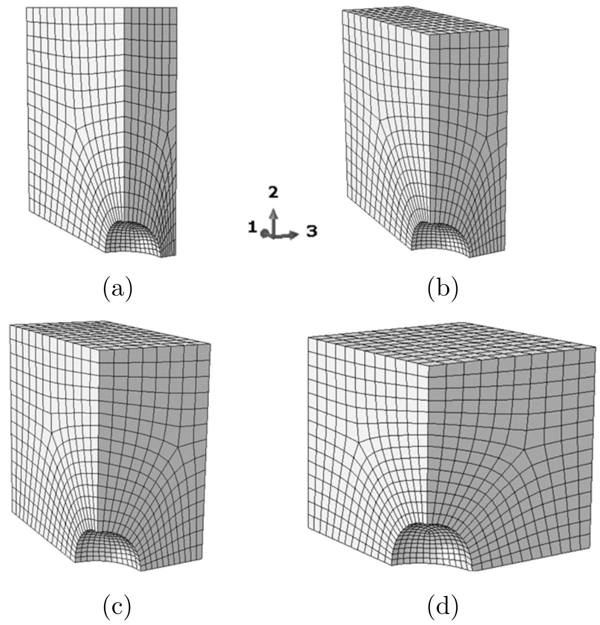

Fig. 2: Finite element meshes showing 1/8 of the unit cell with an initially spherical void of radius r_0 in the centre giving an initial void volume fraction of $f_0 = 0.01$ for (a) $l_1^0/r_0 = l_2^0/r_0 = 5.06$; $l_3^0/r_0 = 0.43$, (b) $l_1^0/r_0 = l_2^0/r_0 = 4.21$; $l_3^0/r_0 = 0.95$, (c) $l_1^0/r_0 = l_2^0/r_0 = 3.58$; $l_3^0/r_0 = 1.5$ and (d) $l_1^0/r_0 = l_2^0/r_0 = 2.75$; $l_3^0/r_0 = 2.75$. The number of elements ranges from 1896 for (a) to 2512 for (d).

void spacings as in ref. [5]. The geometric parameters for the different cell dimensions are given in Table 1. For all unit cells, $a_1^0/r_0 = a_2^0/r_0$. Finite element meshes for four unit cell configurations are shown in Fig. 2. The modelling setup does not account for softening due to void evolution since a small strain formulation is used. It is assumed that the unit cell represents the material condition immediately before failure, neglecting the deformation history leading to this state. Hence, model predictions for the loss of load carrying capacity signal the onset of localisation. The critical equivalent stress at the onset of localisation is recorded and reported in the results section.

Table 1: Geometric parameters for the various unit cells considered for $f_0 = 0.01$. Based on [5].

$a_1^0/r_0 = a_2^0/r_0$	a_3^0/r_0	$l_1^0/r_0 = l_2^0/r_0$	l_3^0/r_0
6.06	1.43	5.05	0.43
5.55	1.70	4.55	0.70
5.21	1.94	4.21	0.95
4.97	2.12	3.97	1.12
4.58	2.50	3.58	1.50
4.18	3.00	3.18	2.00
3.75	3.75	2.75	2.75

2.2 Numerical method

The unit cells are subject to prescribed displacements and the boundary conditions applied to the faces of the cell are

$$\begin{aligned} u_1(a_1^0, x_2, x_3) &= U_1(t), \quad T_2(a_1^0, x_2, x_3) = T_3(a_1^0, x_2, x_3) = 0 \\ u_2(x_1, a_2^0, x_3) &= U_2(t), \quad T_1(x_1, a_2^0, x_3) = T_3(x_1, a_2^0, x_3) = 0 \\ u_3(x_1, x_2, a_3^0) &= U_3(t), \quad T_1(x_1, x_2, a_3^0) = T_2(x_1, x_2, a_3^0) = 0 \end{aligned} \tag{1}$$

The applied symmetry boundary conditions are

$$\begin{aligned} u_1(0, x_2, x_3) &= 0, \quad T_2(0, x_2, x_3) = T_3(0, x_2, x_3) = 0 \\ u_2(x_1, 0, x_3) &= 0, \quad T_1(x_1, 0, x_3) = T_3(x_1, 0, x_3) = 0 \\ u_3(x_1, x_2, 0) &= 0, \quad T_1(x_1, x_2, 0) = T_2(x_1, x_2, 0) = 0 \end{aligned} \tag{2}$$

In Eq. (1), $U_1(t)$ is prescribed and the time history of the displacements $U_2(t)$ and $U_3(t)$ are determined such that a prescribed stress state is maintained. The loading direction is fixed in stress space by enforcing constant ratios between the normal stress components throughout the deformation history such that

$$\Sigma_{22} = \rho_2 \Sigma_{11}, \qquad \Sigma_{33} = \rho_3 \Sigma_{11}, \tag{3}$$

where ρ_2 and ρ_3 are constants. The overall stress components Σ_{ij} are found by volume averaging over all elements, such that: $\Sigma_{ij} = \int_V \sigma_{ij} \mathrm{d}V/V$, where V is the unit cell volume.

The overall effective stress, Σ_e, and the overall hydrostatic stress, Σ_h, are given by

$$\Sigma_e = \frac{1}{\sqrt{2}}\sqrt{(\Sigma_{11}-\Sigma_{22})^2+(\Sigma_{22}-\Sigma_{33})^2+(\Sigma_{33}-\Sigma_{11})^2},$$

$$\Sigma_h = \frac{1}{3}(\Sigma_{11}+\Sigma_{22}+\Sigma_{33}),$$

which in terms of the relative stress ratios become

$$\Sigma_e = \Sigma_{11}\frac{1}{\sqrt{2}}\sqrt{(1-\rho_2)^2+(\rho_2-\rho_3)^2+(\rho_3-1)^2}, \quad (4)$$

$$\Sigma_h = \Sigma_{11}\frac{1}{3}(1+\rho_2+\rho_3). \quad (5)$$

The stress triaxiality, T, and the Lode parameter, L, are given by

$$T = \frac{\Sigma_h}{\Sigma_e} = \frac{\sqrt{2}}{3}\frac{1+\rho_2+\rho_3}{\sqrt{(1-\rho_2)^2+(\rho_2-\rho_3)^2+(\rho_3-1)^2}} \quad (6)$$

and

$$L = \frac{2\Sigma_{22}-\Sigma_{11}-\Sigma_{33}}{\Sigma_{11}-\Sigma_{33}} = \frac{2\rho_2-1-\rho_3}{1-\rho_3}. \quad (7)$$

The overall effective strain, $\overline{E}_e$, is given by

$$\overline{E}_e = \frac{\sqrt{2}}{3}\sqrt{(E_{11}-E_{22})^2+(E_{22}-E_{33})^2+(E_{33}-E_{11})^2} \quad (8)$$

where the strain components, E_{ij}, are found in a way analogous to the stress components.

2.2.1 Multiple point constraints

The macroscopic normal stress components vary throughout the deformation, but the stress ratios are maintained in each increment of the simulation according to Eq. (3). This is achieved by creating multi point constraints through the user subroutine MPC in ABAQUS, which enables enforcing relationships between degrees of freedom in one or more nodes.

Additional degrees of freedom are added to impose boundary conditions on all sides of the model while prescribing the stress ratios. Three dummy nodes, N_i, are created outside of the mesh and connected to one connector node, M, in the mesh as shown in Fig. 3. This connection is made through spring elements (SPRING2 elements from the ABAQUS element library). The displacement in the x_1-direction is then prescribed at the N_1-dummy node, while the displacements (in the x_2- and x_3-directions) corresponding to the desired stress triaxiality and Lode parameter are calculated and applied to the N_2- and N_3-dummy nodes. The displacement of the connector node, M, is coupled to the displacement of the nodes located at (a_1^0, x_2, x_3), (x_1, a_2^0, x_3) and (x_1, x_2, a_3^0) in the direction of the respective face normals. In this way, the displacement of the dummy nodes, N_i, is linked to the unit cell.

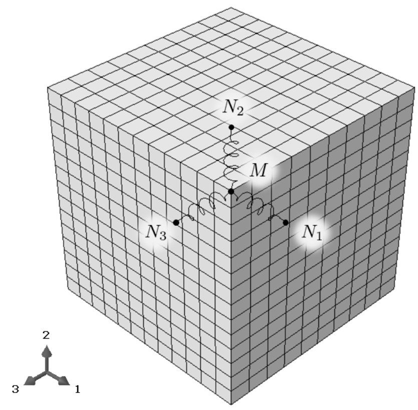

Fig. 3: The spring elements for the multiple point constraints connected to one connector node, M, in the finite element mesh.

The displacement of the dummy nodes, N_i, is related to the forces, F_i, at the faces of the unit cell through

$$F_i = k_i(u_i^{N_i} - u_i^M) \quad \text{with} \quad i = 1,2,3, \quad (9)$$

and k_i being the spring element constants given by $k_i = E(A_i/a_i^0)\times 10^{-1}$, where the factor of 10^{-1} is introduced to stabilise the numerical solution, following Ref. [34]. The forces, F_i, are the resultant of all traction across the corresponding surface and relates to the macroscopic stresses through

$$\Sigma_{11} = \frac{F_1}{A_1}, \qquad A_1 = a_2^0 a_3^0$$
$$\Sigma_{22} = \frac{F_2}{A_2}, \qquad A_2 = a_1^0 a_3^0$$
$$\Sigma_{33} = \frac{F_3}{A_3}, \qquad A_3 = a_1^0 a_2^0 \quad (10)$$

where A_i is the area over which the forces act. Combining Eqs. (3), (9), and (10), gives the dummy node displacements

$$\rho_2 = \frac{\Sigma_{22}}{\Sigma_{11}} = \text{const.} \Rightarrow u_2^{N_2} = u_2^M + \rho_2 \frac{A_2}{A_1}\frac{k_1}{k_2}(u_1^{N_1} - u_1^M)$$
$$\rho_3 = \frac{\Sigma_{33}}{\Sigma_{11}} = \text{const.} \Rightarrow u_3^{N_3} = u_3^M + \rho_3 \frac{A_3}{A_1}\frac{k_1}{k_3}(u_1^{N_1} - u_1^M), \quad (11)$$

where ρ_2 and ρ_3 are input values for the stress ratio, $u_i^{N_j}$ is the displacement of dummy node j in the direction of x_i, u_i^M is the displacement in x_i-direction of the connector node M, A_i are areas from Eq. (10), and k_i are the spring element constants.

The calculations are carried out for three values of Lode parameter, $L = -1, 0$, and 1. The Lode parameter values $L = -1$ ($\Sigma_{11} > \Sigma_{22} = \Sigma_{33}$) and $L = 1$ ($\Sigma_{11} = \Sigma_{22} > \Sigma_{33}$) correspond to overall axisymmetric stress states, while $L = 0$ ($\Sigma_{11} > \Sigma_{22} > \Sigma_{33}$) correspond to an overall state of shear plus hydrostatic stress. For each value of Lode parameter, three triaxialities are considered, $T = 1, 2$, and 3. The values for ρ_2 and ρ_3 to achieve these stress states are given in Table 2.

Table 2: Input parameters determining the prescribed stress state.

L	T	ρ_2	ρ_3
-1	$\frac{1+2\rho_2}{3(1-\rho_2)}$	ρ_3	$\frac{1+2\rho_2}{3(1-\rho_2)}$
	1	0.4	0.4
	2	0.625	0.625
	3	0.727273	0.727273
0	$\frac{1+\rho_2}{\sqrt{3}(1-\rho_2)}$	$\frac{1+\rho_3}{2}$	$\frac{\sqrt{3}T-1}{\sqrt{3}T+1}$
	1	0.634	0.268
	2	0.776	0.552
	3	0.8386	0.6772
1	$\frac{2+\rho_2}{3(1-\rho_2)}$	1	$\frac{3T-2}{3T+1}$
	1	1	0.25
	2	1	0.57
	3	1	0.70

The calculations were carried out using the commercial finite element code ABAQUS with the gradient theory applied to the matrix material through a UEL subroutine. The reader is referred to Ref. [25] for further details on the implementation. The calculations use 20-node user defined elements. The number of elements in the finite element meshes is varied from a minimum of 1896 to a maximum of 2512 elements, Fig. 2.

2.3 Material model: Strain gradient plasticity

The gradient enhanced constitutive model employed is based on the visco-plastic strain gradient plasticity theory proposed by Gudmundson [23] in the context of the mathematical formulation in terms of minimum principles proposed by Fleck and Willis [24]. For the dissipative version considered, the theory accounts for internal elastic energy storage due to elastic strain and dissipation due to the plastic strain rate, $\dot{\varepsilon}^p_{ij}$, and its spatial gradient, $\dot{\varepsilon}^p_{ij,k}$. Contributions from plastic strain gradients to free energy is ignored. The Principle of Virtual Work (PVW) in Cartesian components is expressed by

$$\int_V \left(\sigma_{ij}\delta\dot{\varepsilon}_{ij} + (q_{ij} - s_{ij})\delta\dot{\varepsilon}^p_{ij} + \tau_{ijk}\delta\dot{\varepsilon}^p_{ij,k}\right) \mathrm{d}V = \int_S \left(T_i \delta\dot{u}_i + t_{ij}\delta\dot{\varepsilon}^p_{ij}\right) \mathrm{d}S \quad (12)$$

where σ_{ij} and $s_{ij} = \sigma_{ij} - \frac{1}{3}\delta_{ij}\sigma_{kk}$ are the Cauchy stress tensor and the stress deviator, respectively. The microstress, q_{ij}, is work conjugate to the plastic strain rate, $\dot{\varepsilon}^p_{ij}$, and τ_{ijk} is a higher order stress, work conjugate to the plastic strain rate gradient, $\dot{\varepsilon}^p_{ij,k}$. The right hand side of the PVW includes the conventional traction, $T_i = \sigma_{ij}n_j$ work conjugate to the boundary displacement rate, $\dot{u}_i$, and the higher order traction, $t_{ij} = \tau_{ijk}n_k$, work conjugate to the plastic strain rate, $\dot{\varepsilon}^p_{ij}$. Here, the outward unit normal to the surface S is n_i. Balance laws for the stress quantities are given by

$$\sigma_{ij,j} = 0 \quad \text{and} \quad q_{ij} - s_{ij} - \tau_{ijk,k} = 0 \quad (13)$$

where, the first set of equations is the conventional equilibrium equations in the absence of body forces, and the second set is the higher order equilibrium equations. The higher order boundary conditions are imposed such that the void surface is higher order traction free, while symmetry conditions are imposed at the exterior of the cell through $\varepsilon_{12} = 0$.

2.4 Constitutive equations

The rate-dependent visco-plastic formulation employs a potential to account for plastic dissipation as follows

$$\Phi\left[\dot{E}^p, E^p\right] = \int_0^{\dot{E}^p} \sigma_c \left[\dot{E}^{p'}, E^p\right] \mathrm{d}\dot{E}^{p'} \quad (14)$$

Here, σ_c is the gradient enhanced effective stress, related to the current matrix flow stress through $\sigma_c =$

$\sigma_F[E^p]\left(\frac{\dot{E}^p}{\dot{\varepsilon}_0}\right)^m$, with $\dot{\varepsilon}_0$ denoting the reference strain rate, and m denoting the rate-sensitivity exponent. The material in this work does not undergo strain hardening, making σ_F independent of $\dot{E}^p$ and equal to the material yield stress Σ_0. The viscoplastic law is implemented following the algorithm presented in Ref. [35] to efficiently approach the rate-independent limit. A gradient enhanced effective plastic strain rate is given by

$$\left(\dot{E}^p\right)^2 = \frac{2}{3}\dot{\varepsilon}^p_{ij}\dot{\varepsilon}^p_{ij} + L_D^2\dot{\varepsilon}^p_{ij,k}\dot{\varepsilon}^p_{ij,k} \tag{15}$$

and the associated work conjugate gradient enhanced effective stress by

$$\sigma_c^2 = \frac{3}{2}q_{ij}q_{ij} + \frac{1}{L_D^2}\tau_{ijk}\tau_{ijk}. \tag{16}$$

Here, L_D is a dissipative constitutive length parameter that enters for dimensional consistency. The superscript D refers to dissipative quantities, and the dissipative stress quantities are given by

$$q^D_{ij} = \frac{2}{3}\sigma_c\frac{\dot{\varepsilon}^p_{ij}}{\dot{E}^p}, \quad \tau^D_{ijk} = L_D^2\sigma_c\frac{\dot{\varepsilon}^p_{ij,k}}{\dot{E}^p}. \tag{17}$$

The dissipative length parameter controls the strengthening size effect with an increase in the dissipative length parameter giving an increase in the apparent yield stress in the presence of strain gradients, see [36, 37]. This work is a limit load analysis, which, by definition, is done to determine the overall yield criterion for a given, specific configuration. Limit load analyses normally idealise materials as perfectly plastic. To avoid strain hardening from the energetic gradient contributions, the energetic length parameter, L_E, has been set to zero in this work, and, consequently, the corresponding energetic quantities are omitted.

3 Numerical results and discussion

Throughout, the following material parameters are used; $\Sigma_0/E = 0.001$, $\nu = 0.3$ and $m = 0.01$, where Σ_0 is the yield stress, E is Young's modulus, ν is the Poisson ratio, and m is the strain rate sensitivity exponent. The value of m is considered sufficiently small for the results to approximate a rate-independent material response. The influence of the Lode parameter, L, the stress triaxiality, T, and the normalised length parameter, L_D/r_0, is studied. The effect of the inter-void ligament size is discussed in combination with the other parameters, L, T, and L_D/r_0.

3.1 Critical equivalent stress at localisation

Figure 4 presents the equivalent stress-strain curves for two distinct Lode parameters, $L = -1$ and 1, but for a fixed stress triaxiality, $T = 3$, and a fixed inter-void ligament size of $l_3/r_0 = 1.5$. The equivalent stress-strain curves are depicted for three length parameters, being, $L_D/r_0 = 0.2, 0.5$, and 1 as well as for the conventional limit where $L_D/r_0 = 0$.

The material response shows a clear effect of plastic strain gradients, such that the larger the length parameter, the higher the equivalent stress level. This means that an increase in the stress level is obtained when down-scaling the microstructure and, thus, yielding of the material is delayed due to increasing strain gradient strengthening. The critical equivalent stress, Σ_e^c/Σ_0, signaling localisation (and coalescence) is taken to be at the plateau of the equivalent stress-strain curve.

3.2 Conventional material: Effect of the inter-void ligament size

The conventional limit, $L_D/r_0 = 0$, is considered to set the scene for the study of material size effects. The focus here is the effect of inter-void ligament size on the critical stress at localisation under various loading conditions.

First, three values of the Lode parameter are considered, $L = -1, 0$, and 1, for a fixed stress triaxiality, $T = 2$. Figure 5 shows the critical equivalent stress as a function of the inter-void ligament size. For the six smallest inter-void ligaments, the critical equivalent stress is seen to increase when the inter-void ligament becomes bigger irrespective of the value of the Lode parameter. The increase in the critical stress ties to localisation occurring more easily in small inter-void ligaments lowering the load carrying capacity of the unit cell. As the inter-void ligament size increases, the l_3-ligament can sustain a higher stress level before localisation, leading to an increase in critical equivalent stress. Also, for the six smallest inter-void ligaments, an increase in the critical stress is found with increasing Lode parameter values. Thus, the lowest critical equivalent stress is found for $L = -1$. The dependence on the Lode parameter can be rationalised by considering the imposed stress state. In comparison to the other cases, the relative stress component, ρ_3, is the largest when $L = -1$ (see Tab. 2), and localisation is therefore expected in the l_3-ligament at a lower overall deformation. In contrast, the ρ_3 takes the lowest value for $L = 1$, resulting in delayed localisation and the highest critical equivalent stress obtained. In Ref. [5], void coalescence was found to occur along the ligament with the smallest applied stress for $L > -1$. For all Lode parameters, the relative stress component in the l_3-ligament will be smallest as ρ_3 is always the lowest stress ratio. For $L = -1$, coalescence occurs in the direction of the smallest inter-void ligament size. This corresponds to the l_3-ligament for all geometries except when $l_3/r_0 = 2.75$ as this is a perfect cube, Table 1.

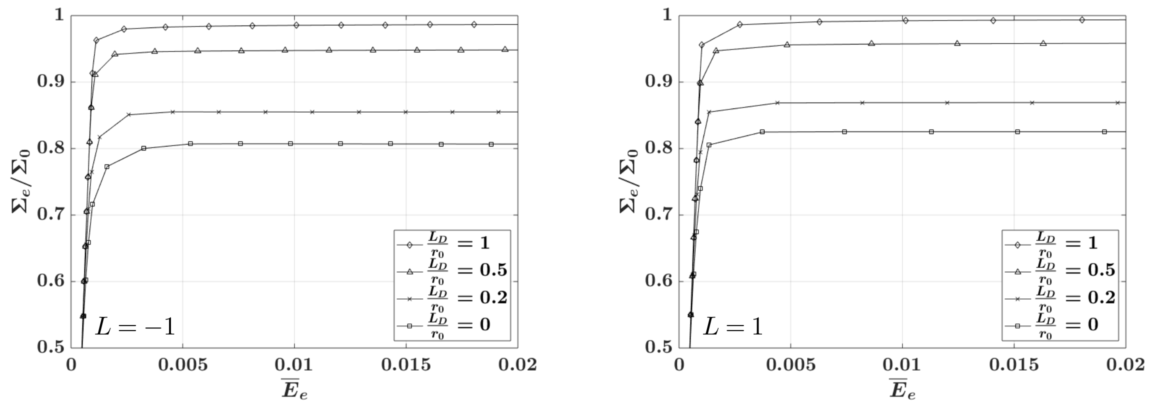

(a) (b)

Fig. 4: Equivalent stress-strain curve for an inter-void ligament size of $l_3/r_0 = 1.5$ under loading conditions giving Lode parameters of (a) $L = -1$ and (b) $L = 1$ and a triaxiality of $T = 3$.

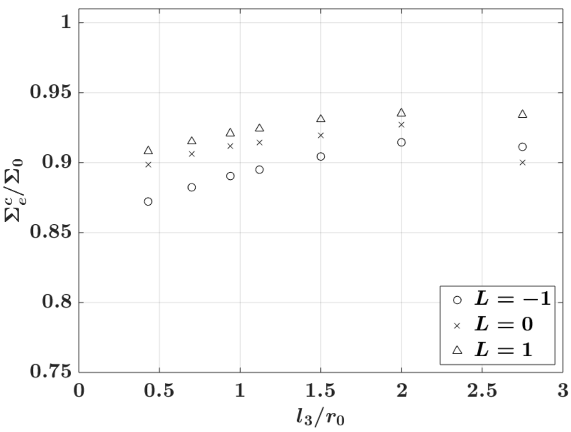

Fig. 5: Critical equivalent stress vs. normalized inter-void ligament size for three values of the Lode parameter with $T = 2$ and $L_D/r_0 = 0$.

There is, however, a shift in the localisation pattern when the l_3-ligament becomes sufficiently wide, for example, a drop in the coalescence stress is found for $l_3/r_0 = 2.75$ for $L = 0$. At this configuration, there is no bias towards the l_3-ligament since the unit cell takes a cubic shape. The shift in the localisation is especially prominent for $L = 0$ (a state of combined hydrostatic tension and shear) where plastic flow localises at $\approx 45°$ across the cubic unit cell leading to an early loss of load carrying capacity. The shift in the localisation is demonstrated by depicting the contours of the effective plastic strain for two distinct unit cells ($l_3/r_0 = 1.5$ and 2.75) subjected to $L = 0$ and $T = 2$ in Figs. 6 and 7. The material response remains conventional such that $L_D/r_0 = 0$, and the loading conditions are described by $L = 0$ and $T = 2$. For the conventional material, the second term of Eq. (15) is zero ($L_D = 0$) and the term *gradient enhanced effective plastic strain* refers to the time integration of only the first term of Eq. (15). For the elongated unit cell ($l_3/r_0 = 1.5$), localisation is seen to occur in the smallest ligament, l_3, whereas localisation is seen to occur along two corners of the cubic unit cell ($l_3/r_0 = 2.75$), indicating that the deformation is localised along $\approx 45°$ i.e. across the diagonal. Figure 6 shows the contour of equivalent plastic strain across the faces of the cell, while Fig. 7(a) and (b) show the contour of the effective plastic strain in the diagonal cross-section of both unit cells at an overall effective strain of $\overline{E}_e = 0.03$. By comparing the two contours it is seen that plastic flow is observed across the entire cross-section indicating localisation at $\approx 45°$ for the cubic model, $l_3/r_0 = 2.75$. In contrast, the plastic flow is constricted for $l_3/r_0 = 1.5$ shown top right in Fig. 7.

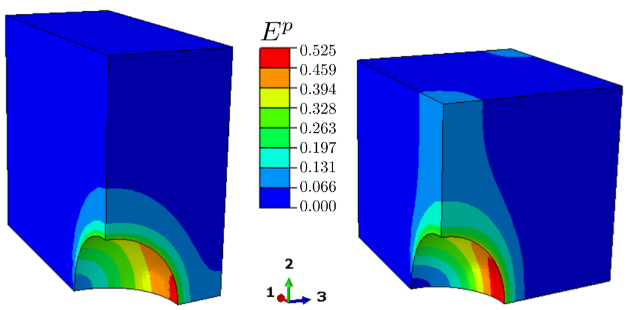

Fig. 6: Distribution of effective plastic strain for $L = 0$, $T = 2$, $L_D/r_0 = 0$, for $l_3/r_0 = 1.5$ to the left and $l_3/r_0 = 2.75$ to the right at a macroscopic effective strain of $\overline{E}_e = 0.03$. For $l_3/r_0 = 1.5$, localisation is favoured in the smallest ligament, l_3. For the cubic unit cell, however, there is no bias towards any of the ligaments and deformation localises along $\approx 45°$, i.e. across the diagonal.

Next, the effect of stress triaxiality is considered. In

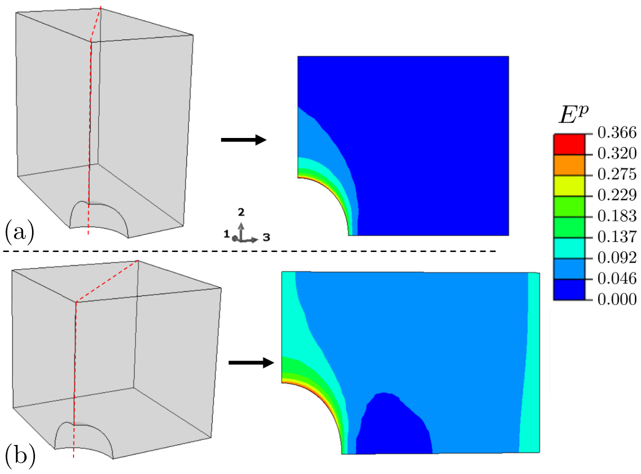

Fig. 7: Distribution of effective plastic strain along a cut from corner to corner for $L = 0$, $T = 2$, $L_D/r_0 = 0$ at $\overline{E}_e = 0.03$ for two geometries: (a) $l_3/r_0 = 1.5$ and (b) $l_3/r_0 = 2.75$. In (a) plasticity has not localized along 45° and for this geometry localisation is favoured in the smaller ligament, while (b) shows that a band, indicated by the dotted line, has formed at a 45^o angle to the main loading axis (the x_1-axis), thus lowering the critical effective stress.

Fig. 8, the critical stress for a conventional material, $L_D/r_0 = 0$, is shown as a function of the inter-void ligament size for $T = 1, 2$, and 3 for a fixed value of the Lode parameter, $L = -1$. In the conventional limit, a high level of stress triaxiality yields low critical stress for all ligament sizes considered. The reason being that a high stress triaxiality corresponds to higher relative stress components, ρ_2 and ρ_3. Figure 8 shows little effect of ligament size on the critical equivalent stress for the low value of triaxiality. For $T = 1$, the relative stress transverse to the main loading direction is insufficient to invoke localisation in the inter-void ligament and the effect of the ligament size will be limited. The cell instead undergoes macroscopic localisation and, consequently, does not exhibit a profound dependence on the inter-void ligament size. This is in line with results presented in Ref. [1], where $T = 1$ has been found to be the limit below which the onset of macroscopic localisation is essentially simultaneous with void coalescence. The results for $T = 2$ and $T = 3$ in Fig. 8 show that the critical equivalent stress is dependent on inter-void ligament size.

A small drop in the critical equivalent stress is seen to occur for the largest ligament for all values of triaxiality in Fig. 8. The effect is most prominent for the highest triaxiality, $T = 3$. Figure 9 shows the contour gradient enhanced effective plastic strain of the cubic cell ($l_3/r_0 = 2.75$) at an effective stress of $\overline{E}_e = 0.08$. At a sufficiently large strain, plasticity is seen to initiate at the corner opposite to the void. Due to the symmetry of both the loading condition ($\Sigma_2 = \Sigma_3$ for $L = -1$) and the unit cell, bands of plastic deformation are observed to stretch across the $x_1 - x_2$ and $x_1 - x_3$ faces, ultimately lowering the coalescence stress giving the drop as seen in Fig. 8.

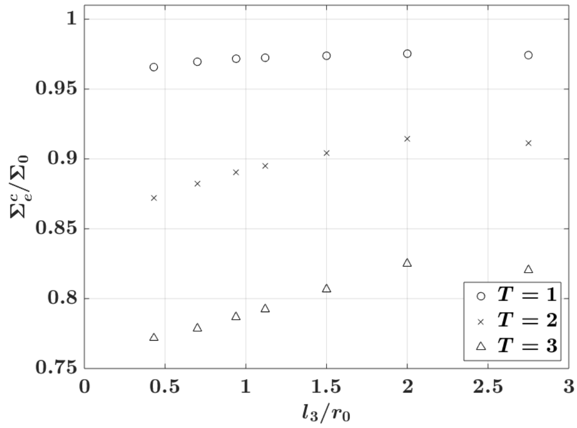

Fig. 8: Critical equivalent stress vs. normalized inter-void ligament size for three values of the stress triaxialities with $L = -1$ and $L_D/r_0 = 0$.

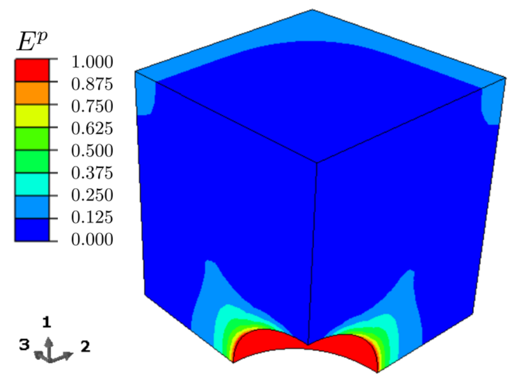

Fig. 9: Bands of plastic flow in the cubic unit cell ($l_3/r_0 = 2.75$) and $L_D/r_0 = 0$ at an overall equivalent strain of $\overline{E}_e = 0.08$. The loading conditions applied to give an axisymmetric stress state with $L = -1$ and $T = 2$. Note the rotated coordinate system to show the symmetry of the plastic flow given by the cubic unit cell and $\rho_2 = \rho_3$ for $L = -1$.

3.3 Gradient enriched material: Effect of the inter-void ligament size

The effect of gradient strengthening in the matrix material is introduced through the length parameter L_D (see Section 2.3). One can imagine down-scaling the microstructure when increasing the value of L_D/r_0. Three values of the length parameter, $L_D/r_0 = 0.2, 0.5$, and 1, are considered in the following for all combinations of the Lode parameter, $L = -1, 0, 1$, and stress triaxiality, $T = 1, 2, 3$. Figure 10 shows the critical effective stress, Σ_e^c/Σ_0, as a function of the inter-void ligament size, l_3/r_0, for all combinations. The results obtained for a conventional material, $L_D/r_0 = 0$ is presented as a reference (see Section 3.2).

The general observation is that the critical stress at localisation increases with the magnitude of the length parameter (down-scaling the microstructure). However, the critical stress has a natural upper bound where the gradient strengthening is so severe that the entire matrix material yields. At such large values of the length parameter, the effect of the Lode parameter, stress triaxiality, and inter-void ligament size vanish and the critical equivalent stress is identical for all combinations of geometry and loading condition. The threshold value is evident from Figs. 10(a)-(i).

Figure 11(a)-(c) show how the length parameter affects the plastic flow in the unit cells by comparing contours of the gradient enhanced plastic equivalent strain, E^p, (see Eq. (15)) for a ligament size of $l_3/r_0 = 1.5$ subject to $L = -1$ and $T = 3$. The contours are extracted at an overall equivalent strain of $\overline{E}_e = 0.02$. Figure 11(a) displays the conventional material response where localisation occurs in the l_3-ligament. At the same level of the overall deformation, a significantly lower effective plastic strain is observed in Fig. 11(b) and (c) when increasing the length parameter. For $L_D/r_0 = 0.2$, Fig. 11(b), some plasticity is seen to develop in the l_3-ligament, but far less than in the conventional case, while the plasticity has barely initiated at this level of the deformation for $L_D/r_0 = 0.5$ Fig. 11(c). The corresponding equivalent stress is shown in Figs. 11(d)-(f). It is seen that the level of stress in the unit cell increases with increasing length parameter. The critical equivalent stress is seen to increase with increased length parameter in Fig. 10 and the material can therefore withstand higher stresses.

Figure 12 shows the change in the deformation mechanism that occurs with increased gradient strengthening. The contour of the normalised rate of equivalent plastic strain, $\dot{E}^p/\dot{\overline{E}}_e$, is shown for the unit cell with the smallest inter-void ligament, $l_3/r_0 = 0.43$ under loading conditions giving $L = 1$ and $T = 3$ for the conventional material with $L_D/r_0 = 0$ and the material with the greatest gradient strengthening contribution, $L_D/r_0 = 1$. Figure 12(a) shows that plastic deformation has developed and localised in the l_3-ligament, as expected for a conventional material at this loading condition. For the matrix surrounding the l_3-ligament, plasticity is reduced in favour of localisation in the l_3-ligament. However, for the gradient strengthened material, plasticity is not only less developed, in line with the gradient strengthening, but also smeared out across the unit cell, see Fig. 12(b). Localisation is to a little extent observed in the l_3-ligament, but overall the entire cell experiences plasticity. This is indicative of a change in deformation mechanism along the lines of the one observed in Ref. [1] for a stress triaxiality of 1. However, here it is seen with an increasing length parameter. As L_D/r_0 increases, the cell is more likely to undergo simultaneous macroscopic localisation and void coalescence in contrast to a conventional material where the cell predominantly undergoes void coalescence for the same loading conditions.

The combined effect of the stress triaxiality (for a fixed Lode parameter) and the length parameter is visualised by the rows in Fig. 10, while the combined effect of the Lode parameter (for a fixed stress triaxiality) and length parameter is visualised by the columns in Fig. 10. Qualitatively, for a fixed stress triaxiality value, the length parameter has a nearly identical impact for all values of the Lode parameter; the critical stress increases with increasing length parameter. It is, however, interesting that the drop in coalescence stress the cubic unit cell ($l_3/r_0 = 2.75$) subject to $L = 0$ diminishes with increasing length parameter for all values of stress triaxiality, Figs. 10(d)-(f). This is because increased gradient strengthening delays the intensification of the plastic flow and homogenizes the plastic strain field.

For the lowest stress triaxiality value, $T = 1$, the effect of the length parameter is small. Nonetheless, the plastic strain gradients that build up around the void give rise to the small increase in gradient strengthening. For the loading conditions giving $T = 1$, the onset of localisation is significantly delayed, thus allowing the material to withstand higher critical stress with a smaller dependence on the inter-void ligament size. The deformation mechanism prevailing at this low value of triaxiality, where macroscopic localisation and void coalescence occur simultaneously [1], implies that the gradients surrounding the void will not influence the critical equivalent stress to a great extent, as the deformation takes place in the entire unit cell.

For a higher value of stress triaxiality, $T = 2$, the effect of the length parameter is more prominent as seen in Fig. 10, and the smaller the inter-void ligament size, the greater the effect of the length parameter is. This is because, at higher stress triaxiality values, the plastic flow tends to localise in the inter-void ligaments as the ligaments diminish in size. The localisation induces large plastic strain gradients that in turn contribute to strengthening. The gradient induced strengthening in the inter-void ligament then inhibits further plastic flow localisation and delays void coalescence. Although not shown here, for $L = -1$ and $T = 2$, the gradient strengthening is sufficiently large that increasing the value of L_D/r_0 from 1 to 2, has a negligible effect. For the intermediate length parameter, $L_D/r_0 = 0.5$, the effects of triaxiality and inter-void ligament size are still visible but greatly reduced due to the smaller degree of gradient strengthening. For the smallest value of the

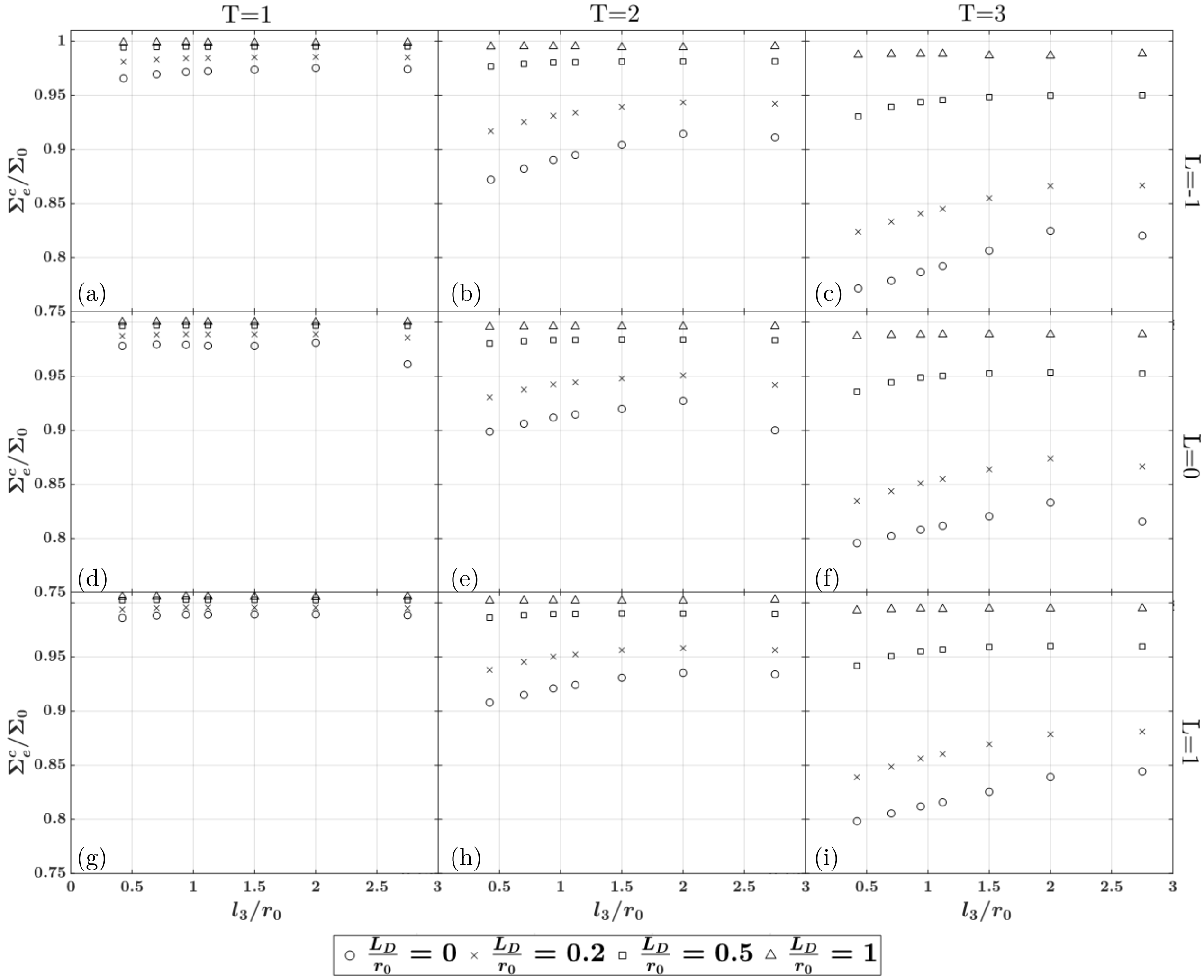

Fig. 10: The critical equivalent stress as a function of the smallest inter-void ligament size. Three values of the Lode parameter are considered, $L = -1, 0$, and 1. For each Lode parameter, three values of the stress triaxiality are considered, $T = 1, 2$, and 3. Throughout, the parameters $\Sigma_0/E = 0.001$, $\nu = 0.3$ and $m = 0.01$ are used. The initial void volume fraction is, $f_0 = 0.01$. The length parameter that enters through the gradient plasticity theory is $L_D/r_0 = 0.2, 0.5$ and 1. A conventional material is modelled with $L_D/r_0 = 0$ and used as a reference.

length parameter, $L_D/r_0 = 0.2$, the critical equivalent stress values follow those of the conventional material, just at a higher relative level for all inter-void ligament size considered. For $L = 0$ and $L = 1$, for $T = 2$, the same effect is seen. The most pronounced effect of the length parameter is seen for $L = -1$, $T = 3$ and $l_3/r_0 = 0.43$ as this configuration has the lowest critical effective stress for the conventional material, but shows the same critical stress for $L_D/r_0 = 1$ as in the remaining results.

4 Summary and conclusions

The interaction of the inter-void ligament size and the gradient induced material size effect on void coalescence is investigated for a range of imposed stress states, here characterised by fixed values of the stress triaxiality and the Lode parameter. To this end, three dimensional finite element unit cell calculations for a single initially spherical void embedded in strain gradient enhanced material matrix are carried out. A conventional material matrix (absence of gradient induced strengthening effects) is considered as reference. The results for the conventional material show that the critical coalescence stress increases when increasing the inter-void ligament size. The effect of the inter-void ligament size is, however, dependent on the imposed stress triaxiality, such that the effect of the inter-void ligament size increases with increasing stress triaxiality. However, above a certain threshold for the inter-void ligament size, the results show a slight decrease in the critical stress. This drop has to do with a transition from plastic flow localisation within the smallest inter-void ligament to plastic flow localization at $\approx 45°$ to the main loading axis. The transition in the plastic flow localisation pattern

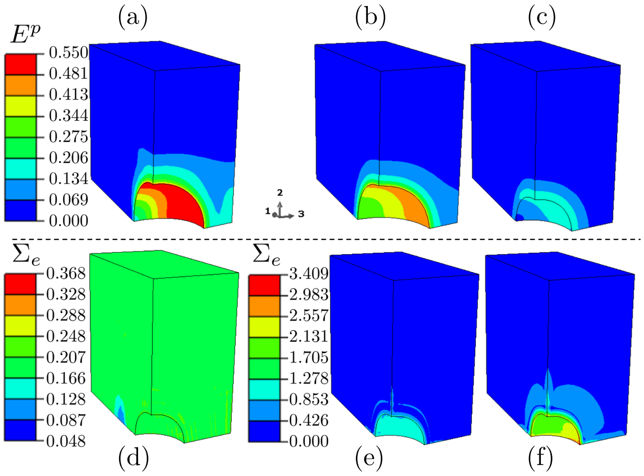

Fig. 11: Distribution of gradient enhanced effective plastic strain for $L = -1$, $T = 3$, $l_3/r_0 = 1.5$ for (a) the conventional material, $L_D/r_0 = 0$, (b) $L_D/r_0 = 0.2$ and (c) $L_D/r_0 = 0.5$ at a macroscopic effective strain of $\overline{E}_e = 0.02$. The effective stress, Σ_e, for the same configuration is shown in the cells at the bottom, also here with (d) the conventional material, (e) $L_D/r_0 = 0.2$ and (f) $L_D/r_0 = 0.5$.

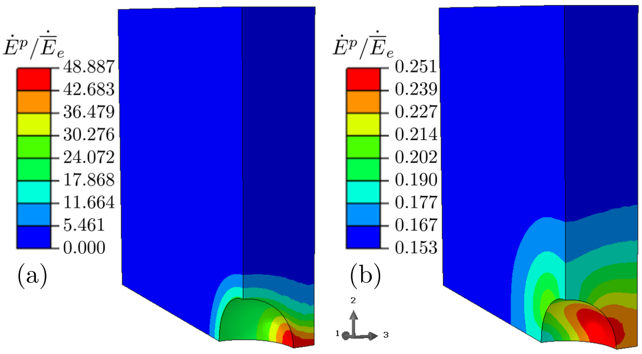

Fig. 12: Change in deformation mode with increased length parameter for $l_3/r_0 = 0.43$ with loading conditions described by $L = 1$ and $T = 3$. The conventional material with $L_D/r_0 = 0$ is shown in a), while b) shows a gradient enriched material with $L_D/r_0 = 1$.

is found to be particularly pronounced for a Lode parameter of $L = 0$. However, irrespective of the Lode parameter value, the transition occurs as the unit cells approach a cubic geometry.

For a void embedded in a strain gradient enhanced material matrix, the value of the critical coalescence stress increases with increasing length parameter i.e. increasing the gradient strengthening effect. The effect of the length parameter is found to intensify with increasing imposed stress triaxiality and decreasing inter-void ligament size. This is due to a propensity for plastic flow localisation in the inter-void ligament when the ligament is small and the stress triaxiality high. Plastic flow localisation introduces large plastic strain gradients which in turn strengthens the ligament and delays further localisation of plastic flow. The strengthening from plastic strain gradients also leads to a weakened dependency in the critical coalescence stress on the inter-void ligament size. Finally, the results show that there exists a natural upper bound where the gradient strengthening is so severe that the entire matrix material yields. For very large values of the length parameter, the effect of the imposed stress state and the inter-void ligament size vanish, and the critical equivalent stress is identical for all combinations of the unit cell geometry and the loading conditions considered.

Acknowledgements

This research was financially supported by the Danish Council for Independent Research through the research project "Advanced Damage Models with InTrinsic Size Effects" (Grant no: DFF-7017-00121). The computing resources provided by the high performance research computing center at Texas A&M University are gratefully acknowledged.

References

[1] Tekoğlu, C., Hutchinson, J., and Pardoen, T., 2015. "On localization and void coalescence as a precursor to ductile fracture". *Philosophical Transactions of the Royal Society A: Mathematical, Physical and Engineering Sciences,* **373**(2038), p. 20140121.

[2] Guo, T., and Wong, W., 2018. "Void-sheet analysis on macroscopic strain localization and void coalescence". *Journal of the Mechanics and Physics of Solids,* **118**, pp. 172–203.

[3] Liu, Y., Zheng, X., Osovski, S., and Srivastava, A., 2019. "On the micromechanism of inclusion driven ductile fracture and its implications on fracture toughness". *Journal of the Mechanics and Physics of Solids,* **130**, pp. 21–34.

[4] Pardoen, T., and Hutchinson, J., 2000. "An extended model for void growth and coalescence". *Journal of the Mechanics and Physics of Solids,* **48**(12), pp. 2467–2512.

[5] Srivastava, A., and Needleman, A., 2013. "Void growth versus void collapse in a creeping single crystal". *Journal of the Mechanics and Physics of Solids,* **61**(5), pp. 1169–1184.

[6] Torki, M., Benzerga, A., and Leblond, J.-B., 2015. "On void coalescence under combined tension and shear". *Journal of Applied Mechanics,* **82**(7).

[7] Torki, M., Tekoglu, C., Leblond, J.-B., and Benzerga, A., 2017. "Theoretical and numerical analysis of void coalescence in porous ductile solids under arbitrary loadings". *International Journal of Plasticity,* **91**, pp. 160–181.

[8] Budiansky, B., Hutchinson, J., and Slutsky, S., 1982. "Void growth and collapse in viscous solids". In *Mechanics of solids.* Elsevier, pp. 13–45.

[9] Koplik, J., and Needleman, A., 1988. "Void growth and coalescence in porous plastic solids". *International Journal of Solids and Structures,* **24**(8), pp. 835–853.

[10] Needleman, A., Tvergaard, V., and Hutchinson, J., 1992. "Void growth in plastic solids". In *Topics in fracture and fatigue*. Springer, pp. 145–178.

[11] Benzerga, A. A., and Leblond, J.-B., 2010. "Ductile fracture by void growth to coalescence". In *Advances in applied mechanics*, Vol. 44. Elsevier, pp. 169–305.

[12] Stelmashenko, N., Walls, M., Brown, L., and Milman, Y., 1993. "Microindentations on W and Mo oriented single crystals: an STM study". *Acta Metallurgica et Materialia,* **41**(10), pp. 2855–2865.

[13] Ma, Q., and Clarke, D., 1995. "Size dependent hardness of silver single crystals". *Journal of Materials Research,* **10**(4), pp. 853–863.

[14] Fleck, N., Muller, G., Ashby, M., and Hutchinson, J., 1994. "Strain gradient plasticity: theory and experiment". *Acta Metallurgica et Materialia,* **42**(2), pp. 475–487.

[15] Stölken, J., and Evans, A., 1998. "A microbend test method for measuring the plasticity length scale". *Acta Materialia,* **46**(14), pp. 5109–5115.

[16] Tvergaard, V., and Niordson, C., 2007. "Size-effects in porous metals". *Modelling and Simulation in Materials Science and Engineering,* **15**, pp. 51–60.

[17] Niordson, C., 2008. "Void growth to coalescence in a non-local material". *European Journal of Mechanics A - Solids,* **27**, pp. 222–233.

[18] Tvergaard, V., and Niordson, C., 2004. "Nonlocal plasticity effects on interaction of different size voids". *International Journal of Plasticity,* **20**(1), pp. 107–120.

[19] Li, Z., and Steinmann, P., 2006. "Rve-based studies on the coupled effects of void size and void shape on yield behavior and void growth at micron scales". *International Journal of Plasticity,* **22**(7), pp. 1195–1216.

[20] Monchiet, V., and Bonnet, G., 2013. "A gurson-type model accounting for void size effects". *International Journal of Solids and Structures,* **50**(2), pp. 320–327.

[21] Nielsen, K., 2017. "Size effects in void coalscence". *In: Contributions to the Foundations of Multidisciplinary Research in Mechanics*(The 24th International Congress of Theoretical and Applied Mechanics; August 22-26, 2016; Montreal, Canada).

[22] Holte, I., Niordson, C. F., Nielsen, K. L., and Tvergaard, V., 2019. "Investigation of a gradient enriched gurson-tvergaard model for porous strain hardening materials". *International Journal of Mechanics A-solids,* **75**, pp. 472–484.

[23] Gudmundson, P., 2004. "A unified treatment of strain gradient plasticity". *Journal of the Mechanics and Physics of Solids,* **52**(6), pp. 1379–1406.

[24] Fleck, N., and Willis, J., 2009. "A mathematical basis for strain-gradient plasticity theory: Part II: tensorial plastic multiplier". *Journal of the Mechanics and Physics of Solids,* **57**(7), pp. 1045–1057.

[25] Martínez-Pañeda, E.and Deshpande, V., Niordson, C., and Fleck, N., 2019. "The role of plastic strain gradients in the crack growth resistance of metals". *Journal of the Mechanics and Physics of Solids,* **126**, pp. 136–150.

[26] Zhang, K., Bai, J., and Francois, D., 2001. "Numerical analysis of the influence of the lode parameter on void growth". *International Journal of Solids and Structures,* **38**(32-33), pp. 5847–5856.

[27] Kim, J., Gao, X., and Srivatsan, T., 2004. "Modeling of void growth in ductile solids: effects of stress triaxiality and initial porosity". *Engineering fracture mechanics,* **71**(3), pp. 379–400.

[28] Gao, X., and Kim, J., 2006. "Modeling of ductile fracture: significance of void coalescence". *International Journal of Solids and Structures,* **43**(20), pp. 6277–6293.

[29] Barsoum, I., and Faleskog, J., 2007. "Rupture mechanisms in combined tension and shear—micromechanics". *International Journal of Solids and Structures,* **44**(17), pp. 5481–5498.

[30] Bao, Y., and Wierzbicki, T., 2004. "On fracture locus in the equivalent strain and stress triaxiality space". *International Journal of Mechanical Sciences,* **46**(1), pp. 81–98.

[31] Barsoum, I., and Faleskog, J., 2007. "Rupture mechanisms in combined tension and shear—experiments". *International journal of solids and structures,* **44**(6), pp. 1768–1786.

[32] Srivastava, A., Gopagoni, S., Needleman, A., Seetharaman, V., Staroselsky, A., and Banerjee, R., 2012. "Effect of specimen thickness on the creep response of a ni-based single-crystal superalloy". *Acta Materialia,* **60**(16), pp. 5697–5711.

[33] Srivastava, A., and Needleman, A., 2015. "Effect of crystal orientation on porosity evolution in a creeping single crystal". *Mechanics of Materials,* **90**, pp. 10–29.

[34] Tekoglu, C., 2014. "Representative volume element calculations under constant stress triaxiality, lode parameter, and shear ratio". *International Journal of Solids and Structures,* **51**(25-26), pp. 4544–4553.

[35] Fuentes-Alonso, S., and Martínez-Pañeda, E., 2020. "Fracture in distortion gradient plasticity". *International Journal of Engineering Science,* **156**, p. 103369.

[36] Martínez-Pañeda, E., Niordson, C. F., and Bardella, L., 2016. "A finite element framework for distortion gradient plasticity with applications to bending of thin foils". *International Journal of Solids and Structures,* **96**, pp. 288–299.

[37] Voyiadjis, G. Z., and Faghihi, D., 2012. "Thermomechanical strain gradient plasticity with energetic and dissipative length scales". *International Journal of Plasticity,* **30**, pp. 218–247.

DTU Mechanical Engineering
Section of Solid Mechanics
Technical University of Denmark

Nils Koppels Allé, Bld. 404
DK-2800 Kgs. Lyngby
Denmark
Tlf.: +45 4525 4250
Fax: +45 4525 1961

www.mek.dtu.dk

January 2021

ISBN: 978-87-7475-641-5

DCAMM
Danish Center for Applied Mathematics and Mechanics

Nils Koppels Allé, Bld. 404
DK-2800 Kgs. Lyngby
Denmark
Phone (+45) 4525 4250
Fax (+45) 4525 1961

www.dcamm.dk

DCAMM Special Report No. S289

ISSN: 0903-1685